UNIVERSITY OF CALIFORNIA, SAN DIEGO

Investigation of the Effect of Shock, Vibration, Surface Texture and Surface Pattern on the Dynamics of the Head Disk Interface

A dissertation submitted in partial satisfaction of the

requirements for the degree Doctor of Philosophy

in

Engineering Sciences (Mechanical Engineering)

by

Aravind N. Murthy

Committee in charge:

Professor Frank E. Talke, Chair
Professor Randolph Bank
Professor David Benson
Professor Thomas Bewley
Professor Jack K. Wolf

2007

The dissertation of Aravind N. Murthy is approved, and it is acceptable in quality and form for publication on microfilm:

_____

_____

_____

_____

_____

Chair

University of California, San Diego

2007

TABLE OF CONTENTS

LIST OF FIGURES

ACKNOWLEDGEMENT

I would first like to thank my advisor Professor Frank E. Talke for his advice and support during my studies at UCSD. Professor Talke offered me a position as a Teaching Assistant for his Computer Aided Design and Analysis class in Winter 2003 and many more quarters after that. In 2003, I started as a Research Assistant in Professor Talke's laboratory at the Center for Magnetic Recording Research. I would like to thank Professor Talke for his guidance in my research, his help with all my presentations, publications and this thesis.

I would like to thank my co-author of many publications, Dr. Bert Feliss for providing me an opportunity to work with him as an intern during the summer of 2004. In addition, I would like to thank Dr. Reinhard Wolter, Dr. Donald Gillis, and the AdTech Department of Hitachi GST (San Jose) for their help during my internship.

I would like to also thank Dr. Eric M. Jayson for his help and advice at the beginning of my thesis. In addition, I would like to thank Professor Itzhak Etsion from the Technion, at Haifa, Israel for many helpful discussions related to textured sliders. I would also like to thank Yutaka Okazaki of J-Fenix, Japan, for providing designs for HDD suspensions and enclosures.

I would especially like to thank all the members of Professor Talke's group who were very helpful during my research here at CMRR. In particular, I would like to thank Mathias Pfabe and Jianfeng Xu for our joint work and publication. I would like to thank Dr. Jiadong Zhang and Dr. Maik Duwensee for many discussions and advice concerning

the CMRR air bearing simulator code. I would like to thank Dr. Lin Zhou for his help regarding many software difficulties. I would also like to thank Marcia Levitt, Betty Manoulian and Iris Villanueva for helping me with conference travel and accounting details.

Acknowledgement for published work:

Chapter 3 is a partial reprint of the material as in “Effect of Non-operational Shock on the Suspension Lift-tab and Dimple Separation in a Load/Unload Hard Disk Drive”, A. N. Murthy, E. M. Jayson, and F. E. Talke, submitted to *Tribology International*. The dissertation author was the primary investigator of this paper and was directly supervised by Prof. Frank E. Talke. The co-author Dr. Eric M. Jayson has given his permission to include the material of the paper in this dissertation.

Chapter 4 is a partial reprint of the material as in "Experimental and Numerical Investigation of Shock Response in 3.5 and 2.5 inch form factor Hard Disk Drives", A. N. Murthy, B. Feliss, D. Gillis, and F. E. Talke, Microsystem Technologies, Vol.12 (no. 12): 1109-1116, 2006. The dissertation author was the primary investigator of this paper directly supervised by Prof. Frank E. Talke. The co-authors Dr. Bert Feliss and Dr. Donald Gillis have given their permission to include the material of the paper in this dissertation.

Chapter 5 is a partial reprint of the material as in “Dynamic Response of 1-inch Form Factor Disk Drives to External Shock and Vibration Loads”, A. N. Murthy, M. Pfabe, J. Xu, and F. E. Talke, Microsystem Technologies, published online, 2006. The

dissertation author was the primary investigator of this paper and was directly supervised by Prof. Frank E. Talke. The co-authors Mathias Pfabe and Jiafeng Xu have given their permission to include the material of the paper in this dissertation.

Chapter 5 is a partial reprint of the material as in "Microdrive Operational and Non-operational Shock and Vibration Testing,", B. Feliss, A. N. Murthy, and F. E. Talke, Microsystem Technologies, published online, 2006. The dissertation author was the primary investigator for the numerical analysis of this paper which was directly supervised by Prof. Frank E. Talke. The co-author Dr. Bert Feliss has kindly given his permission to include the experimental results of the paper (for comparison) in this dissertation.

Chapter 8 is a partial reprint of the material as in "Analysis of Surface Textured Air Bearing Sliders with Rarefaction Effects", A. N. Murthy, I. Etsion and F. E. Talke, published online in *Tribology Letters*, 2007. The dissertation author was the primary investigator of this paper and was directly supervised by Prof. Frank E. Talke. The co-author Prof. Itzhak Etsion has given his permission to include the material of the paper in this dissertation. Partial support of the work in chapter 8 was obtained through the National Science Foundation (NSF) under Grant CMS0408658

Chapter 8 is a partial reprint of the material as in "Dynamic Response of 1-inch Form Factor Disk Drives to External Shock and Vibration Loads", A. N. Murthy, M. Pfabe, J. Xu, and F. E. Talke, Microsystem Technologies, published online, 2006. The dissertation author was the primary investigator of this paper and was directly supervised by Prof. Frank E. Talke. The co-authors Mathias Pfabe and Jiafeng Xu have given their

permission to include the material of the paper in this dissertation.

Chapter 9 is a partial reprint of the material as in “Numerical Simulations of the Head/Disk Interface for Patterned Media”, A. N. Murthy and F. E. Talke, submitted to ASME Information Storage and Processing Systems, 2007. The dissertation author was the primary investigator of this paper directly supervised by Prof. Frank E. Talke.

VITA

1999–2000	Engineering Intern, National Aerospace Laboratories, Bangalore, India
2000	B.E., Mechanical Engineering, BMS College of Engineering, Bangalore University
2000–2001	Consultant, Thesys Technologies, Chennai, India
2001–2006	Teaching Assistant, Department of Mechanical and Aerospace Engineering, University of California, San Diego
2004	M.S., University of California, San Diego
2001–2007	Research Assistant, Center for Magnetic Recording Research, University of California, San Diego
2004	Summer Intern, Hitachi Global Storage Technologies, San Jose, California, USA
2007	Ph.D., University of California, San Diego

PUBLICATIONS

A. N. Murthy, B. Feliss, D. Gillis, and F. E. Talke " Experimental and Numerical Investigation of Shock Response in 3.5 and 2.5 inch form factor Hard Disk Drives", *Microsystem Technologies* (2006) 12: 1109-1116

A. N. Murthy, E. M. Jayson and F. E. Talke "Effect of Non-Operational Shock on Suspension Lift-Tab and Dimple Separation in a Load/Unload Disk Drive", submitted for publication to *Tribology International.* (2006)

A. N. Murthy, M. Pfabe, J. Xu, and F. E. Talke, "Dynamic Response of 1-inch Form Factor Disk Drives to External Shock and Vibration Loads", *Microsystem Technologies*, 13, 8-10, 1031-1038, (2007)

B. Feliss, A. N. Murthy, and F. E. Talke, "Microdrive Operational and Non-Operational Shock and Vibration Testing", *Microsystem Technologies*, 13, 8-10, 1015-1021, (2007)

A. N. Murthy, I. Etsion, and F. E. Talke, "Analysis of Surface Textured Air Bearing Sliders with Rarefaction Effects", published online in *Tribology Letters* (2007)

A. N. Murthy, M. Duwensee, and F. E. Talke, "Numerical Simulations of the Head/Disk Interface for Patterned Media", to be submitted to *Tribology Letters* (2007)

ABSTRACT OF THE DISSERTATION

Investigation of the Effect of Shock, Vibration, Surface Texture and Surface Pattern on the Dynamics of the Head Disk Interface

by

Aravind N. Murthy

Doctor of Philosophy in Engineering Sciences (Mechanical Engineering)

University of California, San Diego, 2007

Professor Frank E. Talke, Chair

Numerical methods were used to study the effect of shock and vibrations on hard disk drives. Finite element models of the hard disk drive were developed for the operational and non-operational state of the drive for three different form factors. The numerical results were compared and validated with experimental data. A commercially available non-linear finite element solver was used to obtain the structural response of the hard disk drive components subject to external shock and vibration inputs. A finite element solution of the Reynolds equation was used to investigate the air bearing response of the head disk interface. The inclusion of surface texture and surface pattern on the slider air bearing surface and its effect on slider flying characteristics were studied.

1

Introduction

1.1 Overview of Hard Disk Drive Technology

It has been over fifty years since the introduction of the first magnetic recording hard disk drive ("Random Access Method for Accounting and Control" or "IBM 305 RAMAC" [1]), designed and manufactured by IBM in 1956. The IBM 305 RAMAC contained a disk drive called "350 Disk File". The 350 Disk File consisted of a stack of fifty 24 inch disks. The capacity of the entire disk file was 5 million 7-bit characters ("bytes" were not not yet in use back in 1956). This capacity works out to about 4.4 MB (Megabytes) in present term. This is about the same capacity as that of the first personal computer hard drives that appeared in the early 1980's, but was a huge storage capacity for 1956. The IBM 305 RAMAC computer system with 350 Disk File storage was leased at a rate of $3,200 per month, equivalent to a purchase price of about $160,000

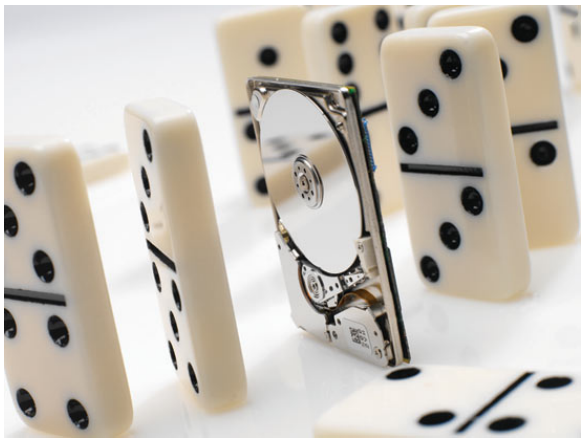

Figure 1.1: 0.85 inch form factor hard disk drive compared to a set of dominos (source Toshiba [7])

in 1957 dollars.

The development of hard disk drive technology since then has been no less than amazing. Currently, hard disk drives with storage capacity on the order of 500 GB are available and are used in modern computer systems. Recently (April 2007), Hitachi Global Storage Technologies [6] shipped a so-called “terabyte drive” [5] with storage capacity of 1 TB (or 1000 GB). These drives are shipped to retailers at suggested retail price of $399 per drive. In addition to the enormous increase in the storage capacity and reduction of the cost per drive, the physical size of the drive itself has scaled down from a drive that needed a 9 m by 15 m room to a drive (0.85 inch form factor) that is comparable to the size of a domino dice (see Figure 1.1).

Not only has the overall size of hard disk drives been reduced tremendously, but also the cost per drive has reduced over the years. The combination of increase in

storage capacity with reduced drive form factors and the availability at a reasonable cost has maintained an ever-increasing demand for hard disk drives. Every consumer wants his/her computer to work indefinitely without any hard drive failure. However, a hard disk drive is a product of various aspects of engineering disciplines such as mechanical, chemical, thermal, electrical, electronics, servo technology, control theory, computer science, etc. The smooth operation of a disk drive relies on all these factors considered in product design as well as environmental factors such as air pressure, temperature, external shock and vibration, etc.

The mechanics and tribology problems of the head disk interface in current hard disk drives will be studied in this dissertation.

1.2 Hard Disk Drive Components

A hard disk drive consists of both electrical and mechanical components assembled and housed in a rectangular enclosure. Figure 1.2 shows the various components of a typical hard disk drive. The main mechanical components are the disk, the actuator arm, and the head-suspension assembly. The components are inter-connected to each other as two separate assemblies. One is the disk-spindle assembly consisting of the spindle motor and the disk. The other is the "head-stack assembly" consisting of the actuator arm, suspension, gimbal/flexure, and the slider with the read/write head all connected to a voice coil motor (VCM). The disk is attached to the spindle motor that

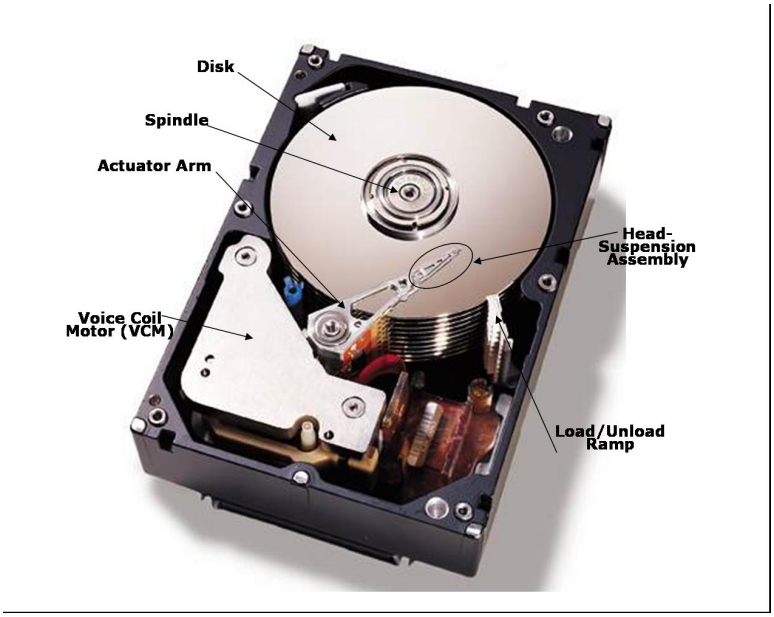

Figure 1.2: Components of a typical hard disk drive (HDD)

will spin the disk at 4200 rpm to 15000 rpm. The spindle motor in hard disk drives is either a ball bearing spindle motor or a fluid dynamic bearing (FDB) spindle motor. The FDB spindle motor is the popular choice in present day hard disk drives. This is due to the fact that FDB spindles have better non-operational shock performance, lower power consumption, lower Non Repeatable Run-Out (NRRO), and lower acoustic noise compared to ball bearing spindle motors. Figure 1.3 shows the schematic of the FDB spindle motor used in hard disk drives.

In order to increase the storage capacity in a single hard disk drive, several disks and head stack assemblies are built into a single stack. Read and write heads are attached to a slider which is in turn attached to a suspension - actuator arm assembly (one for each side of the disks). The stack of such actuator arms referred to as the " E-block" moves

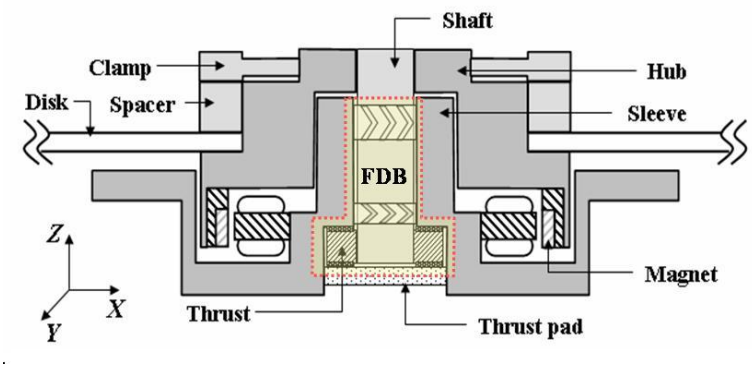

Figure 1.3: Fluid Dynamic Bearing (FDB) spindle used in HDD's

across the disk radially powered by the voice coil motor. The voice coil motor is the positioning motor that positions the slider with the read/write head over a specific data track on the disk. The head is the electromagnetic device that writes (records), reads, and erases data on a magnetic media. It contains a read core and a write core which is used to produce or receive magnetic flux. The read/write head is the recording element which writes data to the magnetic media and reads recorded data from the media. The actuator arm can position the slider with the read/write head accurately over the disk surface through a feedback from the servo system. The actuator arm is powered by the rotary voice coil motor. The load/unload ramp is a mechanical component where the suspension is 'parked' while the disk drive is not operating. When the drive is powered, the actuator arm and the head-suspension assembly move off the ramp and can glide smoothly over the disk surface after the disk attains a suitable rotational speed.

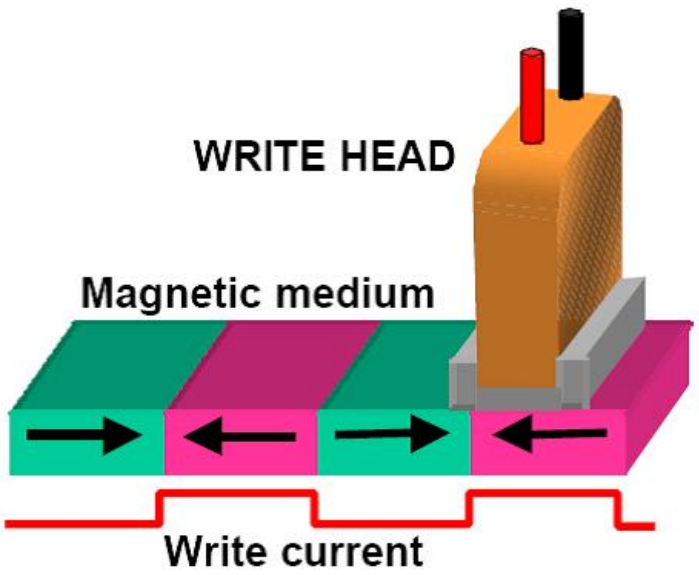

Figure 1.4: Schematic for the write process in magnetic recording

1.3 Principles of Magnetic Recording

In order to store and retrieve data on the magnetic disk, a read/write head is used. Modern magnetic recording heads combine elements of the read and write functions into a single merged head. The information is stored in small domains, called "bits", in the magnetic disk media. Writing employs a magnetic coil that is activated each time a bit needs to be written, or magnetized on the rotating disk. The small, concentrated magnetic field magnetizes a region on the disk. When a current is applied to generate the magnetic field, the hard disk medium is magnetized with a polarity that corresponds to the direction of the writing field. Reversing the current reverses the polarity on the bit to rewrite or erase the information stored in digital format. Figure1.4 shows the process of writing on magnetic disk medium for longitudinal recording. It is important to note that

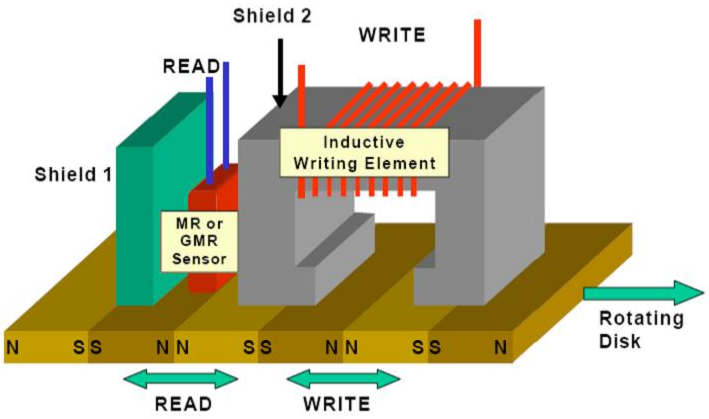

Figure 1.5: Read (with MR/GMR head) and Write process

the change in magnetization direction stores the data and not the magnetization direction itself.

The reading process is performed using a Magnetoresistive (MR) or Giant Magnetoresistive (GMR) head. Magnetoresistive material is typically a nickel-iron alloy that shows an increase in electrical resistance when the current flow is parallel to the magnetic orientation than when it is perpendicular. The resistance drops back to the original value when the magnetic field is removed. The MR head "sees" a vertical magnetic field (up or down) at each transition. The magnetic field changes the resistance and indicates the transition. The greater the measure of change in resistivity, the more accurate or sensitive the reading will be. The GMR sensors utilize the quantum nature of electrons that have two spin states, up and down. Conducting electrons with spin direction parallel to the sensor film's magnetic orientation move easily and thus produce a low electrical resistance. However, the movement of electrons of opposite spin direction is impeded by

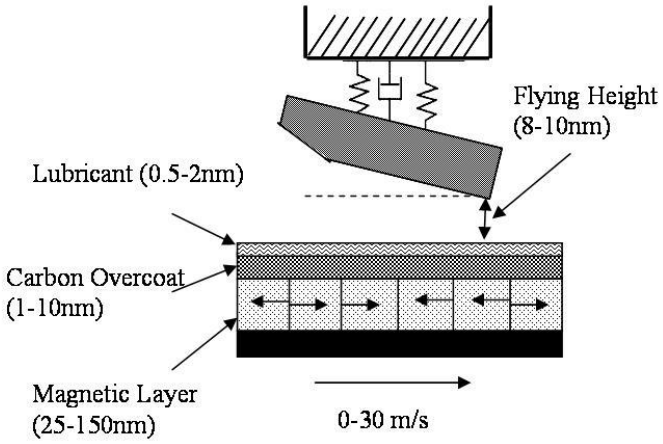

Figure 1.6: Typical head disk interface in hard disk drives

frequent collisions with atoms in the film, thereby producing a higher resistance. Figure 1.5 shows the combined read-write process for magnetic storage in hard disk drives.

1.4 The Head Disk Interface

The cross section of a typical head disk interface is shown schematically in Figure 1.6. As can be seen, the slider flies over the spinning disk maintaining a stable 'flying height' due to the hydrodynamic air bearing at the interface. This flying height is a subset of the 'magnetic spacing' which is defined as the spacing between the read/write head and the magnetic layer on the disk. The magnetic spacing has a substantial effect on the areal density in hard disk drives. The smaller the magnetic spacing, the larger is the voltage signal during the read process. Wallace [1951] derived a spacing loss

equation for sine wave recording, given by

$$\frac{A}{A_o} = e^{-kd} \tag{1.1}$$

where A is the amplitude of the voltage playback, A_o is the amplitude of the voltage playback at zero spacing, k is the wave number of the recorded sine wave and d is the magnetic spacing. As shown in Figure 1.6, magnetic spacing is the sum of the flying height, the carbon overcoat thickness and the thickness of the lubricant. From Eq. 1.1, we see that the maximum amplitude of the voltage playback is achieved when the magnetic spacing d is zero. However, zero spacing would create tribological problems, such as friction, stiction and wear at the head disk interface. Hence, a thin (~8 to 10 nm) layer of air, the air bearing is maintained between the head and the disk.

The disk used in magnetic recording is a flat, circular piece of aluminum or glass with a magnetic coating upon which the digital information can be recorded. The disk has a rigid substrate, usually aluminum-magnesium alloy, which is typically 0.4 to 0.8 mm thick. The substrate is coated with several additional layers: an under-layer to help adhesion (~10 μm nickel phosphide); a layer of chromium (5-10 nm) to control orientation and grain size of magnetic layer; the magnetic layer 25-150 nm (50 nm PtCo with various additions of Ta, P, Ni, Cr); a protective carbon overcoat layer (1-10 nm); and finally a lubricant layer (0.5 to 2 nm) to reduce dynamic friction, stiction and wear of the head disk interface. A typical lubricant layer consists of a monolayer of long chain fluorocarbons like perfluorinated polyether (PFPE)). The magnetic layer forms a cellular

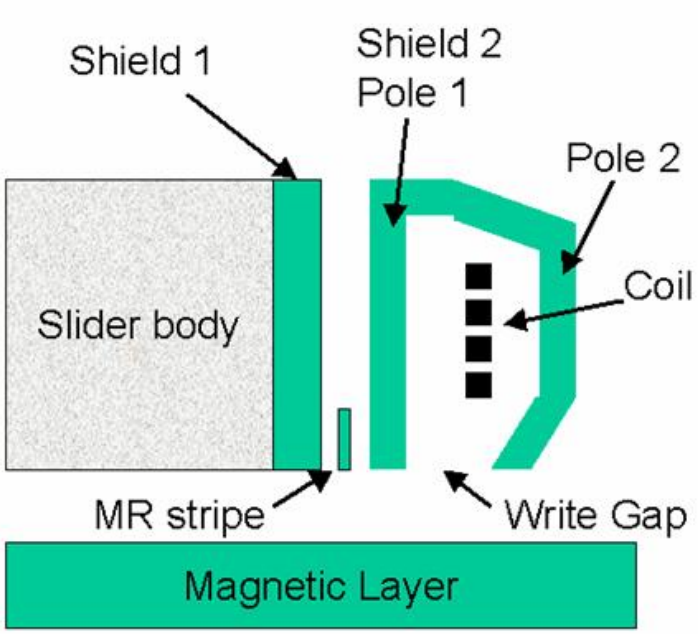

Figure 1.7: Cross section of MR read and inductive write head

structure of Co-rich magnetic cells in a non-magnetic matrix. These cells are similar to particulate recording media on a very fine scale. The slider also has a protective thin layer of carbon overcoat to avoid stiction. The pitch angle of the slider is very small, on the order of about 100 μrad, to maintain a constant flying height in the pole tip region of the write head (Figure 1.7).

1.5 Areal Density and Flying Height Evolution

The development of the MR and GMR heads in the early 1990's led to an increase of areal density of approximately 100% per year. Figure 1.8 shows the evolution of areal density over the past few decades since the first hard disk drive (IBM RAMAC)

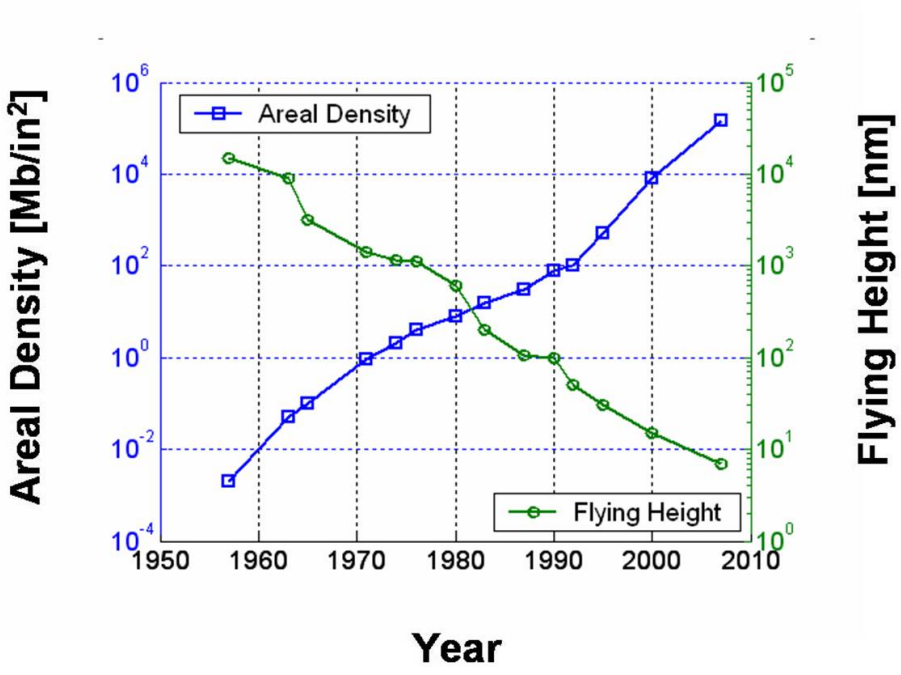

Figure 1.8: Areal density and flying height evolution

was introduced in the year 1956. The areal density has increased from 2 kb/in^2 for the RAMAC to about 150 Gb/in^2 for present hard disk drives. Figure 1.8 also shows the flying height evolution on the right hand scale. The flying height has been reduced significantly from about 20 μm in 1956 to about 8 - 10 nm today.

An important goal of the disk drive industry is to further increase the areal storage density. Another trend in recent years for hard disk drive technology has been the reduction in the form factor and to achieve compactness of the disk drive. The form factor of hard disk drives has decreased from a disk diameter of 600 mm (IBM RAMAC) to current disk diameters of 95 mm (3.5 in) for desktop computers, 65 mm (2.5 in) for laptop computers and 25 mm (1 in) or 21 mm (0.85 in) for "microdrives". The overall

form factor for the slider has also decreased to "Pico" [dimensions: 1.25 mm(length) $\times$ 1 mm(width) $\times$ 0.30 mm(thickness)] and "Femto" [dimensions: 0.85 mm(length) $\times$ 0.7 mm(width) $\times$ 0.23 mm(thickness)] designs. The corresponding air bearing surfaces have also evolved and are shown in Figure 1.9.

The slider material (Titanium Carbide / Alumina) has not changed since 1987. Ferrite sliders were used in hard disk drives manufactured before 1987. The mass of the slider has reduced over years from 55 mg for the “Mini” slider to 0.6 mg for the current “Femto” slider. The change in the read/write head technology and assembly has considerably helped in the reduction of the slider form factor and overall mass. The slider air bearing has also changed from machined two-rail design to etched-rail design and finally to the current five-pad etched pattern sliders designs.

With the increase in storage density and the reduction in the form factor of the disk drives, a new pool of wide-range applications have opened markets, no longer limiting hard disk drive usage only to computers, laptops and servers. Consumer applications such as MP3 music players, personal digital assistants (PDA’s), digital cameras, cellular phones, and television digital video recorders utilize hard disk drives for data storage and playback. Although recent trends indicate that the solid state (flash memory) storage technology has overpowered hard disk technology in small form factor drives, hard disk drives are the popular and best choice of storage for large volume data storage applications.

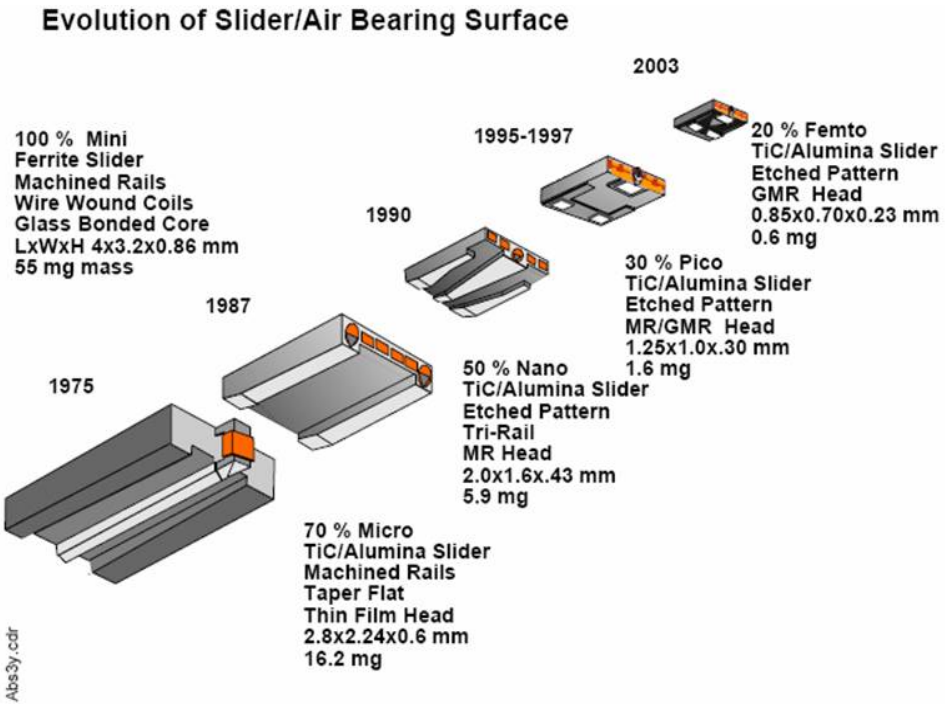

Figure 1.9: Evolution of slider form factors (source: Hitachi GST [6])

1.6 New and Prospective Storage Technologies

In recent years, the rate of growth of areal density in hard disk storage has slowed down due to a physical limit in magnetic recording. The magnetic material on the disk is composed of small grains. Each bit on a conventional magnetic medium covers approximately 100 such grains to ensure reliable storage of information. However, there is a lower limit for the grain size below which the magnetization may switch randomly due to thermal excitation. This limit is referred to as the "superparamagnetic limit".

Since the conventional longitudinal recording is approaching this limit, alternative recording technologies such as perpendicular magnetic recording (PMR) have emerged. Future technologies such as heat assisted magnetic recording (HAMR), discrete track recording (DTR), and bit-patterned media (BPM) are being researched extensively in industry as well as academia. The principle of these new recording technologies will be described in the next sections.

1.6.1 Perpendicular Magnetic Recording

The principle of perpendicular magnetic recording is shown in Figure 1.10. Distinct from longitudinal recording, the magnetized bits point up or down in perpendicular magnetic recording media. The main feature of the perpendicular recording media is the soft underlayer that conducts the magnetic flux. When the write head is energized, the magnetic flux concentrates under a small pole-tip and generates a magnetic field in the short gap between the pole-tip and soft underlayer. The recording layer on which

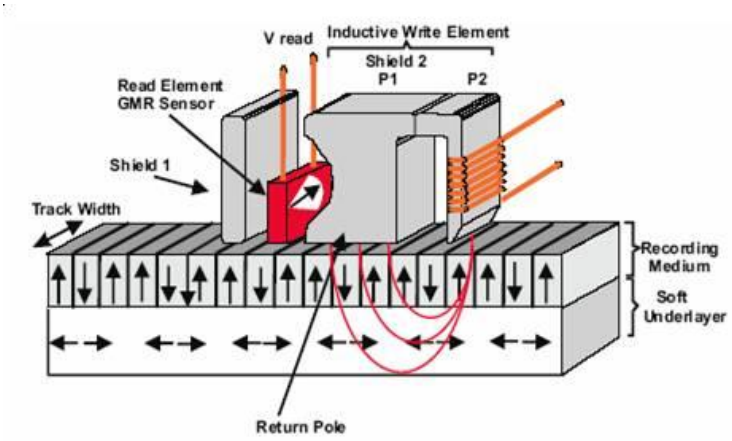

Figure 1.10: Schematic for perpendicular magnetic recording (source: Hitachi GST)

the data are stored is placed in this gap where the magnetic field is the highest. The soft underlayer assists in obtaining stronger readback signals and decreases interference from adjacent tracks.

At an areal density of 500 Gb/in^2, the superparamagnetic limit is likely to be reached [11]. Perpendicular magnetic recording technology may not be able to overcome the thermal stability problem beyond areal density of 500 Gb/in^2.

1.6.2 Heat Assisted Magnetic Recording

To overcome the thermal stability problem, it is necessary to increase the coercivity or magnetic anisotropy constant of the media. Present day magnetic heads cannot write on very high coercivity materials. HAMR solves this problem by heating the magnetic material above the Curie temperature and writing on it during the cooling process when the coercivity is still low. After cooling down to room temperature, the magnetization

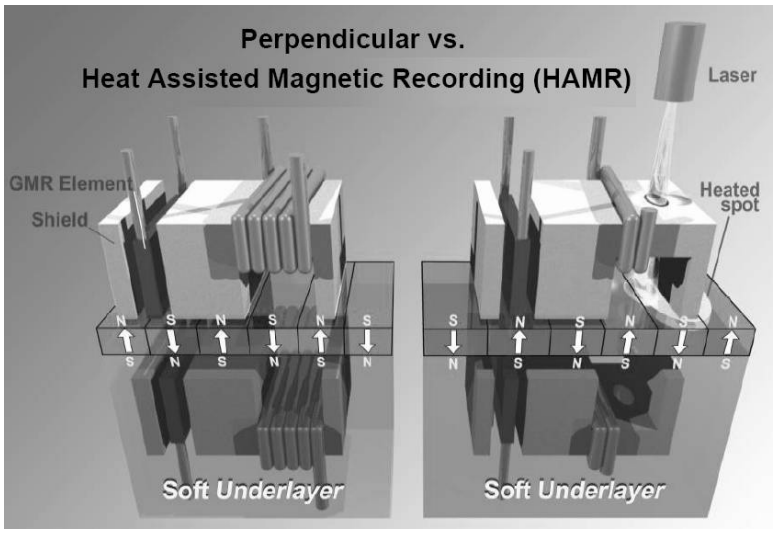

Figure 1.11: Perpendicular magnetic recording vs. Heat assisted magnetic recording (source: Seagate)

of a bit is frozen in.

Figure 1.11 shows a comparison of the principle of PMR and HAMR technologies. In HAMR technology a laser heats the medium locally to 300 degrees centigrade or higher befrore writing. HAMR technology is expected to extend the storage density to beyond 5 Tb/in^2.

1.6.3 Patterned Media for Magnetic Recording

Use of patterned media is a new approach of magnetic recording that has the potential of increasing the areal density beyond 1 Tb/in^2. There are two approaches in patterned media recording. One is the discrete track recording (DTR) and the other is bit patterned media (BPM). In DTR, the bits are stored on discrete circumferential tracks

on the disk (see Figure 1.12(a)). Since the information is stored on discrete tracks, cross talk between bits in the radial direction on the disk can be eliminated. The width and depth of the so-called “grooves” between two such tracks are typically on the order of 40 to 100 nm.

In bit patterned media, each bit is stored on a single magnetic domain or “island” as shown in Figure 1.12(b). Each island on BPM may be composed of one grain or several exchange coupled grains. Magnetic transitions no longer occur between random grains, since distinct boundaries between islands are formed both in the circumferential and the radial directions on the disk. Since each island is a single magnetic domain, BPM is thermally stable at densities higher than can be achieved with the conventional media.

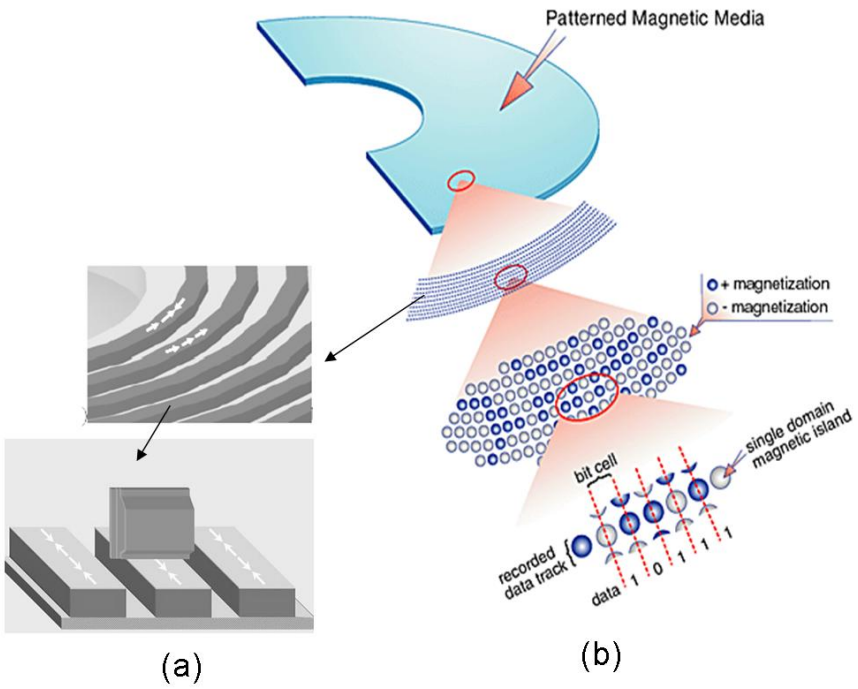

Figure 1.12: Schematic for (a) Discrete track recording [source: Komag] and (b) Bit patterned media [source: Hitachi GST]

1.7 Outline of the Thesis

This thesis covers many topics of mechanics and tribology concerning the hard disk drive technology. These topics include the effect of shock, vibration, enclosure design, surface texture and surface pattern on the dynamics of the head disk interface. The details of the theory involved, experimental and numerical procedures and corresponding results are organized into several chapters and are outlined as follows.

Chapter 1 has given an introduction into magnetic recording for storage in hard disk drives; mechanical components of a typical hard disk drive; storage areal density and flying height evolution over the years since the production of the first hard disk drive. Then an overview of the head disk interface, and the recent trends and applications of the hard disk drives for data storage along with the current outline of this thesis is given.

Chapter 2 provides an overview of the numerical models developed, the simulation procedure, the theory and the experimental techniques used in this dissertation.

Chapter 3 discusses the detailed finite element simulation of non-operational shock in a typical load/unload hard disk drive. A finite element model of a hard disk drive (HDD) was developed to study the effect of non-operational shock on load/unload type disk drive suspensions. The effect of shock amplitude, pulse width, suspension thickness, and flexure thickness, on the magnitude of lift-tab separation and dimple separation due to a shock event is studied.

Chapter 4 gives a detailed description of the effect of both non-operational and operational shock on different form factor hard disk drives. This chapter discusses both experimental and numerical results for shock performance in 3.5 inch form factor disk drives (used in desktop and server applications) and 2.5 inch form factor disk drives (used in laptop and MP3 applications).

Chapter 5 discusses shock and vibration applied to 1-inch form factor disk drives (used in digital cameras, PDA's, etc.), generally referred to as "microdrives". Chapter 5 also describes the effect of the disk drive enclosure design on the dynamics of the head

disk interface.

Chapter 6 describes the theory of hydrodynamic lubrication for the head disk interface. This chapter describes the derivation of the governing equation (Reynolds equation) for hydrodynamic lubrication of pivoted slider bearings. Finite element solutions of the steady state and the time-dependent Reynolds equation are derived in Chapter 7.

Chapter 8 describes an investigation of surface texture and the potential benefits of surface texture in improving the tribological performance of the head disk interface. Surface texture is numerically implemented in high pressure regions of the slider air bearing. Flying characteristics of textured sliders are compared to that of untextured sliders.

Chapter 9 describes the numerical simulations of the head disk interface for patterned media. The pattern is transferred onto the slider surface from the disk surface (as in Bit Patterned Media) and steady state pressure generation is investigated. The dynamic excitation of the slider due to pattern in the head disk interface is also studied.

The conclusions of this dissertation are given in Chapter 10.

Bibliography

[1] IBM 305 RAMAC, www-03.ibm.com/ibm/history/exhibits/storage

[2] Mitsuya, Y., "Nano-Technologies for Head-Medium *Interface* in Magnetic Disk Storage", *Proceedings of the 1997 International Symposium on Micromechatronics and Human Science*, pp 27-32, 1997

[3] Li, H., Liu, B., Hua, W., and Chong, T.-C., "Intermolecular Force, Surface Roughness, and Stability of Head-Disk Interface", *Journal of Applied Physics*, 97, 10P305, 2005

[4] B. Bhushan, "Tribology and Mechanics of Magnetic Storage Devices", *Second Edition, Springer*, 1996

[5] Michael Kanellos, "Hitachi Ships its Terabyte Drive", *News Article, CNET News.com,* 2007

[6] Hitachi Global Storage Technologies, www.hitachigst.com

[7] Toshiba Inc., http://sdd.toshiba.com

[8] R. Wood, "The Feasibility of Magnetic Recording at 1 Terabit per Square Inch", *IEEE Transactions on Magnetics*, Vol. 36, No. 1, pp.36-42, 2000

[9] C. D. Mee and E. D. Daniel, "Magnetic Recording: Technology", Volume 1, McGraw-Hill, 1987

[10] S. Khizroev, and D. Litvinov, "Perpendicular Magnetic Recording: Writing Process", *Journal of Applied Mechanics*, Vol. 95, No. 9, 4521-4537, 2004

[11] Bertram, N., Williams, M., "SNR and Density Limit Estimates: A Comparison of Longitudinal and Perpendicular Recording", *IEEE Transactions on Magnetics*, Vol. 36, No.1, pp. 4-9, 2000

[12] Wood, R., Hsu, Y., and Schultz, M., "Perpendicular Magnetic Recording Technology", *White Paper, HitachiGST Technical Library,* (2006)

2

Numerical Models and Simulation Procedures

2.1 Shock Simulation in Hard Disk Drives

2.1.1 Introduction to Shock Loads

Shock occurs when a force, a position, a velocity, or an acceleration is abruptly modified and creates a transient state of vibrations in the system considered [1]. Shock is defined as a vibratory excitation having a time duration between the natural period of the excited mechanical system and two times that period [1].

A shock whose signal can be represented exactly in mathematical terms is called a simple shock. Standards generally specify half-sine, rectangular (impulse), or step type shock.

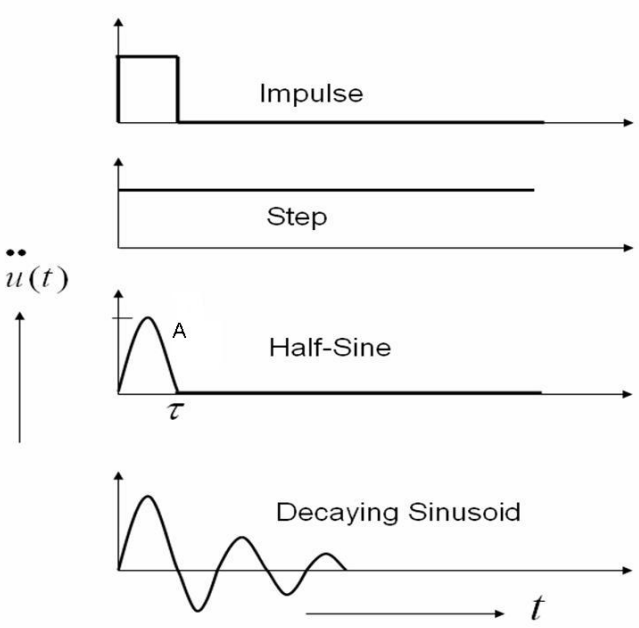

Figure 2.1: Typical types of shock input

Typical shock types [1] are shown in Figure 2.1. In the shock investigations in this dissertation, the half-sine acceleration is used as shock input. It is given by

$$\ddot{u}\,(t) = A \sin\left(\frac{\pi t}{\tau}\right) \qquad [0 < t < \tau] \tag{2.1}$$

and

$$\ddot{u}\,(t) = 0 \qquad [t < 0;\, t > \tau] \tag{2.2}$$

The velocity is described by Eq. (2.3) for time interval between 0 and τ, and Eq. 2.4 for time greater than τ .

$$\dot{u}\left(t\right)=\frac{A\tau}{\pi}\left(1-\cos\frac{\pi t}{\tau}\right)\qquad\left[0<t<\tau\right] \tag{2.3}$$

$$\dot{u}\left(t\right)=\frac{2A\tau}{\pi}\qquad\left[t>\tau\right] \tag{2.4}$$

Similarly, the displacement is described by Eq.2.5 and Eq. 2.6.

$$u\left(t\right)=\frac{A\tau^{2}}{\pi^{2}}\left(\frac{\pi t}{\tau}-\sin\frac{\pi t}{\tau}\right)\qquad\left[0<t<\tau\right] \tag{2.5}$$

$$u\left(t\right)=\frac{A\tau^{2}}{\pi}\left(\frac{2t}{\tau}-1\right)\qquad\left[t>\tau\right] \tag{2.6}$$

Shock is generally quantified using the shock response spectrum (SRS). Biot [], proposed a method consisting of applying the shock under consideration to a standard mechanical system, which does not duplicate the model of the real structure. Instead, it is composed of a support and of N linear single-degree-of-freedom (SDOF) resonators, each comprised of a mass m_i, a spring of stiffness k_i, and a damper c_i. The dampers are chosen such that the damping ratio $\xi = c_i \diagup 2\sqrt{k_i m_i}$ is the same for all N resonators. When the support is subjected to shock, each mass has a specific displacement response according to its natural frequency and to the chosen damping ratio, while a stress is induced in the element.

A hard disk drive experiences shock either due to impact with another rigid object or due to free fall because of gravity. Figure 2.2 shows a single-degree-of-freedom system subject to a free-fall due to gravity.

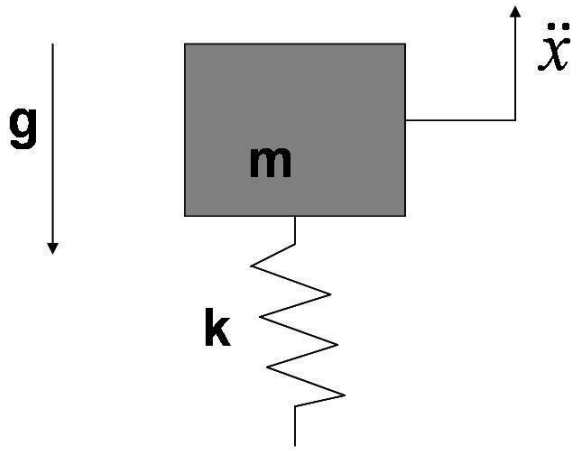

Figure 2.2: Single degree of freedom model subject to free fall due to gravity

In Figure 2.2, m is the mass, k is the spring stiffness, x is the absolute displacement of the mass (the double dot denotes acceleration), g is the gravitational acceleration. Let us assume that the object is dropped from rest and that there is no energy dissipation. Furthermore, we assume that the object remains attached to the floor via the spring after initial contact and the collision is perfectly elastic. We also assume that the object freely vibrates at its natural frequency after contact and the system has a linear response.

The initial velocity of the system as it strikes the ground can be found by equating the change in kinetic energy and the change in potential energy as shown below:

$$\frac{1}{2}m\dot{x}^2 = mg\Delta h \tag{2.7}$$

where Δh is the drop height. Thus, the initial velocity when the mass encounters the

floor is

$$\dot{x}(0) = \sqrt{2g\Delta h} \tag{2.8}$$

Furthermore, the initial displacement is assumed to be zero.

$$x(0) = 0 \tag{2.9}$$

Assume a displacement equation with constant coefficients a and b of the form:

$$x(t) = a \sin \omega_n t + b \cos \omega_n t \tag{2.10}$$

where ω_n is natural frequency of the system and is given by

$$\omega_n = \sqrt{\frac{k}{m}}$$

The zero displacement initial condition requires $b = 0$.

Thus, the displacement is

$$x(t) = a \sin \omega_n t \tag{2.11}$$

and the velocity is

$$\dot{x}(t) = a\omega_n \cos \omega_n t \tag{2.12}$$

Using Eq. (2.8), we can determine the constant a as follows:

$$a = \frac{\sqrt{2g\Delta h}}{\omega_n} \tag{2.13}$$

Substituting Eq. (2.13) into Eq. (2.11), the displacement, velocity and acceleration are:

$$\begin{aligned} x(t) &= \frac{\sqrt{2g\Delta h}}{\omega_n} \sin \omega_n t \\ \dot{x}(t) &= \sqrt{2g\Delta h} \cos \omega_n t \\ \ddot{x}(t) &= -\omega_n \sqrt{2g\Delta h} \sin \omega_n t \end{aligned} \tag{2.14}$$

The force transmitted through the spring is $f(t) = kx$. Using the definition $k = {\omega_n}^2 m$ and the displacement from Eq. (2.14), we can write the force $f(t)$ as:

$$f\left(t\right) = \omega_n m \sqrt{2g\Delta h} \sin \omega_n t \tag{2.15}$$

The total impulse I^*over a half-sine period can be obtained by integrating the force transmitted through the spring over the time interval as:

$$I^* = \int_0^{\pi/\omega_n} \left[f\left(t\right)\right] dt \tag{2.16}$$

Substituting Eq. (2.15) in Eq. (2.16), we get:

$$I^* = \int_0^{\pi/\omega_n} \left[\omega_n m \sqrt{2g\Delta h} \sin \omega_n t\right] dt \tag{2.17}$$

Integrating with respect to time,

$$I^* = -\omega_n m\sqrt{2g\Delta h}\left[\frac{1}{\omega_n}\right]\cos\omega_n t\,\Big|_0^{\pi/\omega_n} \tag{2.18}$$

$$I^* = 2m\sqrt{2g\Delta h} \tag{2.19}$$

A single degree of freedom model subjected to half-sine base excitation is discussed in Chapter 3 along with the finite element numerical simulation.

2.1.2 Shock in Hard Disk Drives:

Dropping, hitting, or striking a hard disk drive against a rigid surface can damage the disk drive. Even if there is no visible evidence of external damage, a hard disk drive subject to shock may completely fail during the initial use itself, or its reliability could deteriorate rapidly. There are two possible states of the disk drive when a shock event can occur. The state when the hard disk drive is not powered is referred to as the "non-operational" state of the drive. When the disk spindle is powered and the disk is spinning, the head flies over the disk forming an air bearing. This state of the disk drive is referred to as the "operational" state of the drive. The shock events in the non-operational case usually have short durations but high amplitudes. However, operational shock events typically have longer durations but lower amplitudes. Based on current technology, there are two types of hard disk drives. One is the “contact-start-stop" (CSS) drive and the other is the “load/unload" (L/UL) [5] drive. A schematic of these two technologies is shown in Figure2.3.

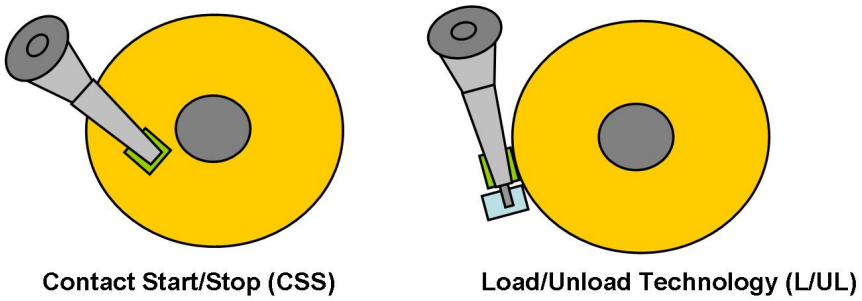

Figure 2.3: Schematic of Contact Start/Stop and Load/Unload Technologies

In CSS drives, the slider rests on a dedicated landing/textured zone when the drive is turned off. When the drive is turned on and the disk starts spinning, an air bearing is formed between the slider and the disk and the slider starts to fly over the disk at a certain disk velocity. In order to reduces stiction of the head disk interface, the CSS landing zone has a higher surface roughness than the very smooth data zone. Since the slider is in contact with the disk surface during take-off, wear of the slider and the disk is a serious tribological problem in CSS disk drives. Another common issue in non-operational CSS disk drives is the so-called “head-slap" due to mechanical shock. Head-slap occurs when the shock amplitude is large enough to cause the separation of the head from the disk surface, then it ’slaps’ onto the disk again, often repeatedly. The head-slap event can cause the head to damage the disk surface, leaving behind wear debris in the head/disk interface region. If the debris lands on the data zone of the media, data errors may occur.

Currently, most disk drives employ load/unload technology. During non-operation,

the suspension is parked on a ramp adjacent to the outer diameter of the disk. The suspension is designed with a small lift-tab that can move along the ramp in the radial direction of the disk. The slider is lowered onto the disk only when the disk is spinning at a certain velocity. Loading and unloading can be achieved without the slider and disk surfaces contacting one another. Wear of the head disk interface due to starting and stopping (CSS) is minimized using L/UL technology. In the non-operational state, load/unload drives have better shock performance than CSS drives since the slider is not in contact with the disk and head-slap does not occur. However, in the L/UL scenario, the lift-tab on the ramp may break during the non-operating state of the drive due to shock. Hard disk drives need to be mechanically robust to sustain shock amplitudes to specified levels for reliable operation.

2.1.3 Simulation Procedure for Non-operational Shock in HDD

A geometric model of the actuator arm, suspension, gimbal, slider, disk, base, ramp and electrical components was developed using Pro-Engineer Wildfire [7] (commercially available 3-D Computer Aided Design software). The geometry was then saved as an IGES (Initial Graphics Exchange Specification) file format which stores the geometry as a combination of lines and surfaces in a digital format. This file can be imported into most finite element software programs. Altair Hypermesh [8] was used in this study. A finite element mesh was created for the HDD components. The finite element model of a typical hard disk drive used in this dissertation is shown in Figure 2.4.

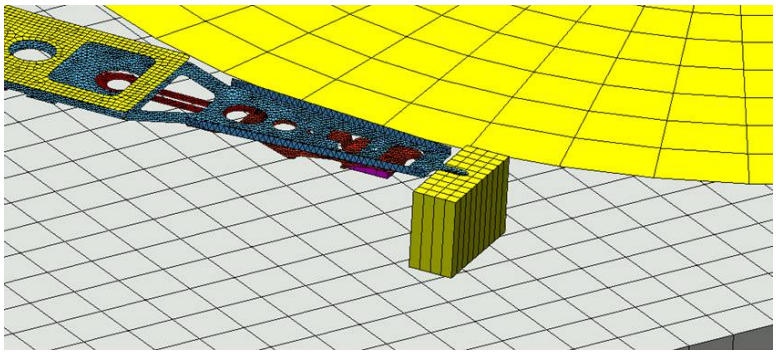

Figure 2.4: Finite element model of typical load/unload HDD

Loads and boundary conditions were applied to the finite element model. The shock load is defined as an acceleration impulse, and is modeled as a half-sine acceleration impulse of 0.5 to 2 ms duration. This acceleration impulse is applied at the base of the disk drive model to simulate shock. The level of shock in terms of G's (1 G = 9.81 m/s^2) is the amplitude of the half-sine input. A typical shock input applied to the hard disk drive model is shown in Figure 2.5.

Contact surfaces were defined between the suspension, gimbal and slider at the dimple and limiter areas. The finite element model is created with solid and shell elements. The suspension, gimbal (flexure), disk and electrical leads are modeled using shell elements. The base, actuator arm, ramp, and slider are modeled using solid elements. The finite element model of the disk drive and the boundary conditions are saved in a format appropriate for the finite element solver used in this study (LS-Dyna). LS-Dyna [2] is a commercially available non-linear finite element solver (see Section 2.4) used to obtain the transient response of the structural components of the hard disk drive model subject

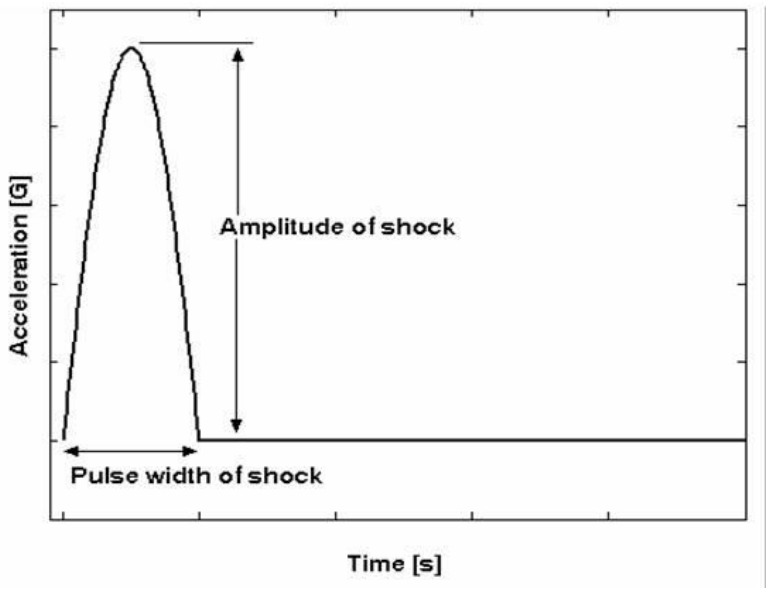

Figure 2.5: Schematic of half-sine acceleration load curve for shock

to a shock event. The amplitude and pulse width of the shock loading were varied to study the effect of shock on the deflection and stress in the head-suspension assembly.

2.2 Operational Shock Simulation of the Head Disk Interface

Operational shock occurs when the magnetic read/write head is flying over the spinning disk at the design flying height. If the amplitude of shock is large enough to break the air bearing between the slider and the disk, the slider may crash into the disk surface which could cause failure of the head disk interface. The highest amplitude of operational shock that can be sustained by the hard disk drive without causing failure of

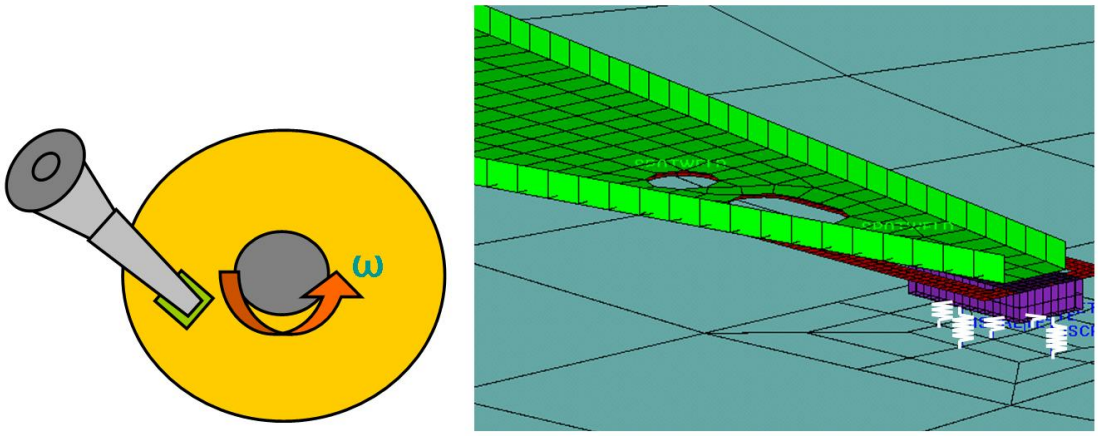

Figure 2.6: Schematic for operational shock simulation and air bearing stress definition

the head disk interface is the "operational shock specification" for that particular disk drive. The operational shock specification for a hard disk drive is typically lower than the non-operational shock specification.

2.2.1 Simulation Procedure for Operational Shock in HDD

A finite element model for the operational shock was developed by using the same components as the non-operational HDD model. In the operational shock model, the head suspension assembly is positioned over the disk and supported by an air bearing. The air bearing between the slider and the disk is modeled by using linear springs. The shock input is applied to the base of the hard disk drive model to simulate linear shock.

Figure 2.6 shows a schematic of the head disk interface and the finite element model used for operational shock simulation. The spring connecting the center of the slider

to the disk represents the stiffness of the air bearing in the z-direction. Two springs connecting centers of the trailing edge and the leading edge of the slider represent the pitch stiffness of the air bearing. Two springs connecting centers of the inner edge and the outer edge of the slider represent the roll stiffness of the air bearing. The air bearing stiffness values are obtained from a finite element solution of the time dependent Reynolds equation for hydrodynamic lubrication (see Chapters 6 and 7).

2.3 Vibrations in Hard Disk Drives

The motion of a structure due to an oscillating force applied to a mechanical system is generally referred to as vibrations. Vibrations may be described as deterministic or random. Deterministic vibrations follows a periodic, established pattern such that the amplitude of the vibration at any point in time is known from the past time history. If the vibration is random, then future events cannot be predicted from the past time history. However, the probability of occurrence of particular magnitudes and frequencies of random vibrations can be quantified in statistical terms. Hard disk drives usually encounter vibrations that are random in nature.

2.3.1 Simulation of Random Vibrations in HDD's

The simulation procedure for vibration loads applied to hard disk drives is similar to the procedure for shock simulation. The half sine shock input is replaced by a random

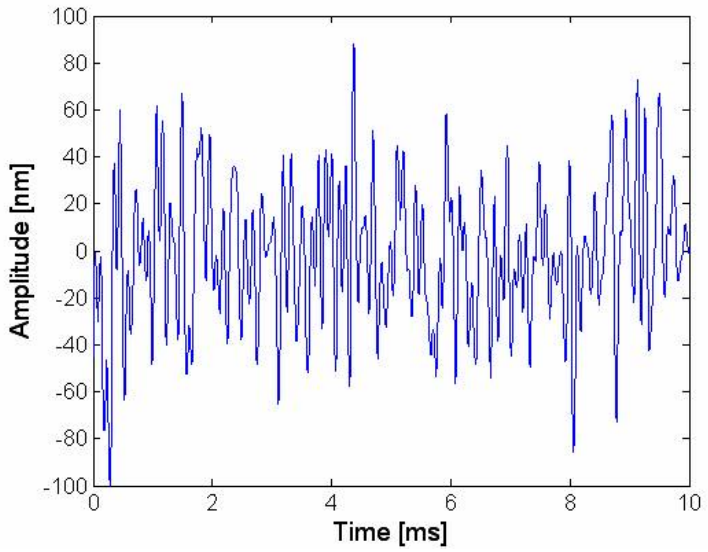

Figure 2.7: Typical random vibration input applied to the hard disk drive model

vibration input, as shown in Figure 2.7.

The peak-to-peak amplitude and the frequency band of the vibration input can be controlled. This vibration input can be applied to the disk drive model in x, y and z directions to investigate the response of the head disk interface to random vibrations. Details of the simulation results and the effect of vibrations on the head disk interface is given in Chapter 5.

Figure 2.8 shows how a vibration input is applied in x, y and z directions.

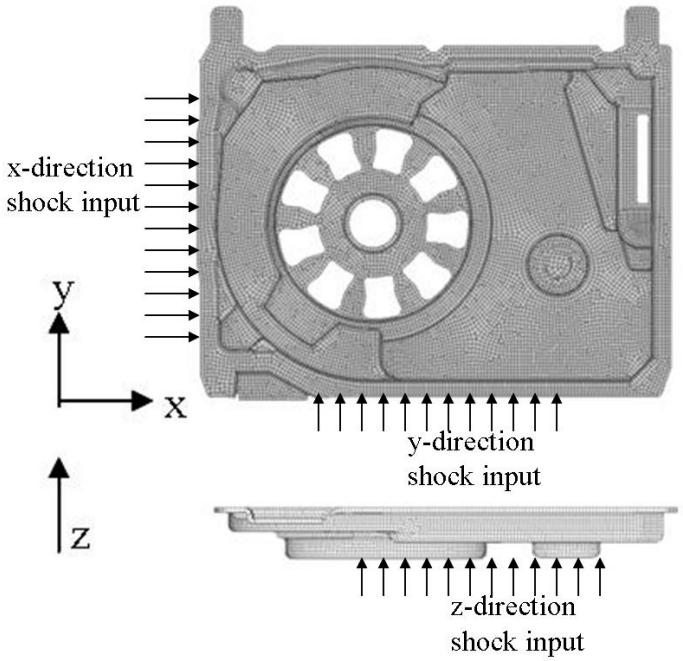

Figure 2.8: Schematic to show how x,y and z vibration input is applied

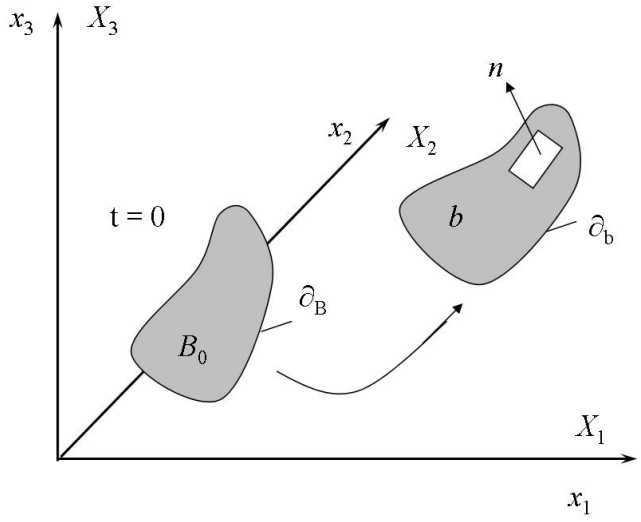

Figure 2.9: Notation for finite element formulation in the non-linear solver

2.4 Theory of Non-Linear Solver (LS-Dyna) used in Shock and Vibration Simulations

2.4.1 Governing Equations

The objective is to obtain the time-dependent deformation in which a point in b (see 2.9), initially at X_a (α =1,2,3) in a fixed rectangular Cartesian coordinate system, moves to a point x_i (i=1,2,3) in the same coordinate system. A Lagrangian formulation [1], [2] is used and the deformation is expressed as follows:

$$x_i = x_i\left(X_\alpha, t\right) \tag{2.20}$$

with the following initial conditions:

$$\begin{aligned} x_i\left(X_\alpha, t=0\right) &= X_\alpha \\ \dot{x}_i\left(X_\alpha, t=0\right) &= V_i\left(X_\alpha\right) \end{aligned} \tag{2.21}$$

where V_i defines the initial velocities.

LS-Dyna [2] is a non-linear finite element solver. The derivation of the governing equations in LS-Dyna starts with the momentum equation given as below:

$$\sigma_{ij,j} + \rho f_i = \rho \ddot{x}_i \tag{2.22}$$

Appendix A describes the detailed derivation [2] and manipulation of the momentum equation and boundary conditions to obtain a weak form of the equilibrium equations as follows:

$$\delta\pi = \int_v \rho \ddot{x}_i \delta x_i dv + \int_v \sigma_{ij} \delta x_{i,j} dv - \int_v \rho f_i \delta x_i dv - \int_{\partial b_1} t_i \delta x_i ds = 0 \tag{2.23}$$

Eq. (2.23) is referred to as the principle of virtual work: "the principle stating that the total virtual work done by all the forces acting on a system in static equilibrium is zero for a set of infinitesimal virtual displacements from equilibrium".

A mesh of finite elements that are connected by nodal points (or nodes) is superimposed on the reference body and nodal parameters are tracked through time.

$$x_i\left(X_\alpha, t\right) = x_i\left(X_\alpha\left(\xi, \eta, \zeta\right), t\right) = \sum_{j=1}^{k} \phi_j\left(\xi, \eta, \zeta\right) x_i^j\left(t\right) \tag{2.24}$$

In Eq. (2.24) k is the number of nodal points defining the element, x_i is the nodal coordinate of the j^{th} node in the i^{th} direction, and ϕ_j are the interpolation or shape functions of the parametric coordinates (ξ, η, ζ).

Summing over n finite elements on the body, Eq. (2.23) can be approximated as follows:

$$\delta\pi = \sum_{m=1}^{n} \delta\pi_m = 0 \tag{2.25}$$

Eq. (2.25) is then written as:

$$\delta\pi = \sum_{m=1}^{n} \left\{ \int_{v_m} \rho\ddot{x}_i \Phi_i^m dv + \int_{v_m} \sigma_{ij}^m \Phi_{i,j}^m dv - \int_{v_m} \rho f_i \Phi_i^m dv - \int_{\partial b_1} t_i \Phi_i^m ds \right\} = 0 \tag{2.26}$$

where

$$\Phi_i^m = \left(\phi_1, \phi_2, \phi_3, \ldots\ldots\ldots \phi_k\right)_j^m \tag{2.27}$$

Eq. (2.26) can be written in matrix notation as follows:

$$\sum_{m=1}^{n} \left\{ \int_{v_m} \rho N^T N a dv + \int_{v_m} B^T \sigma dv - \int_{v_m} \rho N^T b dv - \int_{\partial b_1} N^T t ds \right\}^m = 0 \tag{2.28}$$

where N is the interpolation matrix, B is the strain-displacement matrix, a is the nodal acceleration vector, b is the body force vector, t is the traction force vector, and σ is the stress vector.

Using the sinulation procedures described in the previous sections of this chapter, an input file for LS-Dyna is generated in Altair Hypermesh program. The input file for LS-Dyna solver contains all the finite element model information such as the nodes, elements, materials, thickness properties. The input file also contains the boundary conditions such as the displacement constraints, shock or vibration load curves, contact definitions, etc. LS-Dyna uses the above referenced theory to compute the displacement, velocity, acceleration for each node in the finite element model of the input file and also the stress and strain in each element. The values for displacment, velocity, acceleration, stress and strain are computed for each time step in the simulation and stored in a result file. This result file can be loaded back in Hypermesh to review the results.

2.4.2 Solid Elements

For a mesh of a 8-noded hexahedron solid elements, Eq. (2.24) becomes

$$x_i\left(X_\alpha, t\right) = x_i\left(X_\alpha\left(\xi, \eta, \zeta\right), t\right) = \sum_{j=1}^{8} \phi_j\left(\xi, \eta, \zeta\right) x_i^j\left(t\right) \tag{2.29}$$

The shape function ϕ_j for the 8-node hexahedron is written as

$$\phi = \frac{1}{8}\left(1 + \xi\xi_j\right)\left(1 + \eta\eta_j\right)\left(1 + \zeta\zeta_j\right) \tag{2.30}$$

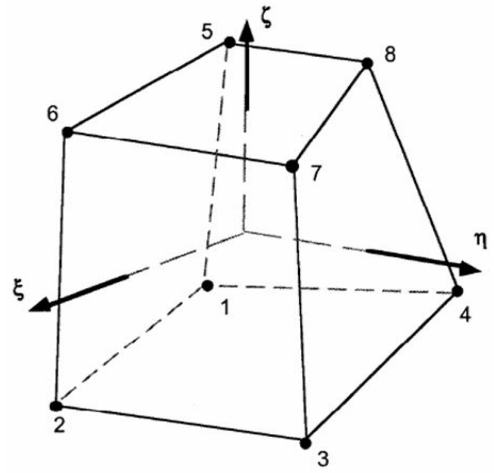

Node	ξ	η	ζ
1	-1	-1	-1
2	1	-1	-1
3	1	1	-1
4	-1	1	-1
5	-1	-1	1
6	1	-1	1
7	1	1	1
8	-1	1	1

Figure 2.10: 8-node solid hexahedron element

where ξ_j, η_j, ζ_j use unit values of $(\pm 1, \pm 1, \pm 1)$ and x_i^j is the nodal coordinate of the j^{th} node in the i^{th} direction (Figure 2.10).

For a solid element, the shape function N is a 3×24 rectangular interpolation matrix given by:

$$N(\xi, \eta, \zeta) = \begin{bmatrix} \phi_1 & 0 & 0 & \phi_2 & 0 & \cdots & 0 & 0 \\ 0 & \phi_1 & 0 & 0 & \phi_2 & \cdots & \phi_8 & 0 \\ \phi_1 & 0 & \phi_1 & 0 & 0 & \cdots & 0 & \phi_8 \end{bmatrix} \tag{2.31}$$

The stress vector is given as:

$$\sigma = (\sigma_{xx}, \sigma_{yy}, \sigma_{zz}, \sigma_{xy}, \sigma_{yz}, \sigma_{zx}) \tag{2.32}$$

B is the 6×24 strain-displacement matrix

$$B = \begin{bmatrix} \frac{\partial}{\partial x} & 0 & 0 \\ 0 & \frac{\partial}{\partial y} & 0 \\ 0 & 0 & \frac{\partial}{\partial z} \\ \frac{\partial}{\partial y} & \frac{\partial}{\partial x} & 0 \\ 0 & \frac{\partial}{\partial z} & \frac{\partial}{\partial y} \\ \frac{\partial}{\partial x} & 0 & \frac{\partial}{\partial x} \end{bmatrix} \cdot N \tag{2.33}$$

2.4.3 Shell Elements

The shell element formulation used by the LS-Dyna non-linear solver is based on the derivation by Belytschko and Tsay in 1981. The Belytschko-Lin-Tsay shell element [4] was implemented in LS-Dyna as an alternative to the Hughes-Liu shell element. This was done since the Belytschko-Lin-Tsay shell element is computationally more efficient than the Hughes-Liu shell element. For a shell element with five (through thickness) integration points, the Belytschko-Lin-Tsay shell elements require 725 mathematical operations compared to 4066 operations for the under-integrated Hughes-Liu element. The Belytschko-Lin-Tsay shell element is usually the shell element formulation of choice and also the default shell element formulation in LS-Dyna.

The Belytschko-Lin-Tsay shell element is based on a combined co-rotational and velocity-strain formulation. The efficiency of the element is obtained from the mathematical simplifications that result from these two kinematic assumptions.

Bibliography

[1] C. M. Harris and A. G. Piersol, “Harris’ Shock and Vibration Handbook” Fifth Edition, *McGraw-Hill*, 2002

[2] Hallquist, J., “LS-Dyna Users Manual”, Livermore Software Technology Corp. 1998

[3] Hallquist, J., “LS-Dyna Theory Manual”, Livermore Software Technology Corp. 1998

[4] Belytschko, T., Lin, J., and Tsay, C.S., “Explicit Algorithms for Nonlinear Dynamics of Shells”, Comp. Meth. Appl. Mech. Eng., 42, 225-251, 1984[a]

[5] Albrecht, T.R., “Load/Unload Technology for Disk Drives”, IEEE Transactions on Magnetics, 35, No. 2, 857-862

[6] Albrecht, M., Rettner, C.T., Thomson, T., McClelland, G.M., Hart, M.W., Anders, S., Best, M.E., Terris, B.D., "Magnetic Recording on Patterned Media", *Joint NAPMRC 2003*, 6-8 Jan. 2003 Pg 36

[7] Parametric Technology Corporation, “Introduction to Pro/Engineer Wildfire 3.0, Parametric Technology Corporation, 2006

[8] Altair Computing, Inc., “Hypermesh 6.0 Documentation”, Altair Computing, Inc.

[9] Singiresu S. Rao, “Mechanical Vibrations”, Third Edition, Addison-Wesley Publishing, 1995

3

Non-operational Shock Simulation in a Load/Unload Hard Disk Drive

3.1 Overview

Mechanical shock is an important consideration for the durability and performance of a hard disk drive. High shock loads are prevalent when the form factor of the drive is small, or when the disk drive is used in hand-held electronic devices. Such devices may experience shock loads as high as 3000G. Load/unload (L/UL) technology is prevalent in most hard disk drives currently on the market. The head/disk interface (HDI) of load/unload drives is less severely stressed than the HDI of contact start/stop (CSS) drives. In addition, L/UL technology has better shock performance as the head is "parked" on the ramp and not in contact with the disk during rest. Furthermore, the

capacity of L/UL disk drives has increased because more disk space is available for data storage. Improved shock performance during the non-operational state of a hard disk drive is highly desirable. However, even if head/disk interactions are absent, other failure modes may occur such as lift-tab damage and dimple separation leading to flexure damage during a non-operational shock.

A number of investigations have been made to study the response of the head disk interface subject to non-operational shock in disk drives. Most of the published studies have been for disk drives employing the CSS technology where the head is parked on a specified location on the disk. Edwards [1] developed a finite element model to study the effect of non-operational shock and head-slap behavior for a constant drop height and various impact surfaces. The model was also verified experimentally by laser Doppler vibrometry (LDV). In another investigation, Aristegui and Geers [2] used an estimate of impact velocity in their finite element model to simulate linear shock response in hard drives. In a more recent investigation, Jayson et al [3] studied the head slap behavior during non-operational shock for both linear and rotary shock inputs. Lee et al [4] developed a theoretical model to investigate head slap quantitatively and design a shock resistant suspension by using Hamilton's principle to formulate the equations of motion. Haeng-Soo Lee et al [5] studied the effect of the inclusion of a dynamic absorber to the actuator arm to improve shock resistance. They concluded that the slider lift-off acceleration level could be increased with the application of a dynamic absorber. All of these studies focused on non-operational shock response in disk drives using CSS

technology.

Several papers have been published in the area of L/UL disk drive technology, but mainly to study the dynamics of the head during the load and unload processes. Zeng et al [6] developed a three degree of freedom (DOF) L/UL model with three springs and three dampers to study the L/UL lift-tab and ramp interaction during the unload process. Zeng and Bogy [7] later improved the three DOF model to a simplified four DOF L/UL model to numerically compute the pitch changes due to lift-tab movement. The model was used to calculate the force applied by the ramp during L/UL process. Weissner et al [8] developed a finite element based suspension model which automatically included the mass of the system including the suspension mass by using C1 continuous beam elements. They studied the dynamics of the head during the load unload process. They also investigated the different states of the suspension during the L/UL process with the inclusion of displacement limiters. Zeng and Bogy [9] also studied the effect of suspension limiters on the dynamics L/UL process numerically. They found that the air bearing design, the unload speed, the limiter gap, the limiter offset and the limiter stiffness had significant effect on the unload process.

This chapter describes the simulation of non-operational shock for a typical L/UL type head suspension assembly (HSA) using finite element analysis. The effects of shock amplitude, shock pulse width and design parameters on shock are studied for non-operational conditions and the results are compared with the trends obtained from a single degree of freedom (SDOF) model. In addition, the design of the so-called "sus-

pension limiter" is studied and its influence on the maximum von Mises stress predicted in the suspension-flexure beams due to shock is investigated.

3.2 Numerical Load/Unload Model

A finite element model of the hard disk drive (HDD) was created using Altair Hyperworks [10] as explained in Chapter 2. The HDD components modeled are the actuator arm, the suspension, the head gimbal assembly (HGA), the base, the load/unload ramp and the disk. The finite element model consists of solid elements and shell elements. The base of the HDD, the slider and the ramp are modeled with constant stress solid elements (Chapter 2). The disk, the actuator arm, the suspension and the gimbal are modeled using Belytschko-Lin-Tsay shell (Chapter 2) elements with uniformly reduced integration [11]. Figure 3.1 shows the finite element model of a typical L/UL HDD with the suspension on the ramp. Shock inputs were modeled as half-sine accelerations with various amplitudes and pulse widths. This acceleration was applied to the base of the hard disk drive to simulate a shock event.

Contact pairs were defined between the suspension and the gimbal (flexure), the suspension lift-tab and the ramp, and the slider and the gimbal surface. The contact algorithm used is a surface to surface contact with one surface being assigned as "master" surface and the other surface being a "slave" surface. The elements of the suspension lift-tab directly above the ramp surface act as slave elements and the elements on the

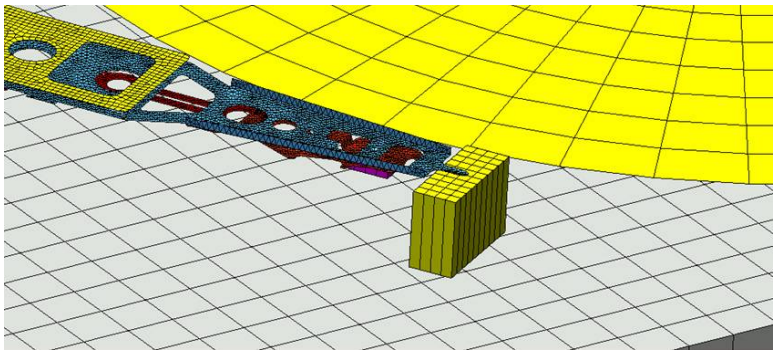

Figure 3.1: Finite element model of typical load/unload HDD

top surface of the ramp act as master elements in the contact definition. This algorithm ensures that the slave elements do not penetrate the master elements by using a penalty method. The contact force is determined by using the penalty method, which applies a reaction force proportional to the penetration distance at an interfering node. Energy is dissipated through the coefficient of friction defined for the interface. A non-linear finite element solver (LS-Dyna [11]) was used to perform the transient shock analysis (Chapter 2). The effect of non-operational shock was studied for a typical load/unload disk drive with the suspension parked on the L/UL ramp.

3.3 Dimple Separation and Lift-Tab Separation

Dimple separation is defined as the maximum distance between the suspension dimple and the head gimbal assembly (HGA) after a shock (Figure 3.2(a)), while lift-tab separation is defined as the maximum distance between the suspension lift-tab and the ramp after a shock (Figure 3.2(b)).

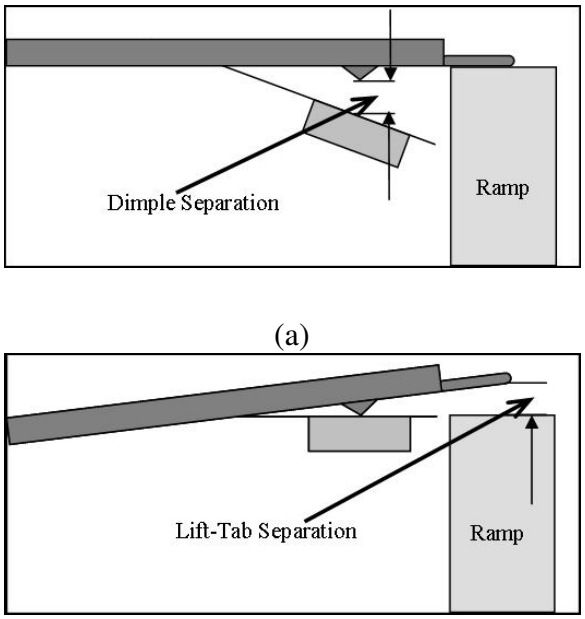

Figure 3.2: (a) Schematic of dimple separation and (b) schematic of lift-tab separation

Figure 3.3 shows different positions of the suspension for a shock load of 800 G and a pulse width of 1 ms as a function of time during a half-sine non-operational shock. Figure 3.3(a) shows the initial position when the suspension lift-tab rests on the ramp, while Figure3.3(b), 3.3(c) and 3.3(d) show the position at time t = 0.690 ms, t = 1.47 ms, and t = 2.20 ms, respectively. From Figure 3.3(b) (time, t = 0.690 ms), we observe that the head gimbal assembly (HGA) has separated from the suspension dimple and moves downward. This motion continues until the limiter stops the downward motion. At this point, the HGA swings back and again contacts the suspension dimple, causing the suspension to move in the upward direction. The upward momentum of the slider causes the suspension lift-tab to separate from the ramp as shown in Figure 3.3(c.).

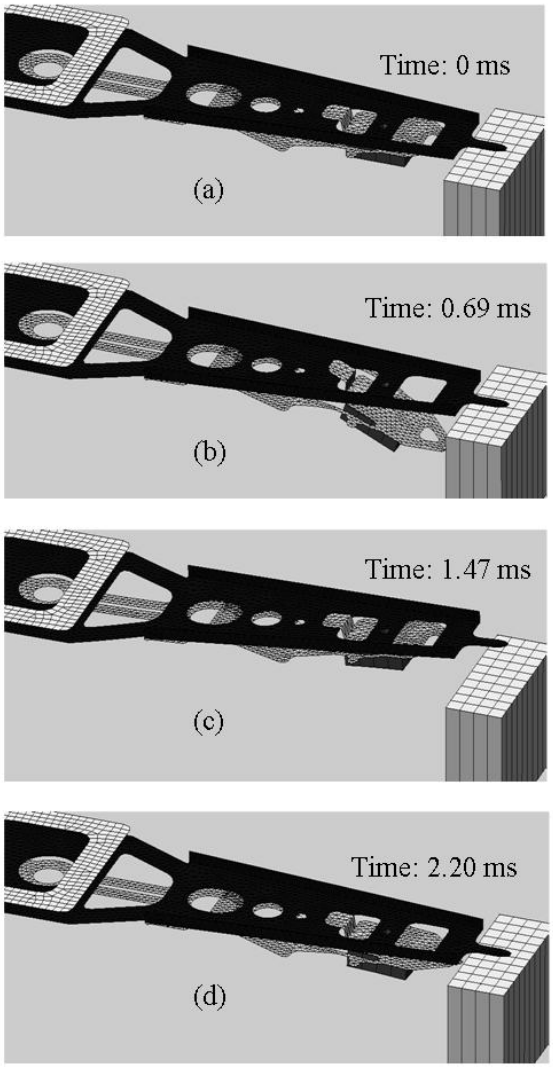

Figure 3.3: Different stages during non-operational shock simulation in a typical load/unload type suspension model: (a) initial position, (b) dimple separation, (c) lift-tab separation, and (d) return to initial position

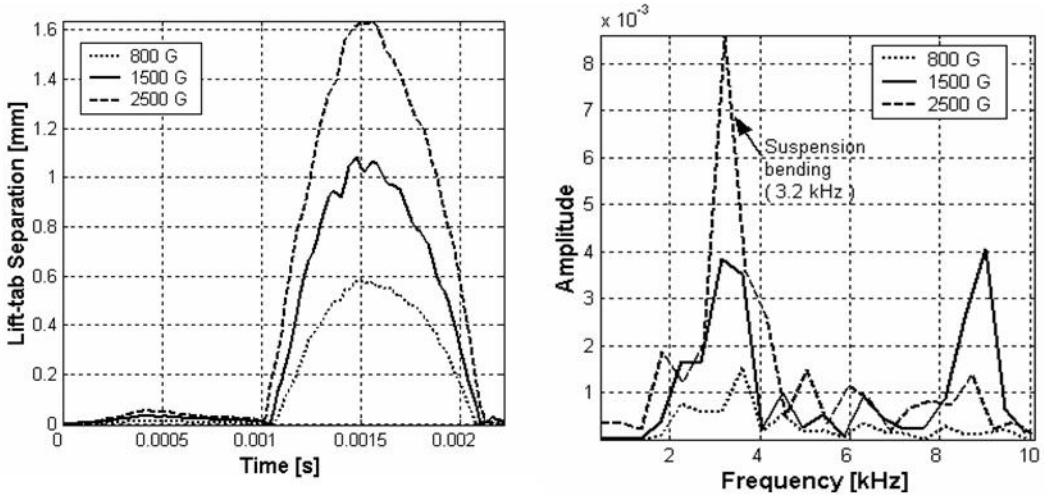

Figure 3.4: (a) Suspension lift-tab separation for different shock amplitudes and 1ms shock pulse width, (b) FFT of lift-tab separation

The time at which the maximum lift-tab separation occurs is 1.470 ms after the initial shock is applied. Maximum lift-tab separation occurs after the half-sine acceleration shock impulse is completed. The suspension then moves downward to rest on the ramp as shown in Figure 3.3(d.). This sequence repeats multiple times but the amplitude of vibrations dampens out quickly after the end of the half-sine acceleration input.

3.4 Numerical Results

3.4.1 Effect of Shock Amplitude on Lift-Tab and Dimple Separation

Figure 3.4(a) shows the separation of the lift-tab versus time for shock amplitudes of 800 G, 1500 G, and 2500 G. To study the frequency content of the HGA due to a

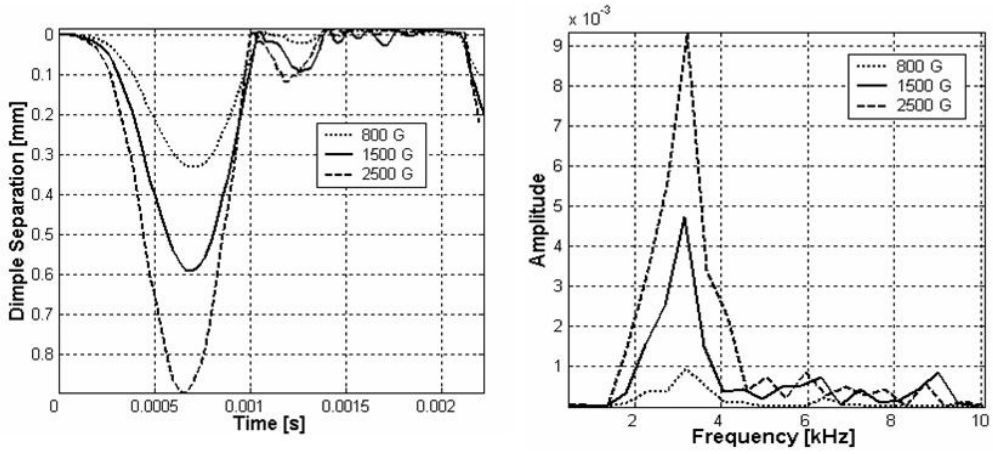

Figure 3.5: (a) Suspension dimple separation for different shock amplitudes and 1ms shock pulse width, (b) FFT of dimple separation

shock, Fast Fourier Transform (FFT) of the displacement signal was performed. 3.4(b) shows the corresponding FFT of lift-tab separation. The pulse width of the half-sine shock input was 1ms in all cases. We observe that the amplitude separation of the lift-tab from the ramp is proportional to the amplitude of the shock. Figure 3.5(a) shows the separation of the dimple from the HGA for shock loads of 800 G, 1500 G, and 2500 G, respectively, and Figure 3.5(b) shows the corresponding FFT of dimple separation. The displacement in Figure 3.5(a) is shown in a downward direction to indicate the distance the HGA moves downward and away from the dimple.

Figure 3.4(a) and Figure 3.5(a) show that the maximum lift-tab separation and the corresponding dimple separation increase with increasing shock amplitudes. Approximately one millisecond after the shock, the HGA separates from the suspension dimple although the suspension lift-tab continues to rest on the ramp. The limiter engages with

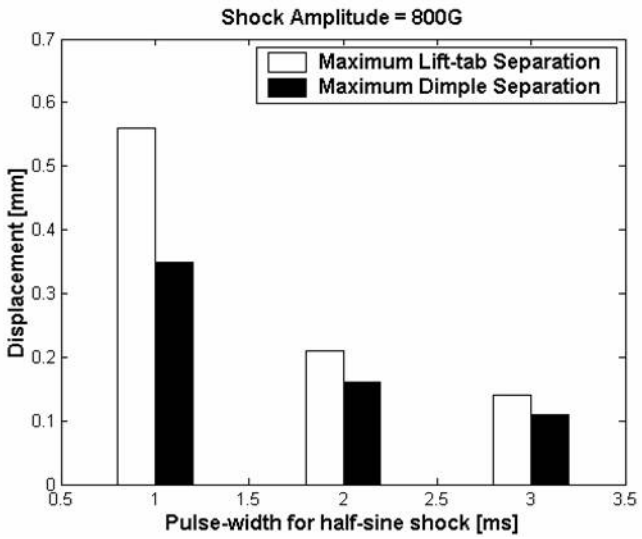

Figure 3.6: Maximum lift-tab and maximum dimple separation for different shock pulse widths of 800G amplitude

the suspension to limit the head separation, causing the HGA to swing back towards the suspension. The contact of the HGA with the suspension dimple causes the separation of the lift-tab from the ramp. . The predominant frequency peak was found to be the first bending mode of the suspension, (3.2 kHz). Thus, the first bending mode of the suspension determines the separation of the lift-tab in the vertical direction. The amplitude of the frequency peak at 3.2 kHz increases with increasing shock amplitude as observed in Figure 3.4(b) and Figure 3.5(b). As can be seen from Figures 3.4 and 3.5, the greater the dimple separation, the greater is the lift-tab separation from the ramp.

3.4.2 Effect of Shock Pulse Width on Lift-Tab and Dimple Separation

To study the effect of shock pulse width on the frequency of excitation, the shock pulse width was varied while keeping the amplitude of the shock constant. Figure 3.6 shows the suspension lift-tab and dimple separation for shock pulse durations of 1 ms, 2 ms, and 3 ms, respectively. In each of the three cases, the amplitude of the shock was 800 G's.

We observe that both the lift-tab and the dimple separation decrease as the pulse width of the half-sine shock input increases. Impact on hard surfaces like concrete or steel causes high amplitude accelerations with shorter pulse widths, while impact on soft surfaces like rubber or carpet produces low amplitude acceleration with longer pulse widths. Figure 3.7 and Figure 3.8 show the maximum lift-tab and maximum dimple separation for the case when the amplitude of the shock is 1500G and 2500G, respectively.

In Figure 3.9, the onset of lift-tab separation as a function of the shock amplitude and the shock pulse width are shown. We observe that the onset of lift-tab separation is a function of the pulse width of the shock input. The lift-tab begins to separate from the ramp after the completion of the half-sine shock pulse even if the amplitude of the shock is kept constant. On the other hand, if the shock amplitude is varied keeping the shock pulse width constant, we observe that the onset of the lift-tab separation is constant for all cases.

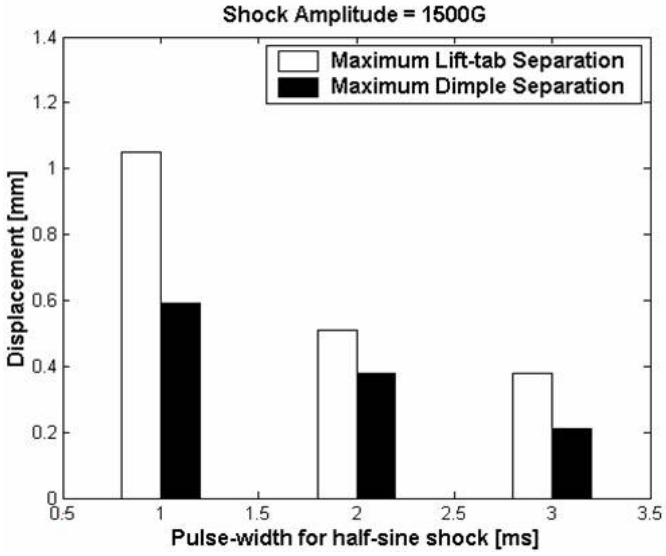

Figure 3.7: Maximum lift-tab and maximum dimple separation for different shock pulse widths of 1500G amplitude

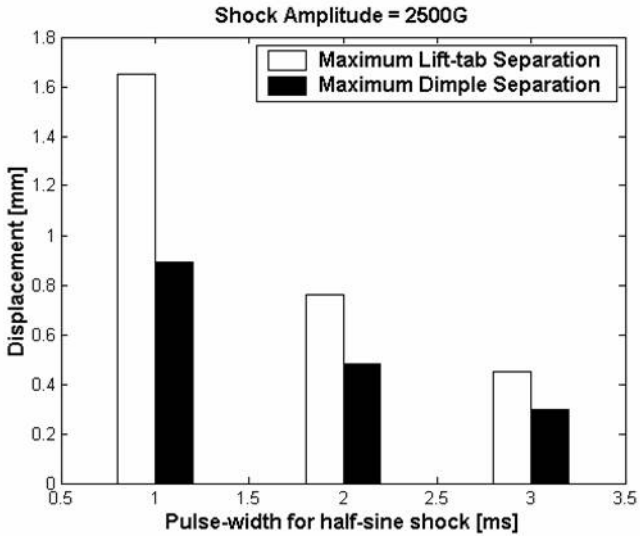

Figure 3.8: Maximum lift-tab and maximum dimple separation for different shock pulse widths of 2500G amplitude

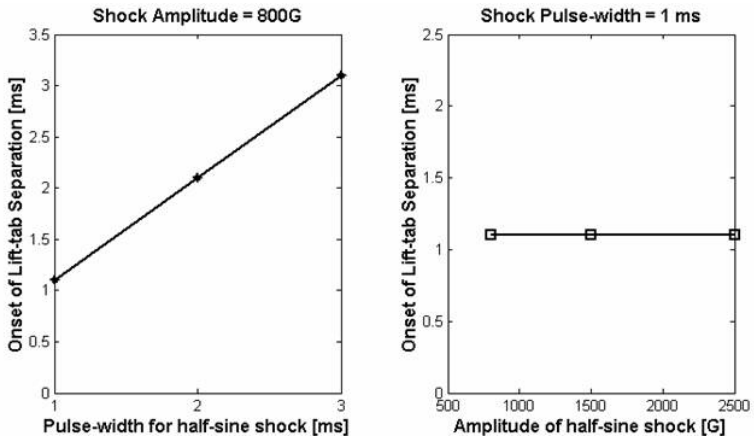

Figure 3.9: Onset of lift-tab separation for varying shock pulse widths (left) and for varying shock amplitude (right)

3.4.3 Effect of Design Parameters on Lift-Tab Separation and Dimple Separation

To study the effect of design parameters on lift-tab separation and dimple separation, a sensitivity analysis for the suspension and gimbal was performed by changing the thickness of the suspension and the gimbal. The shock amplitude was kept constant at 800 G and the pulse width was 1 ms for all cases. In each case, an increase in the thickness of the suspension or the gimbal spring resulted in a higher bending stiffness. An increase in the thickness of the flexure (gimbal) resulted in a reduction of the dimple separation and also a reduction in the lift-tab separation. Reduced dimple separation and lift-tab separation were obtained when the thickness of both the suspension and the gimbal were increased simultaneously.

Figure 3.10 shows the comparison of maximum lift-tab separation and maximum

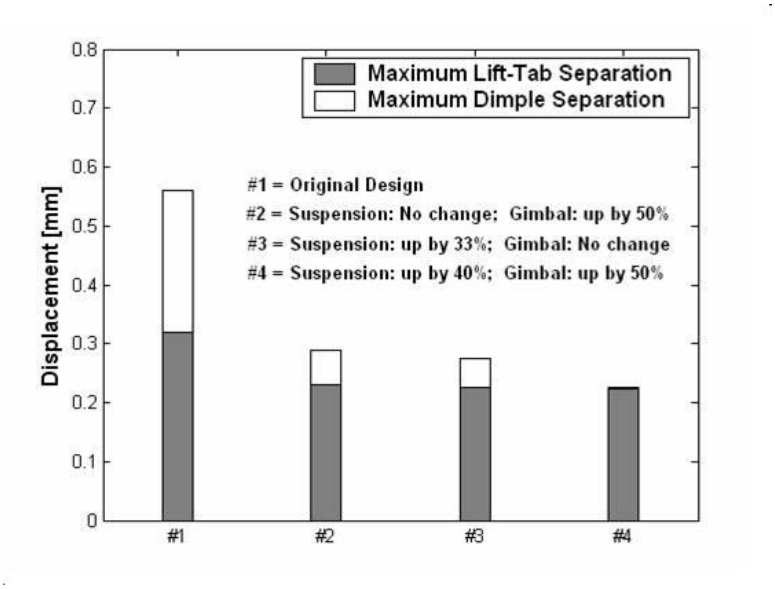

Figure 3.10: Maximum lift-tab separation and maximum dimple separation for different thickness of suspension-gimbal designs

dimple separation for the original suspension-gimbal design and three modified suspension and gimbal designs. From Figure 3.10 we observe that the maximum lift-tab separation and the maximum dimple separation decrease when the thickness of the gimbal is increased by 50% over that of the original design. Comparing the various designs, we see that similar results for maximum lift-tab separation and maximum dimple separation can be obtained by increasing either the suspension thickness or by increasing the gimbal thickness. This can be explained as follows. An increase in the gimbal thickness causes a reduction in the deflection of the HGA due to the increased bending stiffness. Therefore, the momentum of the "swing back" to reestablish contact with the suspension dimple is reduced, resulting in reduced lift-tab separation. Similarly, an increase

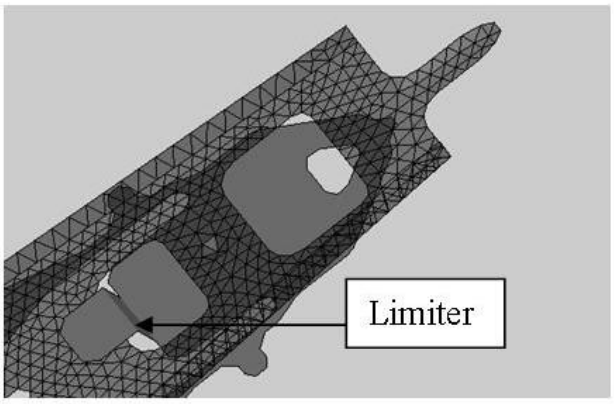

Figure 3.11: Limiter design

in the suspension thickness decreases the suspension deflection due to higher bending stiffness, thereby reducing the dimple and also the lift-tab separation.

3.4.4 Effect of Suspension Limiters and Stress Induced due to Shock

In many load/unload HDD's, a so-called "suspension limiter" is used to restrict the downward movement of the HGA during dimple separation. To investigate the operation and stress induced when a suspension limiter engages, we have studied the performance of a typical limiter design (Figure 3.11).

As can be seen from Figure 3.11, the limiter acts like a hook which contacts the upper surface of the suspension if a large dimple separation occurs. This limits the allowable value of the dimple separation.

As is shown in Figure 3.12, the maximum von Mises stress occurs at the bending region of the flexure during dimple separation. For a shock amplitude of 800 G and a

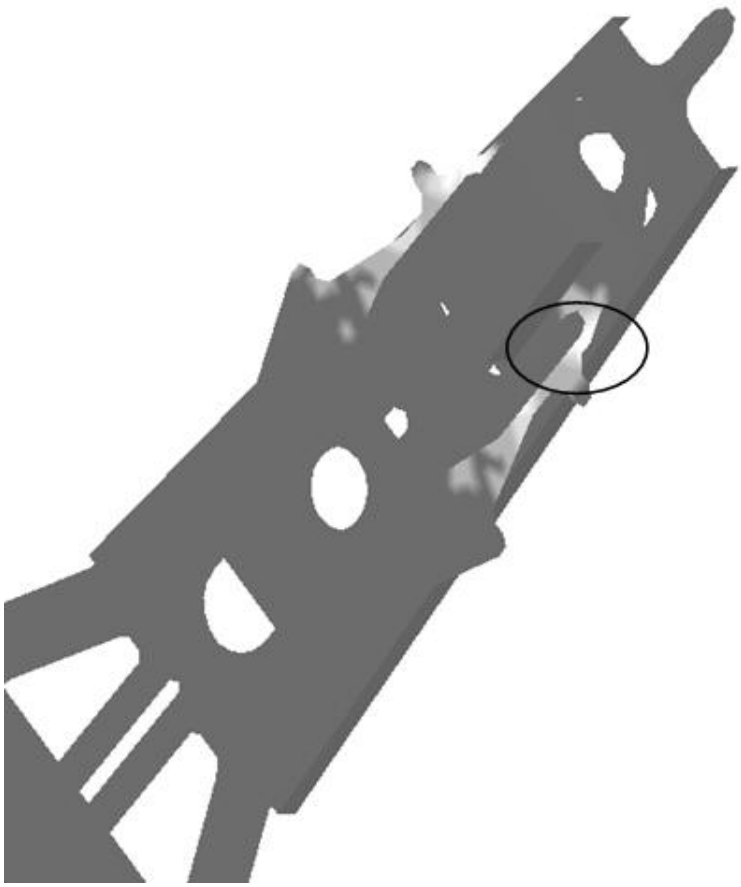

Figure 3.12: Region of flexure where the maximum von Mises stress occurs

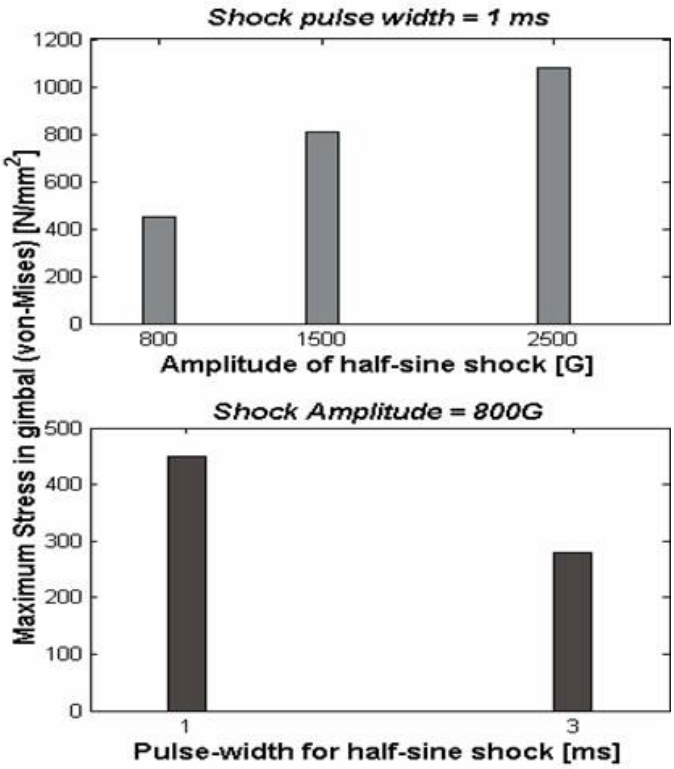

Figure 3.13: Maximum von Mises stress in the flexure for varying shock amplitudes and varying shock pulse widths

shock pulse width of 1 ms, the maximum von Mises stress in the flexure for the limiter design shown in Figure 3.11 was = 450 N/mm2.

The maximum von Mises stress in the flexure is plotted as a function of the shock amplitude and shock pulse width in Figure 3.13. We observe that the stress in the flexure increases with increasing shock amplitude. However, an increase in the shock pulse width reduces the von Mises stress in the flexure. We also observed that for shock amplitudes greater than 2700 G (1 ms half-sine pulse width), plastic yielding occurs at the bending region of the flexure, i.e., the maximum von Mises stress exceeds the yield

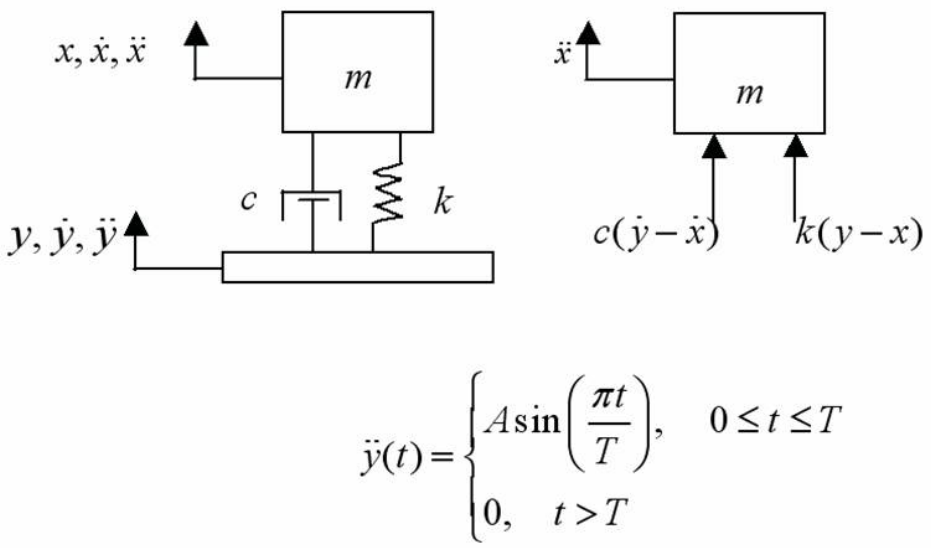

Figure 3.14: SDOF model subject to half-sine input

stress of the material used for the flexure.

3.5 Summary and Discussion

From the numerical results presented, we have observed that dimple and lift-tab separation increase with increasing shock amplitude. On the other hand, both dimple and lift-tab separations were found to decrease with increasing shock pulse width or increasing suspension or gimbal spring thickness. These trends are in agreement with predictions obtained from a damped single degree of freedom (SDOF) model for the suspension shown in Figure 3.14.

For this system, the equation of motion is given by

$$\ddot{z} + 2\xi\omega_n\dot{z} + \omega_n^2 z = -A\sin\left(\frac{\pi t}{T}\right) \qquad (0 \leq t \leq T) \tag{3.1}$$

where z is the relative displacement given by $z = x - y$, c is the damping coefficient, m is the mass, k is the stiffness, while ξ is the damping ratio given by $\xi = c/2m\omega_n$ and ω_n is the natural frequency given by $\omega_n^2 = k/m$.

For the acceleration profile given by

$$\ddot{y}\,(t) = \begin{cases} Asin\left(\dfrac{\pi t}{T}\right) & (0 \leq t \leq T)\,0 \qquad (t > T) \end{cases} \tag{3.2}$$

the displacement is given by

$$y\,(t) = \begin{cases} \dfrac{AT^2}{\pi^2}\left(\dfrac{\pi t}{T} - \sin\dfrac{\pi t}{T}\right) & (0 < t < T) \\ \dfrac{AT^2}{\pi}\left(\dfrac{2t}{T} - 1\right) & (t > T) \end{cases} \tag{3.3}$$

Figure 3.15(a) and Figure 3.15(b) show the relative displacement for the single degree of freedom suspension model as a function of the shock amplitude and shock pulse width, respectively. We observe that an increase in the amplitude of shock increases the relative displacement while an increase in the pulse width causes a reduction in the relative displacement. Furthermore, an increase in flexure thickness results in a reduced relative displacement.

In order to predict the trend of dimple and lift-tab separation on suspension and gimbal thickness, it is convenient to model the suspension as a beam of rectangular cross section. For this case, the equation for the fundamental frequency of a uniform

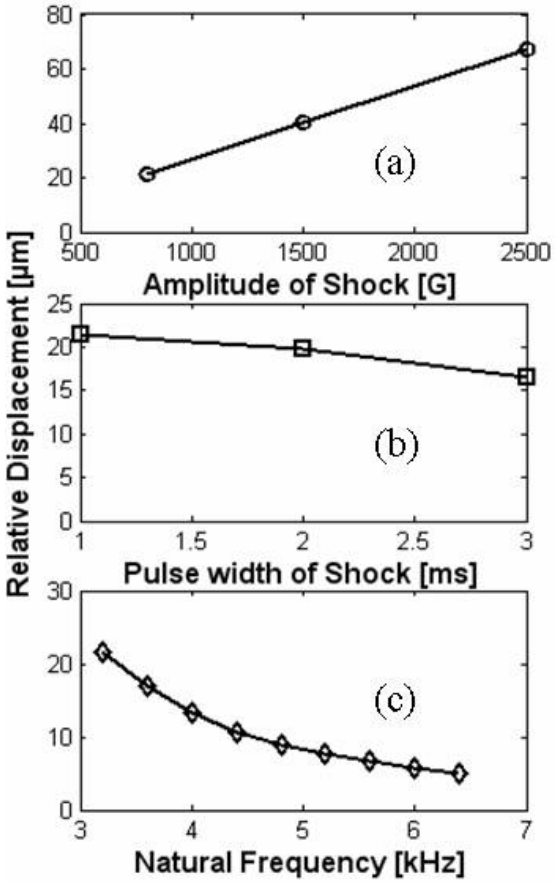

Figure 3.15: Relative Displacement of the SDOF model for suspension

beam is given by

$$f_0 = \kappa\sqrt{\frac{EI}{ml^4}} \tag{3.4}$$

where $I = wt^3/12$ is the area moment of inertia, (w = width of beam, t = thickness of beam) and $m = \rho V = \rho * l * w * t$ (ρ is the density, V is the volume)

$$f_0 \propto t \tag{3.5}$$

Thus, for a simple beam, the fundamental frequency is directly proportional to the thickness of the beam. Figure 3.15(c) shows the relative displacement of the single degree of freedom model as a function of the thickness (a function of the natural frequency). We observe that the trends obtained from the single degree of freedom model for the suspension agree well with the results obtained from finite element analysis. We also note that the relative displacement increases with increasing shock amplitude, decreases with increasing pulse width, and decreases with increasing thickness.

3.6 Conclusions

The following conclusions can be drawn from this study:

Lift-tab and dimple separation increase with increasing shock amplitudes.

Lift-tab separation and dimple separation decrease with increasing shock pulse width.

The pulse width of shock input governs the onset time of lift-tab separation. Shorter

pulse widths excite higher frequencies and greater amplitudes. A short duration shock pulse width causes larger lift-tab separation than a longer duration pulse width for the same shock amplitude.

An increase in the thickness of suspension and gimbal spring causes a reduction in lift-tab separation as well as dimple separation.

The numerical FEM predictions agree well with the trends obtained from a simplified single degree of freedom model for the suspension/gimbal structures.

The maximum von Mises stress in a flexure increases with increasing shock amplitudes. Plastic deformation occurs first in the flexure when the amplitude of shock exceeds the HDD's capability.

Acknowledgement

Part of the material in this chapter has been submitted for publication to the journal *Tribology International*: A. N. Murthy, E. M. Jayson, and F. E. Talke, "Effect of Non-operational Shock on the Suspension Lift-tab and Dimple Separation in a Load/Unload Hard Disk Drive".

The dissertation author was the primary investigator of this paper and was directly supervised by Prof. Frank E. Talke. The co-author Dr. Eric M. Jayson has given his permission to include the material of the paper in this dissertation

Bibliography

[1] Edwards, J.R., “Finite Element Analysis of the Shock Response and Head Slap Behavior of a Hard Disk Drive”, IEEE Transactions on Magnetics, Vol. 35, No. 2 (1999)

[2] Aristegui, J.L., and Geers, T.L., "Shock Analysis of a Disk Drive Assembly", Journal of Information Storage and Processing Systems, Vol. 2, pp. 25-31, (2000)

[3] Jayson, E.M., Murphy, J.M., Smith, P.W., and Talke, "Head Slap Simulation for Linear and Rotary Shock Impulses", Tribology International, 36, 4-6, 311-316 (2003)

[4] Lee, S. J., Hong, S. K. and Lee, J. M., "A study of shock-resistance design of suspension subjected to impulsive excitation," IEEE Trans. on Magn., vol. 37, no. 2, pp. 826-830, 2001.

[5] Lee, H. S, Chang, D. H., Sohn, J. S, Hong, M. P, and Choa, S. H., "Dynamic Absorber for Actuator Arm in A Disk Drive," Asia-Pacific Magnetic Recording Conference, 2000, pp MP13/1 - MP13/2

[6] Zeng, Q.H., Chapin, M, and Bogy, D.B., "Dynamics of the Unload Process for Negative Pressure Sliders", IEEE Trans. on Magn., vol. 35, no. 2, pp. 916-920, 1999.

[7] Zeng, Q.H., Bogy, D.B., "A Simplified 4-DOF Suspension Model for Dynamic Load/Unload Simulation and Its Application", ASME Journal of Tribology, Vol. 122, 274-279, (2000)

[8] Weissner, S., Zander, U., and Talke, F.E., "A New Finite-Element Based Suspension Model Including Displacement Limiters for Load/Unload Simulations", ASME Journal of Tribology, Vol. 125, 162-167, (2003)

[9] Zeng, Q.H., Bogy, D.B., "Effects of Suspension Limiters on the Dynamic Load/Unload Process: Numerical Simulation", IEEE Trans. on Magn., vol. 35, no. 5, pp. 2490-2492, 1999.

[10] Altair Hyperworks, Theory Manual, Altair Computing, Inc.

[11] LS-Dyna, User and Theory manuals, Livermore Software Technology Corp.

[12] Harris C.M., Piersol A.G., Harris" Shock and Vibration Handbook, 5th edition, McGraw-Hill, 2002

4

Experimental and Numerical Investigation of Shock Response in 3.5 and 2.5 inch form factor Hard Disk Drives

4.1 Overview

Hard disk drives encounter shock and vibrations due to impact loads, both during manufacturing and during end use. The effect of mechanical shock is one aspect of the durability of a HDD. Mechanical shock can damage the head disk interface (HDI) leading to permanent failure. It is therefore important to study the response of a HDD

to shock during operational condition in addition to the non-operational condition. A number of investigations have been performed in the past to study the effect of shock in HDD. Allen and Bogy [1] studied the non-operational shock response at the component level for the disk, the suspension and the slider. Edwards [2] performed finite element analysis of an HDD model and compared the numerical results with the experimental results obtained using laser Doppler vibrometry. This study evaluated the shock response of the HDD as a complete system instead of components. Jayson et. al. [3] studied the "head slap" behavior during non-operational conditions for linear and rotary shock inputs. Kouhei et al [4], Ishimaru [5], and Kumar et al [6] have investigated the "head slap" phenomenon experimentally for non-operational shock. Lee et al [7] developed a theoretical model to investigate head slap quantitatively and design a shock resistant suspension by using Hamilton's principle to formulate the equations of motion. Zeng et al [8] and Jayson et al [9] implemented finite element analysis to obtain the structural response of an HDD during operational conditions to shock loads. Zeng et al [8] computed the air bearing stiffness values obtained by solving the steady state Reynolds equation employing a finite difference based numerical scheme. Zeng et al [8] and Jayson et al [9] used to modify the finite element model to obtain the time dependent normal load and moments applied on the slider. Then they determined the dynamic air bearing response to operational shock by solving the time dependent Reynolds equation. Jayson et al [9] used a finite element based solution of the time dependent Reynolds equation. They also studied the effect of air bearing stiffness on a HDD subjected to operational

shock. In a recent investigation, Bhargava and Bogy [1] proposed a procedure to compute the normal loads and moments applied to the slider and determine the air bearing response simultaneously by coupling the two simulation routines for fast computation time. Jayson and Talke [11] also performed slider optimization for operational shock. The time dependent forces and moments were applied as external loads to get the slider response to operational shock as in [9]. The genetic algorithm was then used to optimize the air bearing contour to get optimum results for shock.

In this chapter we investigate the shock response of two form factor hard disk drives. The first is the 3.5 inch HDD, typically used in desktop computers, and the second, a 2.5 inch HDD, typically used in laptop computers. Shock loads and product specifications are different for both types of disk drives. The shock response spectrum (SRS) for linear shock input was obtained during both non-operational and operational states of the drive. The out of plane (z-axis) displacement of the arm and the suspension was measured at different positions using a laser Doppler vibrometer (LDV). The experiments were repeated at least 5 to 10 times at each measurement position to determine the mean and the standard deviation for the maximum peak-to-peak displacement amplitude. A numerical finite element model was developed to simulate the shock response of HDD's. Finite element mesh and loads are applied using a procedure similar to that described in Chapter 2 (Altair Hypermesh [9], LS-Dyna [5]).

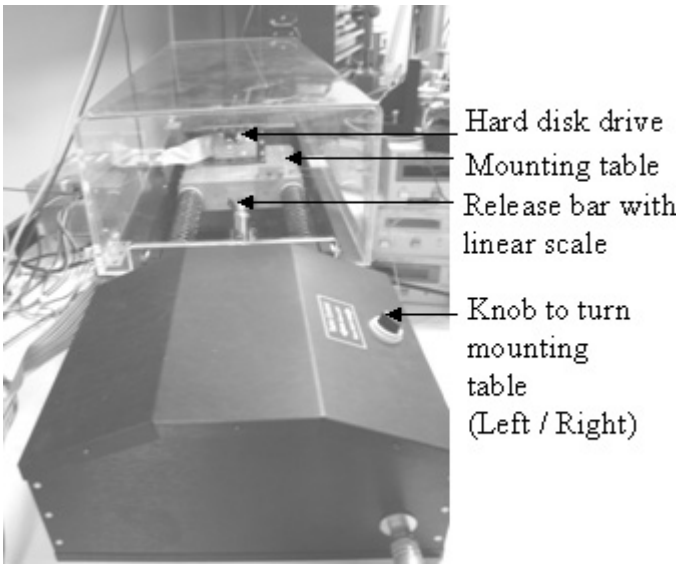

Figure 4.1: Linear shock test machine (GHI Systems Inc.)

4.2 Description of the Experiment

A commercially available linear shock test machine (GHI Systems LSM [12]) was used for the measurement of the shock response in hard disk drives (Figure 4.1). The tester consists of a mounting table (where the HDD is mounted), a seismic mass (to which the mounting table impacts during test), an adjustable linear travel mechanism for the mounting table, and a release mechanism (powered by pneumatic pressure springs).

The tester allows application of half-sine accelerations in the range from 1 G to 10,000 G with pulse widths ranging from 0.1 ms to 30 ms. The amplitude of shock was controlled by varying the distance of travel of the mounting table before impacting the seismic mass. The pulse width of the half-sine shock load can be varied by using different dampers (pre-programmed by elastomeric durometers) to impact the seismic

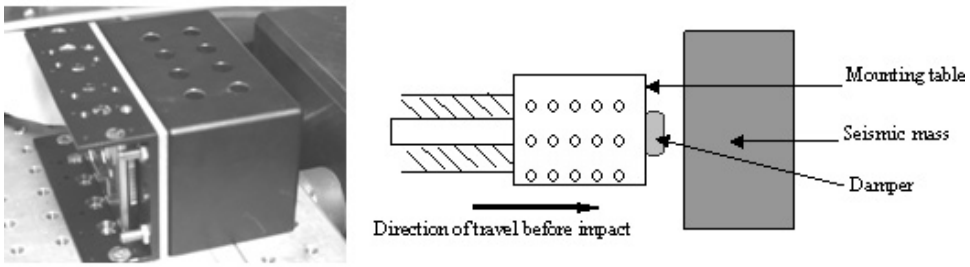

Figure 4.2: HDD mounted on the table and supported by a block (schematic on the right shows seismic mass and damper)

mass. The hard disk drive was mounted onto a C-shaped bracket to secure the drive. The bracket was in turn mounted on the mounting table of the shock machine in a vertical position as shown in Figure 4.2. A rigid block of aluminum was used to minimize the movement of the drive in the horizontal direction due to a linear shock. The cover of the hard disk drive was modified by cutting an opening and covering it with an optically clear glass plate to permit observation of the head suspension assembly (HSA). The window was large enough to permit observation of the HSA during both operational conditions and also during non-operational conditions when the head is parked on a ramp adjacent to the disk.

A Polytec Laser Doppler Vibrometer (1D-LDV) was used to measure the out-of-plane motion of the actuator arm and the suspension at various locations in the disk drive using a transparent mirror mounted on the cover of the drive. A dual fiber interferometer setup was used with the incident beam on the object to be measured and (head or suspension) and the reference beam on the object's carrier (drive body or bracket). This

technique allowed the common mode of the carrier's movement to be removed since the reference beam was dynamically subtracted from the incident beam. A PC was used to control the linear shock machine and another PC was used to control and capture the LDV signal. Post processing of the raw data was performed using Matlab.

4.3 Experimental Results

During non-operational shock, the actuator was "parked" with the suspension lift-tab resting on the L/UL ramp. During operational shock, the disk was spinning and the head was flying over the disk on the outer diameter corresponding to the first data track on the disk. Results for both states of the hard disk drive are discussed in this section.

4.3.1 Results for 3.5 inch HDD

1) Non-operational Shock Response

Figure 4.3(a.), (b.), and (c.) show the experimental data for the displacement of the actuator arm and suspension at three positions denoted by P1, P2, and P3. Position P1 is near the voice coil motor (VCM)), position P2 is near the suspension, and position P3 is in the bending region of the suspension hinge, respectively.

In Figure 4.3, a shock amplitude of 250 G (1 G = acceleration of gravity, 9.81 m/s^2) and a half-sine pulse width of 1 ms was applied. The experiments were repeated at each measurement positions at least ten times. The average of the maximum peak to

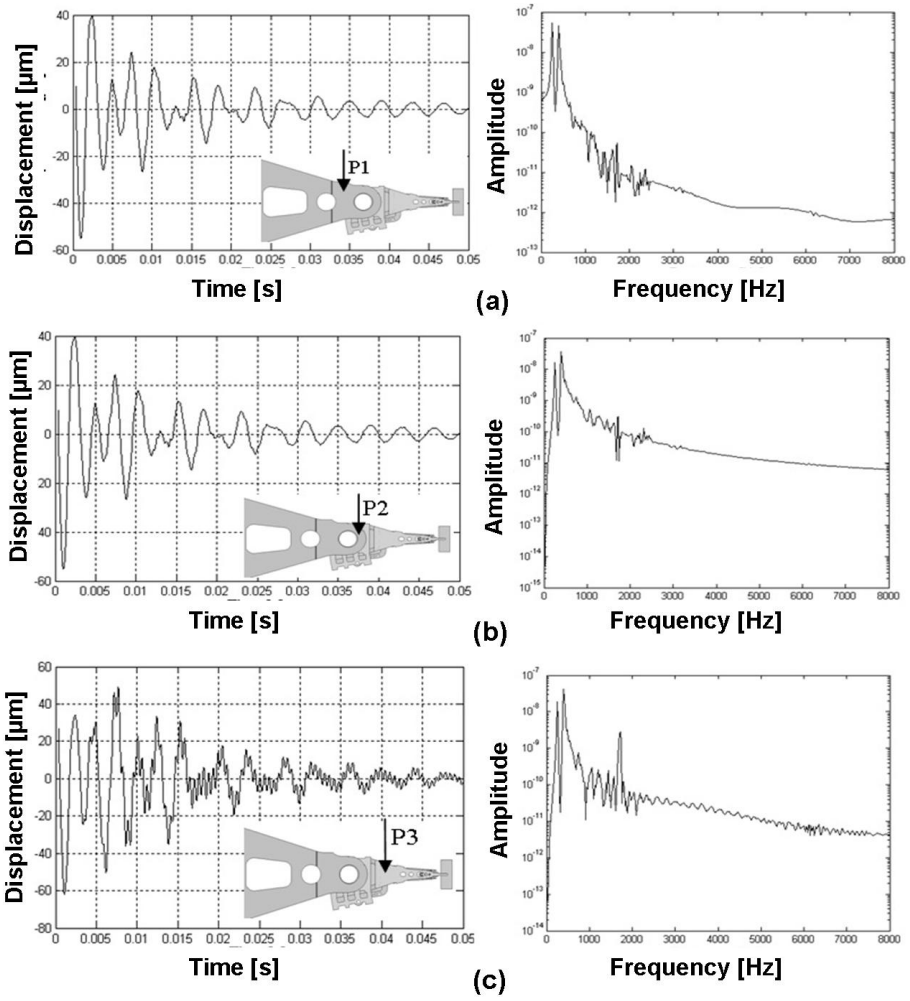

Figure 4.3: Displacement of the actuator arm (a) & (b), and the suspension (c) for non-operational shock in 3.5 inch HDD (FFT of the displacement signal is shown on the right side of each plot)

peak amplitude of displacement was 100 m for the actuator arm and 110 m for the suspension. From the experimental data, we observe that the vibration of the arm and suspension damp out quickly after the shock input. As can be seen from Figure 4.3, the displacement of the arm suspension assembly is dampened out almost completely after 45 ms.

A similar trend in the time-dependent displacement profile was observed for the arm and the suspension. The frequency content of the displacement is shown on the right side of Figure 4.3(a.), Figure 4.3(b.) and Figure 4.3(c.). The first peak at 400 Hz corresponds to the bending mode of the actuator arm and the second peak at 1750 Hz corresponds to the suspension bending mode. No torsional modes of vibration were observed during the experiment. The 400 Hz frequency is a coupled mode which appears on both the arm and suspension displacement signals. The reason for this behavior seems to be the fact that the bending of the suspension includes the effect of bending of the actuator arm. Hence the frequency content of the arm also appears on the FFT of displacement plot for the suspension beam (Figure 4.3(c.)). On the other hand, the suspension bending frequency of 1750 Hz (high frequency vibrations as seen in Figure 4.3(c.)) was not observed in the FFT of the displacement profile for the arm (Figure 4.3(a.) and Figure 4.3(b.)). The reason for this behavior is the fact that the bending of the actuator arm is independent of the bending of the suspension beam. The standard deviation after averaging ten measurements at each position was within 5 % to 10 %.

Figure 4.4 shows the spectrogram of the suspension displacement signal shown in

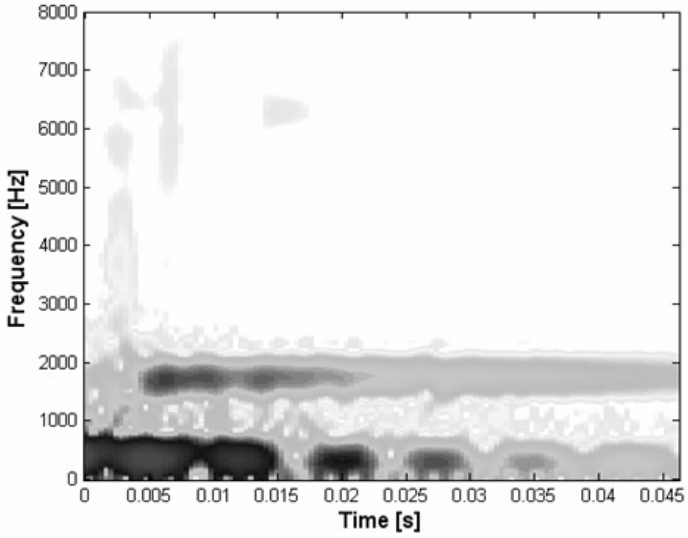

Figure 4.4: Time frequency spectrum of the suspension displacement for non-operational shock in 3.5 inch HDD

Figure 4.3(c.). We observe well defined frequency peaks at 400 Hz and 1750 Hz, respectively, as was observed in Figure 4.3(c). The first band is between 300 Hz to 700 Hz with peak amplitude of 400 Hz corresponding to the arm bending mode. The second band with peak frequency amplitude of 1750 Hz is the suspension bending mode. The amplitude of the mode in the 400 Hz range is higher than the mode at 1750 Hz. A portion of the actuator arm for the 3.5 inch HDD studied was located directly above the outer diameter of the disk during the non-operational state of the disk drive. We therefore measured the z-axis displacement of the disk at the outer diameter which corresponds to a radial position directly below the portion of the actuator arm covering the disk. The average peak-to-peak displacement of the disk at the outer diameter was measured to be

40 m. The clearance between the arm and the disk in the z-axis was approximately 200 m. Even if the disk and the arm displacements were out of phase during the shock, there should be no arm-disk impact due to shock. However, in other disk drives a arm/disk impact could occur if the initial arm/disk clearance is small (less than 200 m).

2) Operational Shock Response

Figure 4.5 shows the displacement of the actuator arm and the suspension at different positions during the operational shock input for the 3.5 inch HDD. Arm position1 (AP1) is the one nearest to the voice coil motor (VCM) and the suspension position2 (SP2) is the farthest from the VCM towards the free end (see inset). In the operational case, the vibrations of the suspension due to shock include contributions from the disk run-out. Since the suspension flies over the spinning disk, any disk run-out caused by the shock load should result in additional vibrations of the head and the suspension.

In Figure 4.5, a shock of 40 G's amplitude and a half-sine pulse of 2 ms was used. The rotational speed of the disk spindle was 15,000 rpm. All measurements in this study were made with the head flying at the outer diameter of the disk. The average of the maximum peak to peak amplitude of displacement for the actuator arm and the suspension was 80 m and 95 m, respectively.

Figure 4.6(a.) shows the out of plane displacement of the suspension for an operational shock of 40 G's, 2 ms input for the 3.5 inch HDD and Figure 4.6(b) shows the spectrogram for the displacement signal. We observe that the frequencies from 300 Hz

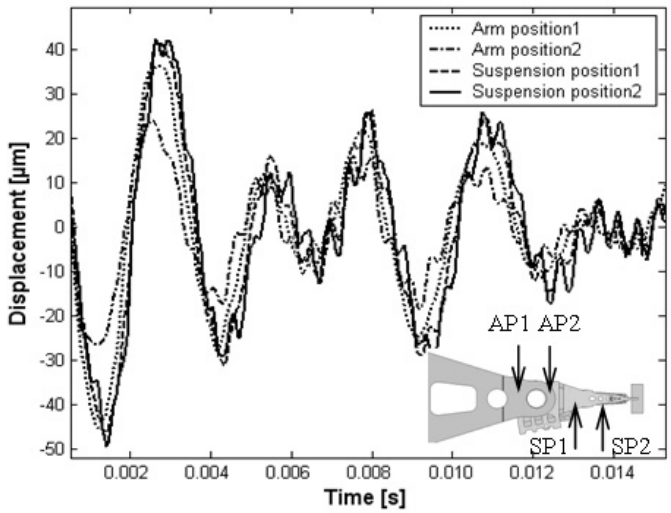

Figure 4.5: Displacement of the actuator arm and the suspension at different positions for operational shock in 3.5 inch HDD

to 600 Hz are identical to the frequencies found in the spectrum shown in Fig.4 for the non-operational shock. On the other hand, a frequency band is observed at 2100 Hz which is slightly higher in amplitude than the one in the non-operational case (1750 Hz). This can also be observed by comparing the FFT signal in Figure 4.6(a.) and Figure 4.3(c.). The overall displacement signal looks similar for the operational shock and non-operational shock even though the specifications are 40 G - 2 ms and 250G - 1 ms, respectively. In the non-operational case, the suspension rests on the ramp and consequently, the disk does not contribute any additional displacement. The non-operational case is similar to a cantilever type loading. However, in the operational case, the suspension flies over the disk with the support of the air bearing which acts as a spring/damper system between the slider and the disk. Thus disk run-out also contributes to the out

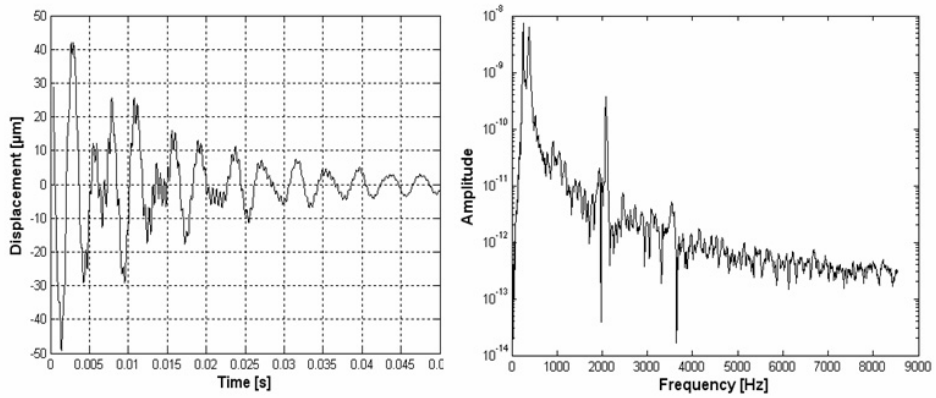

(a)

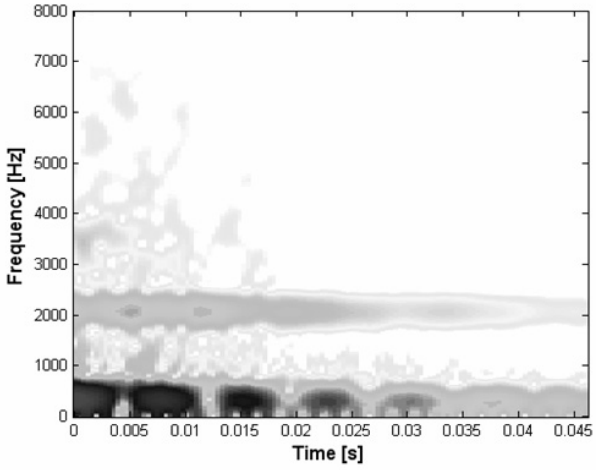

(b)

Figure 4.6: (a) Displacement of the suspension and FFT of displacement and (b) corresponding time-frequency spectrum for operational shock in 3.5 inch HDD

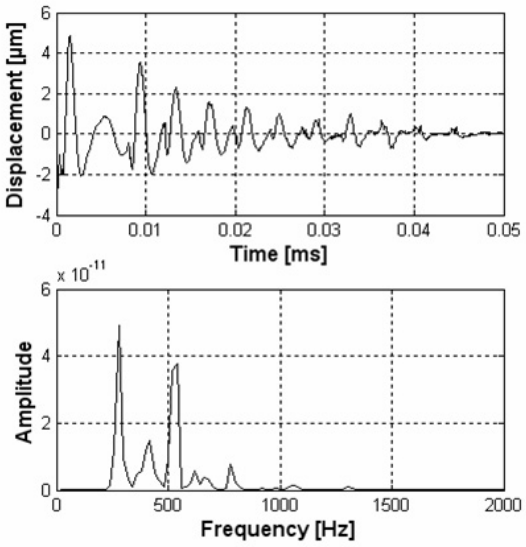

Figure 4.7: Displacement of the top disk at the outer diameter for operational shock in 3.5 inch HDD and corresponding FFT plot

of plane motion of the suspension-arm assembly. The higher frequency for operational shock can also be attributed to the fact that the suspension is supported at both ends.

Figure 4.7 shows the displacement of the disk at the outer diameter and the FFT of the displacement signal. The first and the second umbrella mode of the disk are at 275 Hz and 400 Hz which can be seen in Figure 4.7. The peaks at 550 Hz and 800 Hz are the harmonics of the umbrella modes. The average maximum peak to peak displacement of the disk at the outer diameter was approximately 7 m, i.e., the contribution of disk run-out to HSA vibrations is minimal.

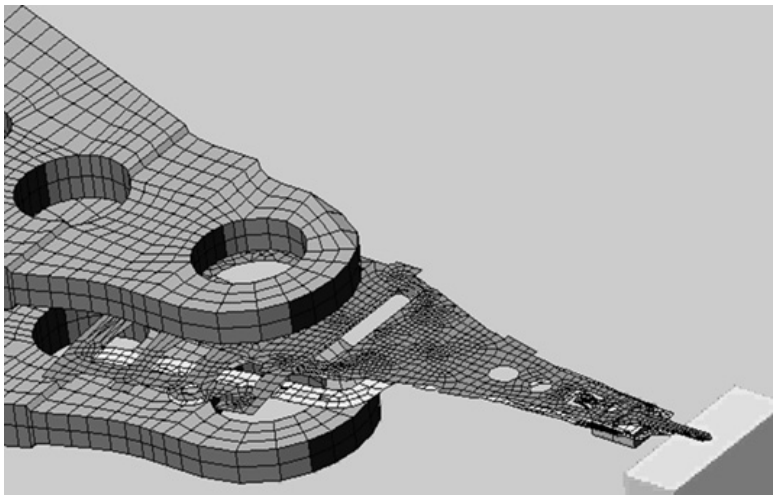

Figure 4.8: Displacement of the top disk at the outer diameter for operational shock in 3.5 inch HDD and corresponding FFT plot

4.4 Numerical Finite Element Model Of The Hard Disk Drive

A finite element model of the hard disk drive was developed using the procedure described in Chapter 2. The simulation computed the acceleration, velocity, and the displacement of each node and also the stress and strain across each element. The displacements of the arm and suspension assembly were computed and compared with experimental results.

Figure 4.8 shows the numerical finite element model of the 3.5 inch HDD. The actuator arm, the ramp and the slider were modeled using solid elements. The suspension, the gimbal and the electrical leads were modeled using shell elements. The model consists of a total of 9904 nodes and 7036 elements. For the non-operational case, the suspen-

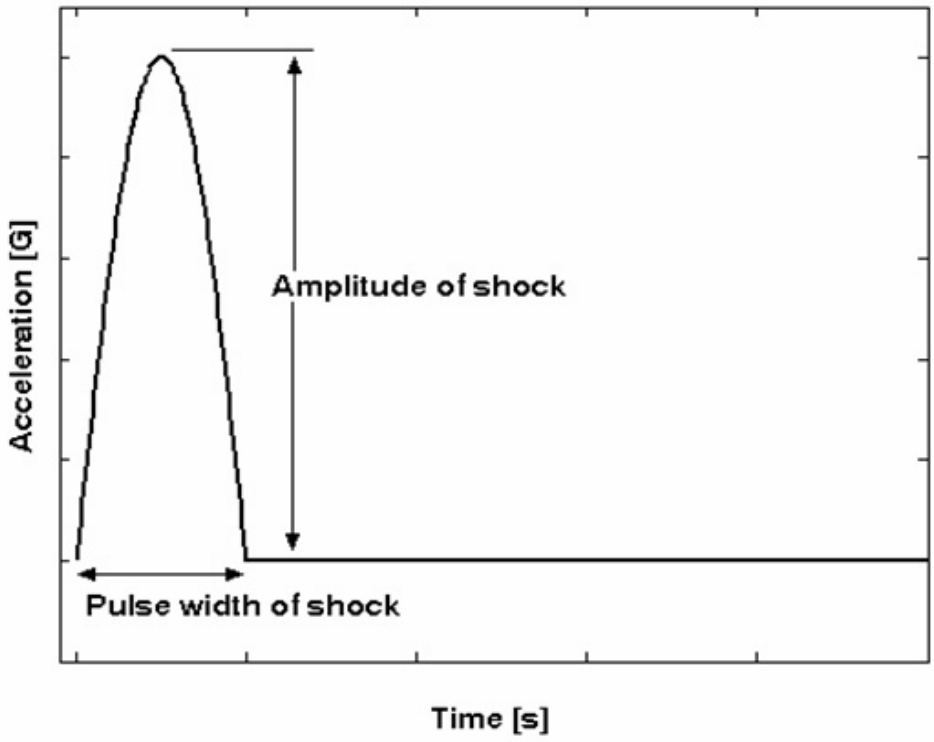

Figure 4.9: Schematic of half-sine acceleration load to simulate shock

sion lift-tab rests on the load/unload ramp. Contact is defined between the suspension lift-tab elements and the top surface of the ramp.

Figure 4.9 shows the schematic of a half-sine acceleration load applied to simulate shock numerically. A half-sine shock load of 250 G and 1 ms pulse width was applied to the HDD model.

Figure 4.10shows the finite element shock simulation results for the 3.5 inch HDD model. The displacement time response of the arm and the suspension was computed at locations corresponding to those of the measured data. The maximum peak-to-peak displacement amplitude predicted by the finite element simulation was within 10% to

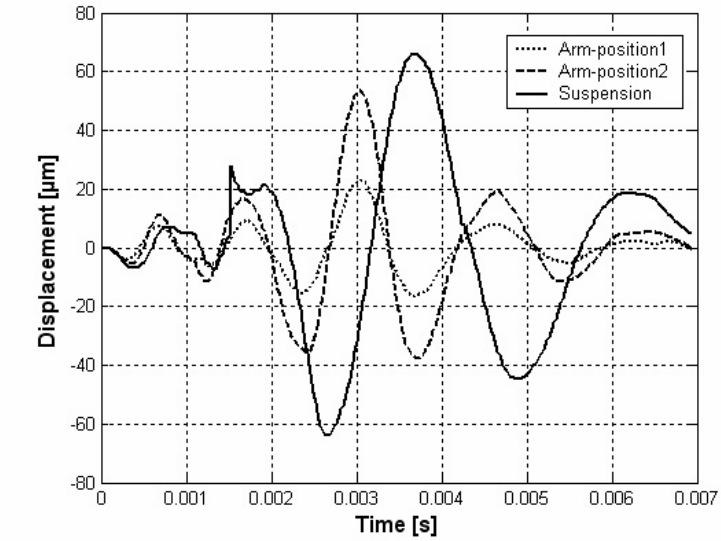

Figure 4.10: Non-operational shock simulation results: displacement of the arm and suspension obtained for the 3.5 inch HDD model Simulation Results for 3.5 inch HDD Model

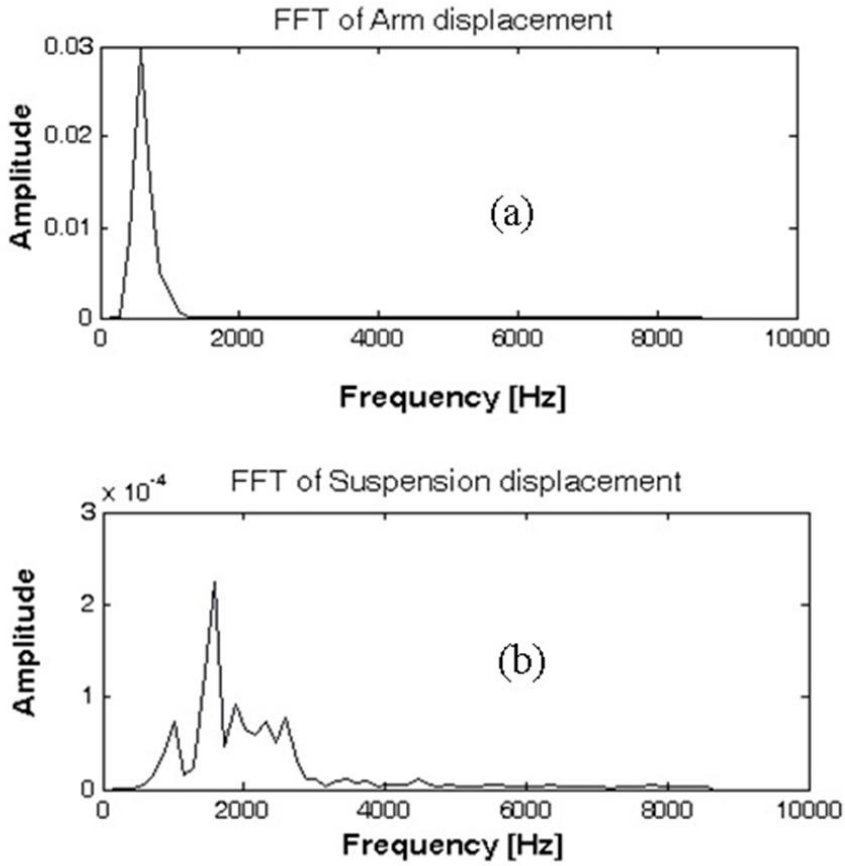

Figure 4.11: (a). FFT of arm and (b) FFT of suspension for non-operational shock simulation in 3.5 inch HDD FE model

experimental results for both the actuator arm and the suspension. The maximum peak to peak displacements for the actuator arm and the suspension were 90 m and 120 m respectively.

Figure 4.11(a.) shows the FFT of the time response for the arm and Figure 4.11(b.) shows the FFT of the time response for the suspension. There is good agreement of the numerical simulation results with the experimental results with respect to the predomi-

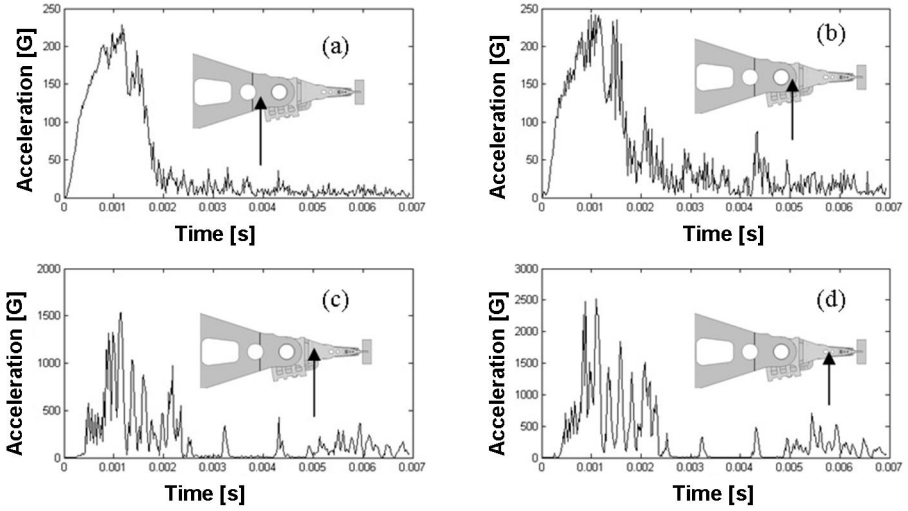

Figure 4.12: Acceleration of arm and suspension at different positions for non-operational shock simulation in 3.5 inch HDD FE model

nant modes of bending.

Figure 4.12shows the acceleration of the actuator arm and suspension at various positions. The acceleration for the actuator arm in Figure 4.12(a.) and Figure 4.12(b.) is similar to that of the half-sine acceleration applied at the base of the actuator arm. However, the stiffness of the suspension is quite different from that of the arm, resulting in vibrations of higher frequency. Figure 4.12(c.) and Figure 4.12(d.) show that the instantaneous acceleration in the suspension could reach values as high as ten times the peak half-sine acceleration input. The acceleration decreases rapidly after the completion of the half-sine shock load in the actuator arm (Figure 4.12(a.) and Figure 4.12(b.)), but it takes longer for the acceleration to dampen out in the suspension (Figure 4.12(c.) and

Figure 4.12(d.)).

4.5 Discussion of Results and Comparison with 2.5 inch HDD

For the prescribed shock inputs, the actuator arm and the suspension predominantly show bending modes of vibrations. Non-operational and operational shock experiments showed that the actuator arm, the suspension, and the disk experience out of plane vibrations due to the linear shock. These vibrations tend to increase in peak-to-peak amplitude from the VCM towards the free end of the suspension. For the specified non-operational shock conditions, we observed that the combined displacements of the actuator arm and the disk did not cause any interference. The specifications for the non-operational and operational shock cases were 250 G, 1 ms and 40 G, 2 ms respectively. However, the difference in the displacement amplitudes for the two cases was slight, if any. The actuator arm suspension system showed peak-to peak z-axis displacement between 80 m and 120m. This means that the HDD can withstand higher amplitude shock loads during non-operational state than during the operational state without any damage to the HDI. The operational shock specification in terms of shock amplitude is 15% to 20% of the non-operational specification for both form factors discussed (250 G for non-operational shock and 40 G for operational shock for 3.5 inch HDD). Hence, the worst case situation is head disk interface failure during operational condition. On the

other hand, the disk is much more robust to shock compared to the head stack assembly. HDI failure mostly occurs due to impact of components of the head stack assembly onto the disk ("head slap" [2], [3]). Components of the head stack assembly in general fail earlier due to shock than the disk. The simulation results show that the von Mises stress in the suspension and flexure approaches the yield strength during a shock event. Suspension design changes and increases in the suspension preload can reduce the head slap phenomena and thereby increase the operational shock specifications. Slider air bearing design and optimization to prevent head slap during operational shock [11] can also improve the shock performance of the HDD. Numerical simulation results for the non-operational case agreed well with the experimental results with respect to the displacement amplitudes and modes of vibrations. The shock response was also measured for the 2.5 inch HDD. The specification for non-operational shock load and operational shock load in the 2.5 inch HDD was 800 G - 1 ms and 100 G - 11 ms respectively.

Typical results of the displacement of the actuator arm and suspension of 2.5 inch HDD for non-operational shock are shown in Figure 4.13. It is evident from Figure 4.13 that the fundamental frequencies of the arm-suspension assembly are higher in the 2.5 inch HDD than in the 3.5 inch HDD. The implications of these results in terms of shock response are that the 2.5 inch HDD is capable of withstanding higher shock loads than the 3.5 inch HDD. This is desirable since the smaller form factor drive is used in a mobile environment and has greater likelihood of experiencing impact loads than the 3.5 inch HDD. Fundamentally, the arm structure and design is different for the

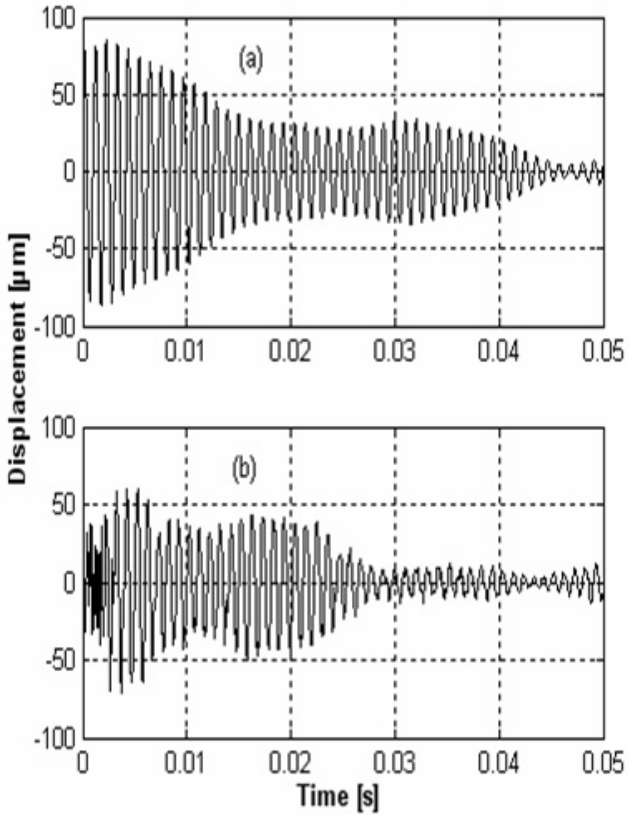

Figure 4.13: (a) Displacement of the arm, (b) the suspension bending region for non-operational shock in 2.5 inch HDD

two HDD's. The larger arm stacking in the 3.5 inch HDD along with the longer beam length and lower bending stiffness produces lower frequency modes. Alternatively, the 2.5 inch HDD has smaller HSA stacking, a less rigid design and smaller beam length, which produce higher frequency modes. Higher bending frequencies for the HSA are desirable for better shock performance.

4.6 Summary and Conclusions

The shock response of a 3.5 inch HDD was experimentally investigated for both the non-operational and the operational case.

We observed that there is no actuator arm - disk impact for the specified non-operational shock load conditions.

Operational shock response showed that the disk contribution to out of plane displacements of the HSA is less than 10% for the specified shock load conditions in the experimental set up.

A numerical finite element model of the 3.5 inch HDD was developed to simulate the shock response for the non-operational case. The results obtained in the simulation compared well with the experimental results. The bending modes of the suspension and arm were also in good agreement with the experimental results.

In comparison, we observed that the vibrations modes of the suspension-arm assembly in the 2.5 inch HDD is higher than the vibration modes of the suspension-arm

assembly in a 3.5 inch HDD.

Acknowledgement

Part of the material in this chapter has been published in the *Microsystem Technologies Journal* : A. N. Murthy, B. Feliss, D. Gillis, and F. E. Talke, "Experimental and Numerical Investigation of Shock Response in 3.5 and 2.5 inch form factor Hard Disk Drives", Microsystem Technologies, Vol.12 (no. 12): 1109-1116, 2006.

The dissertation author was the primary investigator of this paper directly supervised by Prof. Frank E. Talke. The co-authors Dr. Bert Feliss and Dr. Donald Gillis have given their permission to include the material of the paper in this dissertation.

Bibliography

[1] A. M. Allen, and D. B. Bogy, "Effects of shock on the head-disk-interface," *IEEE Trans. on Magn.*, vol. 32, no. 5, pp. 3717-3719, 1996

[2] J. R. Edwards, "Finite element analysis of the shock response and head slap behavior of a hard disk drive," *IEEE Trans. On Magn.*, vol. 35, no. 2, pp. 863-867, 1999

[3] E. M. Jayson, J. M. Murphy, P. W. Smith, and F. E. Talke, "Head slap simulation for linear and rotary shock impulses," *Tribology International*, vol. 36, 4-6, pp. 311-316, 2003

[4] T. Kouhei, T. Yamada, Y. Kuroba, and K. Aruga, "A study of head-disk interface shock resistance," *IEEE Trans. on Magn.*, vol. 31, no. 6, pp. 3006-3008, 1995

[5] N. Ishimaru, "Experimental studies of a head/disk interface subjected to impulsive excitation during non operation," *ASME J. of Tribology*, vol. 118, pp. 807-812, 1996

[6] S. Kumar, V. D. Khanna, and M. Sri-Jayantha, "A study of the head disk interface shock failure mechanism," *IEEE Trans. on Magn.*, vol. 30, no. 6, pp. 4155-4157, 1994

[7] S. J. Lee, S. K. Hong, and J. M. Lee, "A study of shock-resistance design of suspension subjected to impulsive excitation," *IEEE Trans. on Magn.*, vol. 37, no. 2, pp. 826-830, 2001

[8] Q. H. Zeng, and D. B. Bogy, "Numerical simulation of shock response of disk-suspension-slider air bearing systems in hard disk drives," *Microsystem Technologies*, vol. 8, pp. 289-296, 2002

[9] E. M. Jayson, J. M. Murphy, P. W. Smith, and F. E. Talke, "Effects of air bearing stiffness on a hard disk drive subject to shock and vibration," *ASME J. of Tribology*, vol. 125, pp. 343-349, April, 2003

[10] P. Bhargava, and D. B. Bogy, "Numerical Simulation of Operational-Shock in small form factor drives," *ASME J. of Tribology*, 129, 153-160 , 2007

[11] E. M. Jayson, and F. E. Talke, "Optimization of air bearing contours for shock performance of a hard disk drive," *ASME J. of Tribology*, vol. 127, pp. 878-883, October, 2005

[12] GHI Systems, Inc., 2005

[13] Polytec Inc., 2005

[14] Altair Hyperworks, Theory Manual, Altair Computing, Inc., 2006

[15] LS-Dyna, User and Theory manuals, Livermore Software Technology Corp., 2006

5

Numerical Investigation of Shock and Vibration Response in 1-inch Form Factor Hard Disk Drives

5.1 Dynamic Response of 1-inch form factor disk drives to Shock Loads

Commercially available microdrives (1-inch form factor disk drives) were tested using linear shock testing equipment. The shock amplitude for operational and non-operational shock was gradually increased to determine the maximum shock that a microdrive could withstand before failure. During a shock event, the displacement and frequency of the vibrations of the microdrive were examined at various locations on the

arm and suspension. In addition, A scanning laser Doppler vibrometer (LDV) was also used to determine the amplitude and frequency of the vibrations of the front cover and to investigate whether these vibrations contribute to failure of the head/disk interface. A finite element model of the disk drive was also developed to simulate the shock response. The maximum amplitude for failure to occur was determined numerically for operational and non-operational conditions using a pulse width of 2 ms. A comparison of experimental and numerical results was performed.

5.1.1 Overview

The probability of experiencing external shock and vibration loads are higher for small form factor disk drives. These drives are used in consumer products such as music players (iPods), digital cameras, personal digital assistants (PDA's), and cellular phones. Therefore, it is important to understand the shock boundary (amplitude of shock at which the head disk interface fails) and vibration characteristics of small form factor drives.

Several authors have published work on shock in the head disk interface. Bhargava and Bogy [1] proposed a procedure to compute the normal loads and moments applied to the slider and determine the air bearing response simultaneously by coupling the two simulation routines for fast computation time. Jayson and Talke [2] also performed slider optimization for operational shock. The time dependent loads and moments were applied as external loads to predict the slider response to operational shock as in [3].

The genetic algorithm was then used to optimize the air bearing contour for shock [2]. In the previous chapter [4], the operational and non-operational shock response of 3.5 and 2.5 inch hard disk drives was described. The displacement of the actuator arm, the suspension, and the disk due to linear shock was studied both experimentally and numerically.

In this chapter, we investigate the shock and vibration response of small form factor (1 inch disk diameter) hard disk drives or "microdrives". A number of microdrives were used to determine the operational and non-operational shock response using the same shock testing equipment as used in Chapter 4. In this study, three types of microdrives were tested; Vendor #1 with 4 GB (Gigabytes) and 6 GB drives and Vendor #2 with a 5 GB drive. An analysis and comparison was made between all three types of drives to determine the maximum shock parameters needed to sustain hard and soft errors. The response to linear shock input was studied for both non-operational and operational states of the drive. The out-of-plane (z-axis) displacement of the arm and suspension was investigated at different positions. In addition to the experimental data collected, a numerical finite element model was developed to simulate shock in a microdrive.

5.1.2 Experimental Results

Microdrives from two different vendors were first subjected to operational shock while the heads performed random read/write motion between the inner diameter (ID) and outer diameter (OD) of the disk. Shock testing under fast access conditions is done

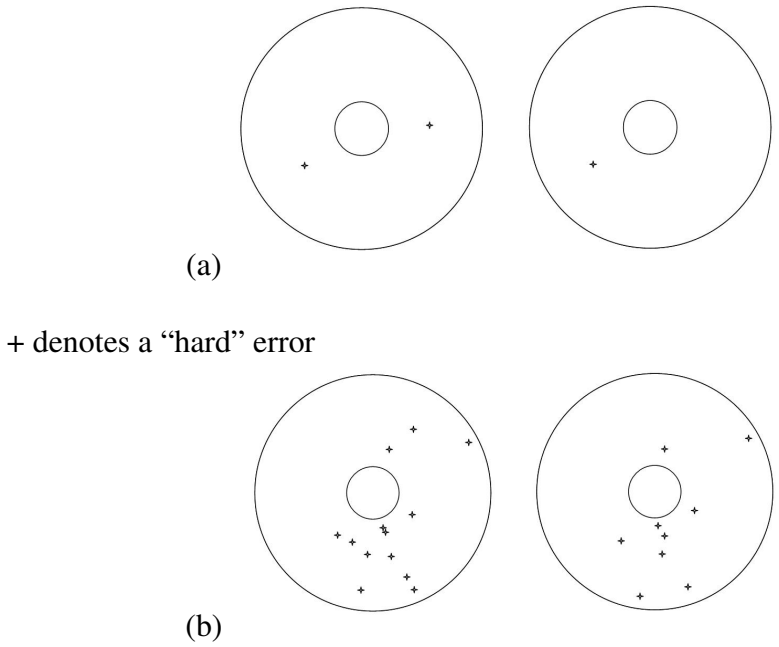

Figure 5.1: (a) Hard errors after 200 G - 2 ms shock during dwell (both surfaces of a single disk), (b) Hard errors after 200 G - 2 ms shock during fast access (both surfaces of a single disk)

for the following two reasons: 1) to simulate “real life” events during which the drive will be subjected to shocks, i.e. running, walking, or jogging; and 2) to study the shock response of the drive while it is accessing different tracks. During fast access, the flying height of the head decreases due to roll motion of the head. A shock event can impose severe stress on the head/disk interface during roll motion since the flying height is decreased.

A typical shock event during track following (dwell) and fast accessing is shown in Figure 5.1(a) and Figure 5.1(b), respectively. The shock event during dwell produces only 1 hard error at the location of the dwell track. The shock event during fast access

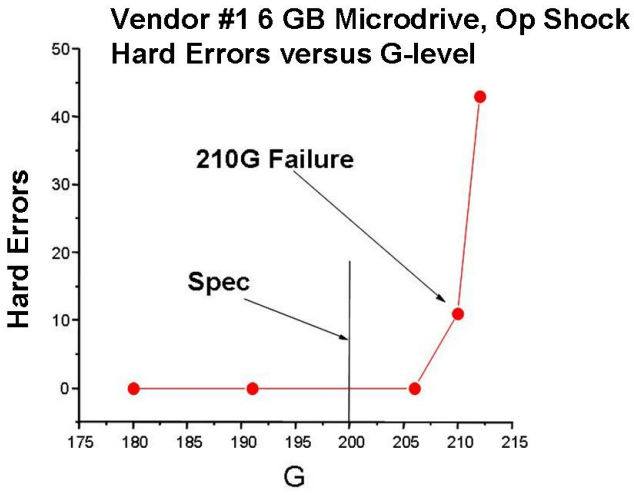

Figure 5.2: Number of Hard Errors vs. G, Vendor #1 (operational shock)

produces over a dozen hard errors between ID and OD, which is more than ten times worse than the dwell condition. During the time that both heads are accessing across the surface of the disk, the shock event occurs over a 2 ms time. The heads hit the disk; bounce many times while the actuator is pulling the heads across the entire surface, from ID through OD. Multiple hard errors are created across both disk surfaces.

For the operational shock, the shock intensity in the z-direction was monotonically increased from 0 to 250 G while monitoring the number of hard/soft errors that incurred for each shock level. The shock pulse width was 2 ms for all operational shock experiments.

The results of the first linear shock test for Vendor #1 microdrive is shown in Figure

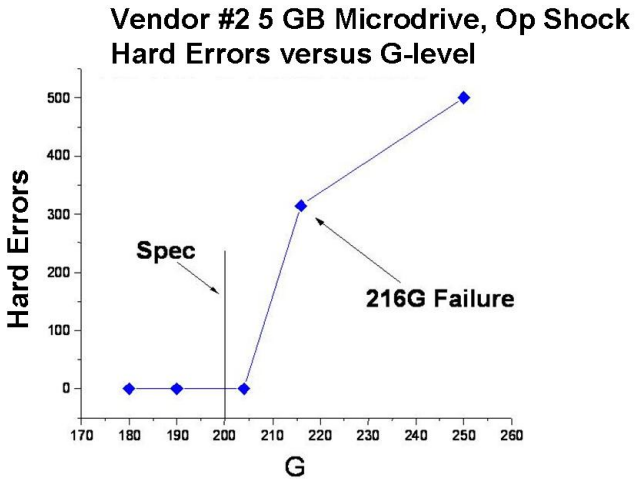

Figure 5.3: Number of Hard Errors vs. G, Vendor #2 (operational shock)

5.2. The specification for all microdrives tested was 200 G operational in the z-direction. The microdrive tested passed this specification and went on to log hard errors at 210 G, which was termed a failure. The microdrive from Vendor #2 was tested in the same fashion and the results are shown in Figure 5.3. This microdrive passed the 200 G specification and then failed at 216 G. Both microdrives tested successfully for the operational shock specification.

For the non-operational shock, the shock amplitude in the z-direction was increased from 0 to 2800 G while monitoring the readiness of the HDD after each shock level. The specification for both drives is 2000 G. The shock pulse width was 1 ms for all non-operational shock experiments. The non-operational shock parameter (increasing

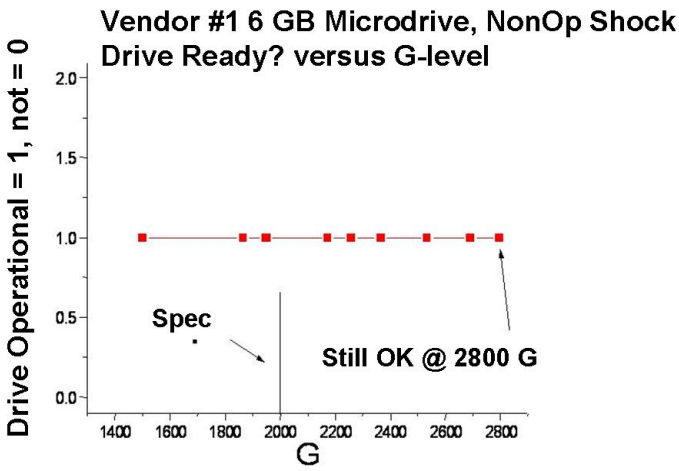

Figure 5.4: Number of Hard Errors vs. G, Vendor #1 (non-operational shock)

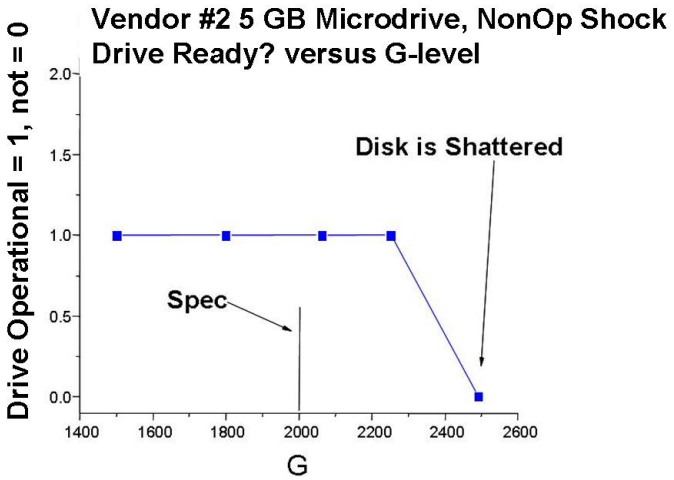

Figure 5.5: Number of Hard Errors vs. G, Vendor #2 (non-operational shock)

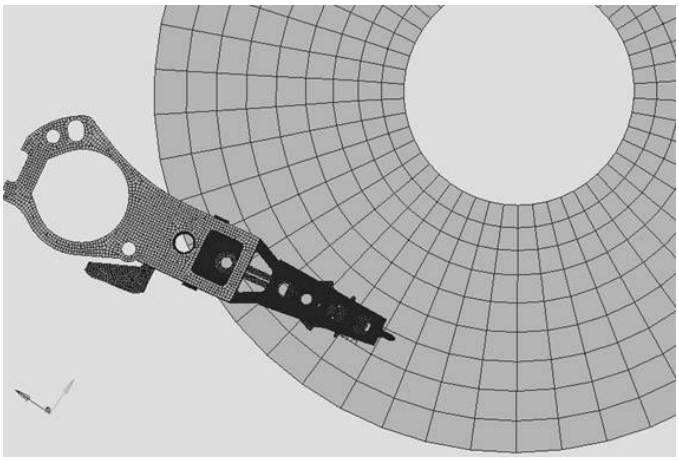

Figure 5.6: . Finite element model of the microdrive

the amplitude of G) was tested against both microdrives and the results are shown in Figures 5.4 and 5.5.

The non-operational shock testing of the microdrive for Vendor #1 was shown to be very robust since it surpassed the specification of 2000 G by 800 G. The experiment was truncated at 2800 G due to limitations of the shock apparatus. The microdrive for Vendor #2 also surpassed the 2000 G specification but increasing it to 2500 G caused the disk to shatter. The disk failure was due to shock failure of other components in the drive that impacted the disk during the shock event. The second part of the experiment, involving the measurement of the out-of-plane (z-axis) displacement of the arm and the suspension, will be discussed as a comparative analysis in the following section.

5.1.3 Numerical Shock Simulation and Comparison to Experimental Results

The finite element model of the disk drive is shown in Figure 5.6. The shock specifications for the microdrive were used in the numerical model for the non-operational and operational conditions. Shock loads were modeled as half-sine acceleration impulses. The shock loads were applied to the base of the disk drive for the shock simulation. A commercially available finite element program [9] was used as pre and post-processor in the simulation study. Two different finite element models were developed for numerical analysis. One model was for a non-operational shock simulation and the other for an operational shock simulation. For non-operational shock simulation, the head stack assembly is parked on a load/unload (L/UL) ramp. For the operational shock simulation, the head stack assembly is supported over the disk by springs that represent an air bearing as in [3].

The transient analysis of the drive response to a shock was performed using a nonlinear finite element solver (LS-Dyna [5]). Contact is defined between the various components such as the suspension, gimbal, ramp, slider and disk to avoid interference. The simulation computed the acceleration, the velocity, and the displacement of each node and also the stress and strain for each element. The displacement of the arm and suspension assembly was computed and compared with experimental results.

Figure 5.7 shows the displacement of the suspension for an operational shock. Figure 5.7(a) is the measured data and Figure 5.7(b) is the simulation result. In Figure

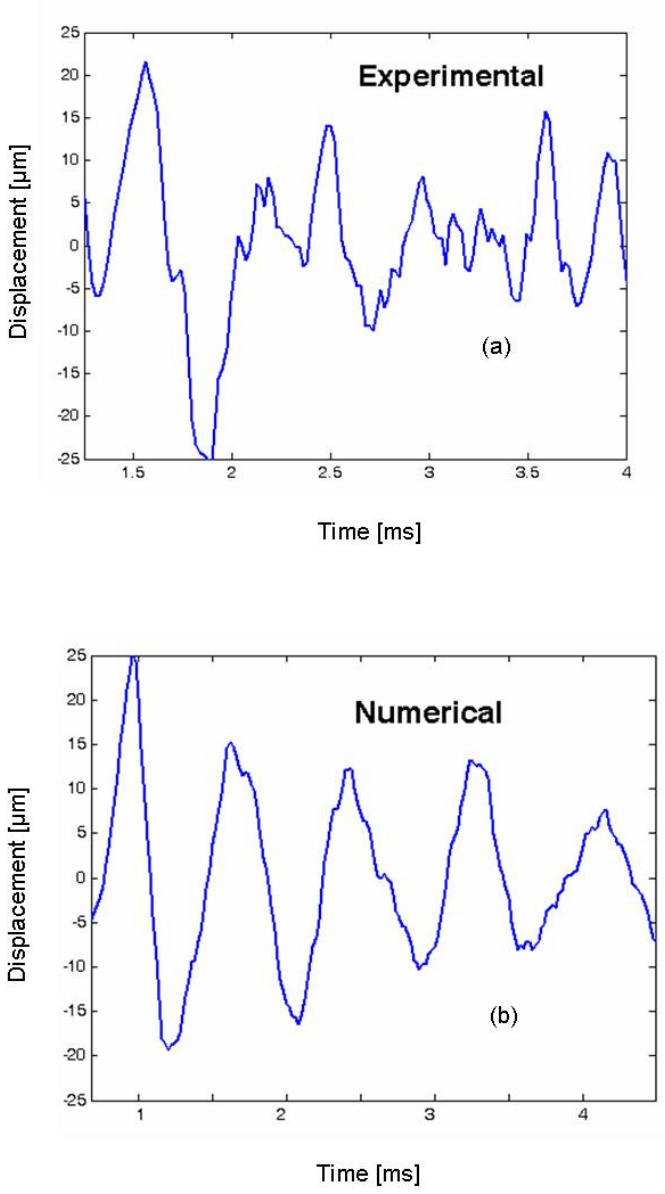

Figure 5.7: Displacement of suspension for operational shock: (a) Experimental, (b) Numerical

5.7 an acceleration of 210 G and a pulse width of 2 ms duration were used for both the experimental and numerical results. We observe that the maximum peak-to-peak displacement from the numerical simulation is close to the experimental results.

Figure 5.8(a) shows the Fast Fourier Transform (FFT) of the measured displacement signal for operational shock shown in Figure 5.7(a). Figure 5.8(b) shows the spectrogram of the numerical displacement signal for operational shock shown in Figure 5.7(b). From Figure 5.8, we observe mostly the first bending modes of the arm and the suspension. From the FFT plot of the measured data, we see that the dominant resonant frequencies are between 500 Hz to 3800 Hz with the maximum amplitude occurring at around 950 Hz. This is also seen on the spectrogram (Figure 5.8(b)) of the shock simulation data suggesting good correlation of the experimental and numerical results in the frequency domain. The displacement time response of the arm and the suspension was computed at locations similar to those where the data were measured. A comparative analysis was made for both the non-operational and the operational shock data.

Figure 5.9 shows the maximum peak-to-peak displacement of the arm and suspension for non-operational shock. The experimental results for the maximum peak-to-peak displacement of the arm and the suspension are compared with the numerical results. The amplitude of the displacement for the arm and the suspension is between 30 m and 50 m.

Figure 5.10 shows the maximum peak-to-peak displacement of the arm and suspension for operational shock. A comparison of experimental and numerical results for

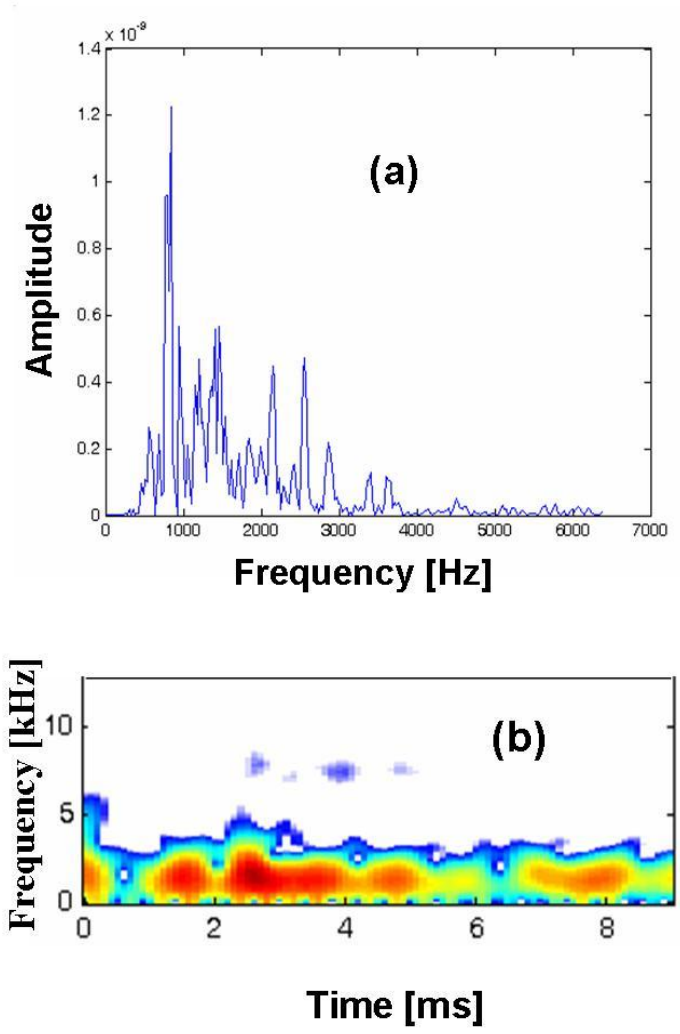

Figure 5.8: (a) FFT of displacement shown in Figure 5.7(a), (b) spectrogram of displacement shown in Figure 5.7(b))

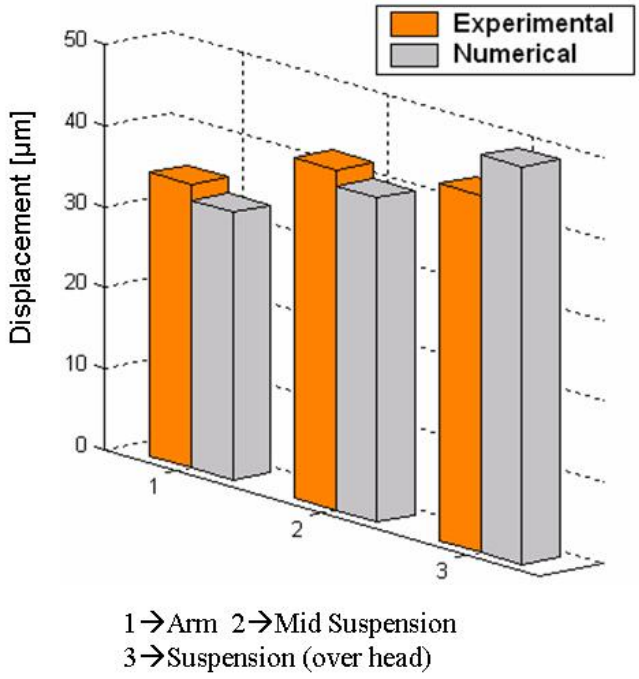

Figure 5.9: Maximum peak-to-peak displacement at different locations (non-operational shock)

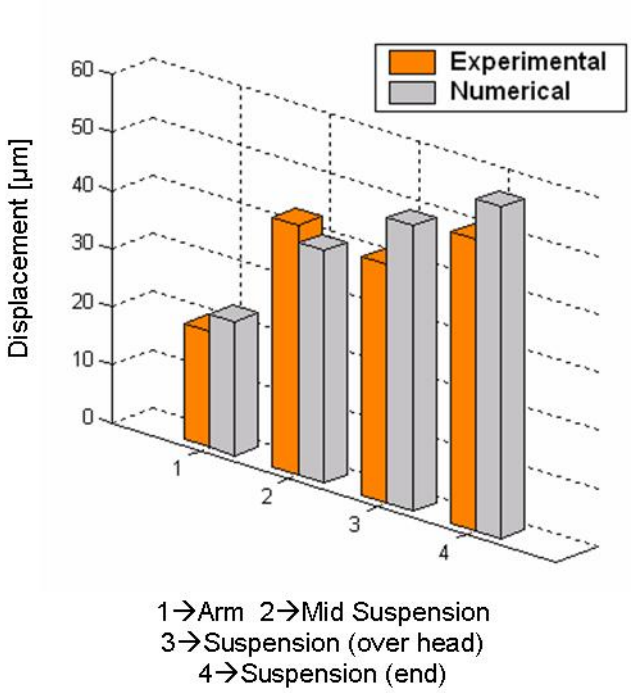

Figure 5.10: Maximum peak-to-peak displacement at different locations (operational shock)

operational shock is also shown in Figure 5.10. We observe that the displacement of the actuator arm is lower compared to the suspension. This is expected because the arm is much stiffer than the suspension. From Figures 5.9 and 5.10, we observe that the maximum peak-to-peak amplitudes of displacement for the arm and suspension are similar even though the specifications of shock loading conditions are significantly different.

5.1.4 Summary of Results for Shock Response of 1-inch HDD's

Non-operational shock data was obtained for 1-inch hard disk drives when the head stack assembly was parked on the load/unload ramp. The shock amplitude is about ten times higher than that of the operational shock event which takes place when the head is loaded and flying over the disk. The HSA is either in a track-follow mode or in a random track-seeking mode from inner diameter (ID) through the outer diameter (OD) of the disk. In the operational state, the head is separated from the disk by an air bearing with spacing on the order of 8 to 10 nm. For the microdrives tested, shock amplitude of about 200 G is enough to break the air bearing and allow the head/suspension to move either in the positive or negative z-direction from the plane of the disk. These shock events typically cause the head slap signature, i.e., disk dings and scratches, typically seen in disk drive failures. Alternatively, when the heads are parked on the load/unload ramp, shock amplitudes on the order of 2000 G or higher (for the microdrives tested) usually produce failure in other disk drives components, such as the motor bearing, pivot bearing and arm/suspension, rather than the head itself.

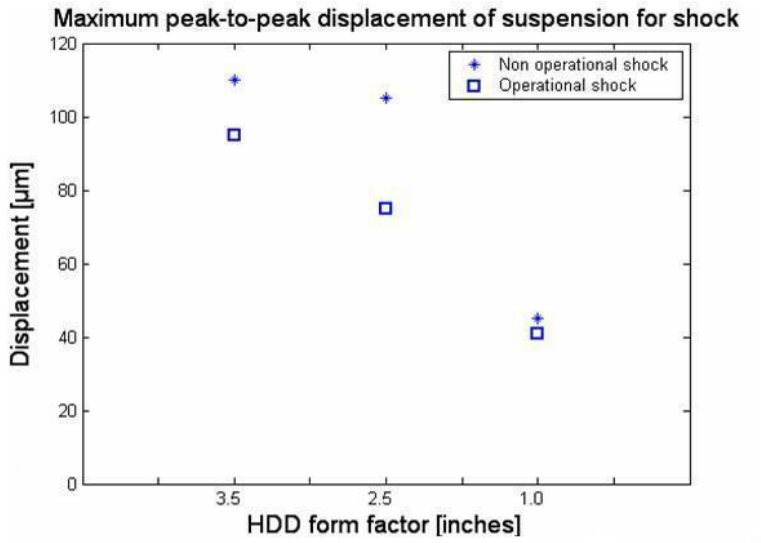

Figure 5.11: Comparison of the maximum peak-to-peak displacement of the suspension different form factor HDD's

Figure 5.11 shows the comparison of suspension displacement for non-operational and operational shock in three different form factor HDD's. The data for the 3.5 and 2.5 inch HDD's were taken from Murthy et al. [4] (discussed in Chapter 4). The data was measured for the shock specifications of the corresponding disk drives. We note that the specified amplitude of shock for the 3.5 inch HDD was the least and the amplitude of shock for the 1-inch HDD (microdrive) was the highest. However, we observe that the displacement of the suspension is the lowest for the microdrive and the highest for the 3.5-inch HDD. This is due to the fact that the suspension design in small form factor HDD has smaller beam length and higher resonant frequencies. It is desirable to have a lower displacement and in turn a better resistance to shock.

5.1.5 Conclusion for shock in 1-inch HDD's

A number of different microdrives from two different manufacturing vendors were investigated with regard to shock robustness of operational and non-operational shock parameters. From the results, the following conclusions can be made:

The shock response of the drives varied with manufacturing vendors due to differences in the main mechanical design of the drives. However, all the microdrives tested successfully met the designed shock specification provided by the vendor.

The hard errors ocurred at approximately 210 G for operational shock due to failure of the air bearing at the head disk interface. Failure of the microdrive in the non-operational case occured beyond 2000 G mostly due to failure of mechanical components such as the disk, voice coil magnet, etc.

To increase the operational shock specification from 200 G to 300 G the suspension design should be modified to prevent slap motion of the head/suspension against the disk. Increasing the gram load of the suspension can lead to reduction of slap shock of the head against the disk.

The numerical shock simulation compared close to the experimental results for both non-operational and operational shock.

5.2 Dynamic Response of 1-inch Form Factor Disk Drives to Vibration Loads

5.2.1 Overview

In the previous chapters, the effect of shock was investigated for the components of the head stack assembly, such as the actuator arm, suspension and the gimbal (or flexure). In this section, the effect of external vibrations on the head disk interface of 1-inch form factor hard disk drives using two different enclosures, the so-called thin enclosure and the thick enclosure is investigated. First, a modal analysis is performed for the two enclosures and the corresponding disk drive models. Then, the response of the head disk interface to applied in-plane and out-of-plane vibrations for both models is investigated.

5.2.2 Numerical Simulation Results

Modal Analysis

Figure 5.12 shows the top and front views of the two designs of 1-inch disk drive enclosures investigated in this study. The enclosure on the left is described in this thesis as the thick enclosure, while the enclosure on the right is described as the thin enclosure. The thick enclosure has a recessed area to hold the disk/spindle assembly and the actuator base. Modal analysis of the enclosures was performed first for the enclosures alone

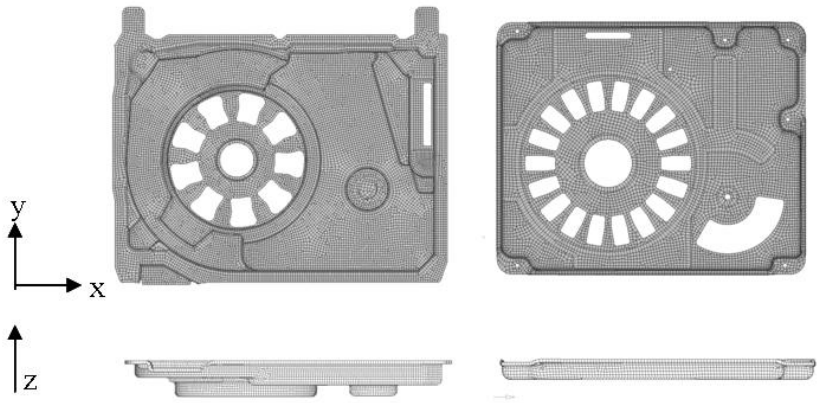

Figure 5.12: Two different 1-inch disk drive enclosures

and then for the assembled disk drives including the head suspension assembly, the spindle motor, and the disk. The enclosure was constrained at the holes that allow fastening of the disk drive to the system housing. The results of the modal analysis for the two enclosure designs and the respective disk drive models are shown in Figure 5.13(a) and Figure 5.13(b). In Figure 5.13(a) the first four fundamental modes are bending, torsion or combined bending and torsion modes of the enclosures. We observe from Figure 5.13(a) that the resonant frequencies of the thicker enclosure are higher than those of the thin enclosure, except the fourth fundamental mode.

The results of the modal analysis for the assembled disk drives (Figure 5.13(b)) show that the resonant frequencies are reduced due to the additional mass from the added components. The reduction is larger for the disk drive model with the thin enclosure compared to the model with the thick enclosure. This is due to the fact that the mass

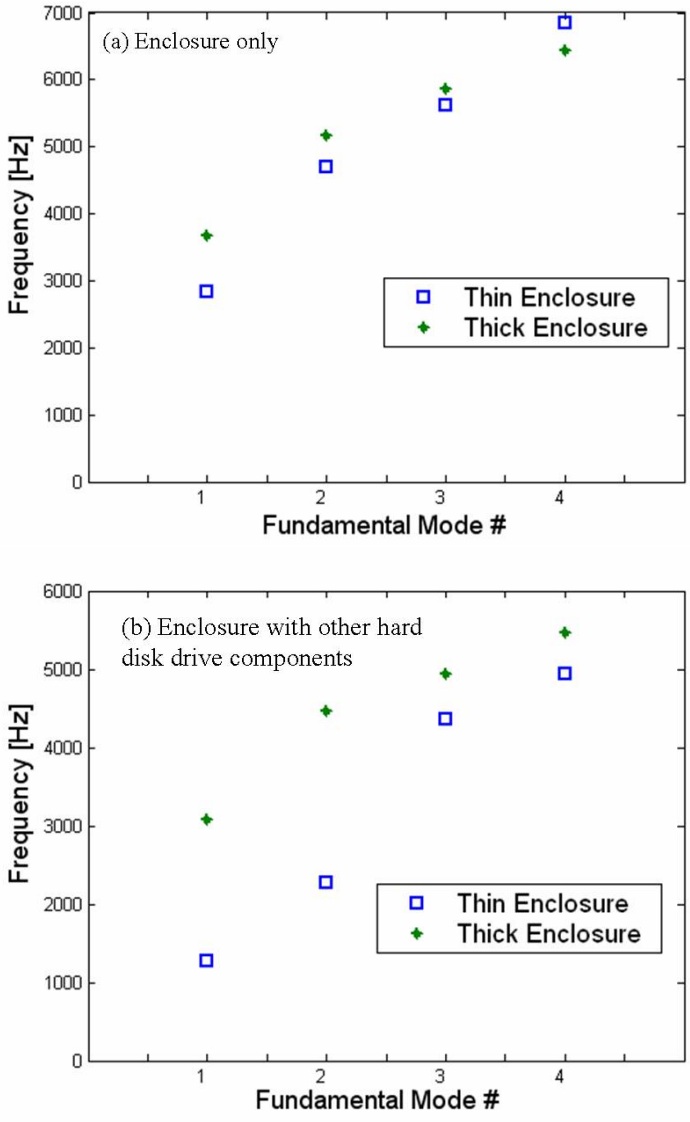

Figure 5.13: Modal results for (a) two enclosures (left) and (b) enclosure with additional disk drive components

of the thin enclosure by itself is smaller than the mass of the thick enclosure. Thus, the additional mass due to the components of the head stack assembly has a larger influence for the thin enclosure model than the thick enclosure model.

Vibration Analysis

To determine the effect of enclosures on the head disk interface, the in-plane and out-of-plane vibration response for the two 1-inch disk drive designs was investigated. The models include the pivot bearing, the head stack assembly , the spindle motor, the disk and the disk drive enclosures. The air bearing between the disk and the slider was approximated by five linear springs. A spring located at the center of the slider was used for the z-direction stiffness (200 N/mm). To approximate the pitch stiffness, two springs were positioned at the center of the leading edge and the center of the trailing edge of the slider. The stiffness value used for these springs was 40 N/mm. Similarly, two springs with stiffness values of 10 N/mm were positioned in the middle of the inner and the outer rail of the slider to approximate the roll stiffness.

To simulate the vibration response for the two 1-inch hard disk drive models, a random displacement between 1 and 10 kHz frequency range was created and applied to the hard disk enclosure (Figure 5.14). For the in-plane vibration analysis, the displacement was applied along the edge of the enclosure (x or y directions, (Figure 5.12)). For the out-of-plane vibration analysis, the displacement was applied at the base of the enclosure (z direction, (Figure 5.12)).

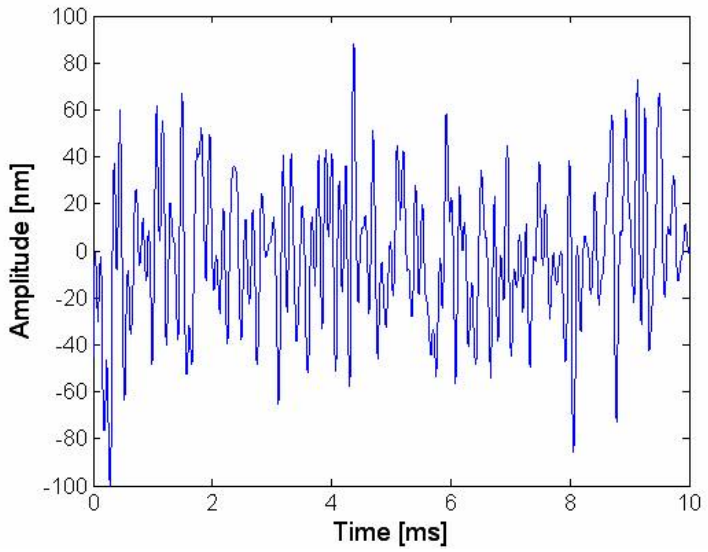

Figure 5.14: Random vibration applied to the enclosure

Figures 5.15 and 5.16 show the relative on-track and off-track displacement at the trailing edge center of the slider for externally applied in-plane vibrations. On-track vibrations are the relative displacements of the slider trailing edge center in the circumferential direction of the disk. Off- track vibrations are the relative displacements of the slider trailing edge center in the radial direction. Figure 5.15 shows the displacement time history for the 1-inch HDD model with the thin enclosure and Figure 5.16 shows the corresponding results for the 1-inch HDD model with the thick enclosure. The first two graphs in Figures 5.15 and 5.16 show the relative on-track and off-track displacement for vibrations applied in the x-direction. The last two graphs of Figures 5.15 and 5.16 show results for vibrations applied in the y-direction.

Figure 5.18 shows the maximum amplitude of on-track and off track vibrations for

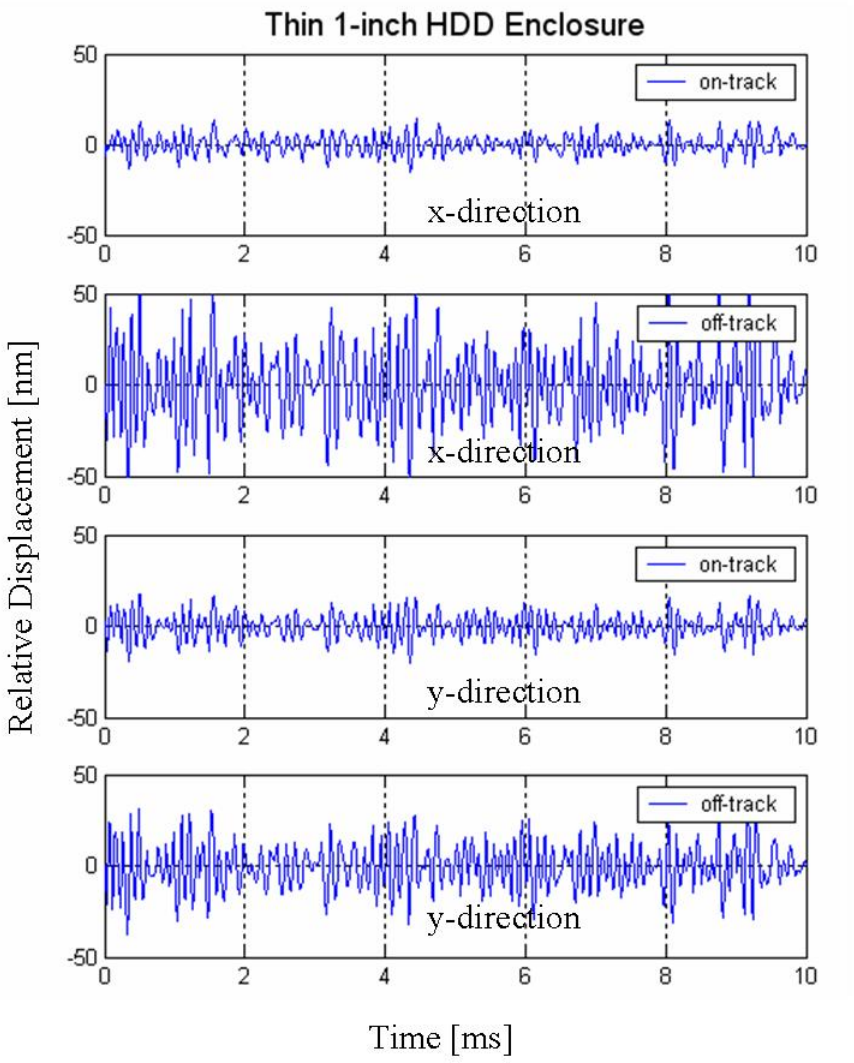

Figure 5.15: On-track and off-track displacement of the trailing edge center (TEC) for applied (in-plane) vibrations for the thin enclosure disk drive model

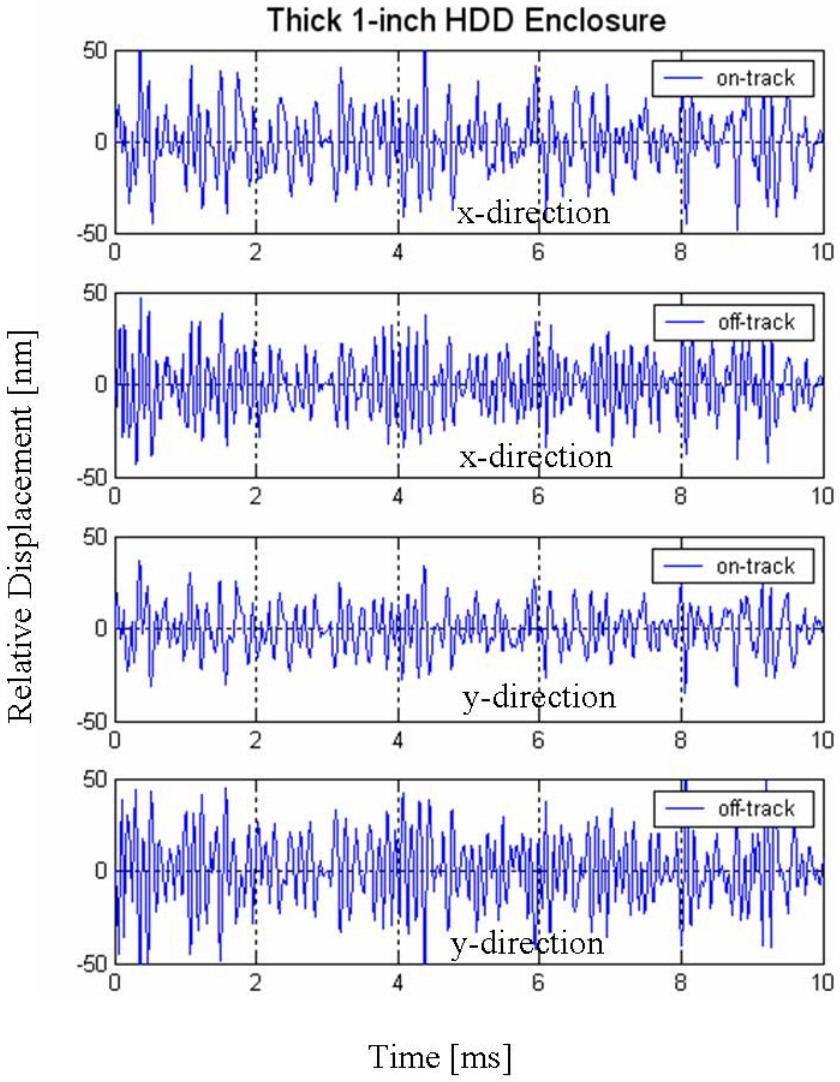

Figure 5.16: On-track and off-track displacement of the trailing edge center (TEC) for applied (in-plane) vibrations for the thick enclosure disk drive model

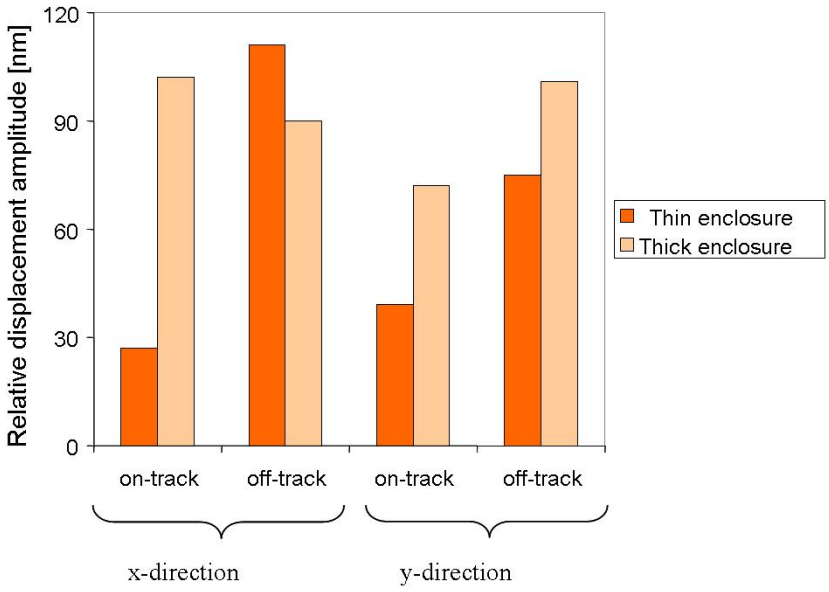

Figure 5.17: Maximum amplitude of relative displacement for in-plane vibration response

the two disk drive models. We observe that the relative on-track displacement of the slider for the thin enclosure model is smaller compared to the relative off-track displacement. The reason for this result is related to the stiffness of the suspension, which allows bending but restrains the motion of the slider in the tangential direction of the disk. The suspension vibrates around the pivot axis, which explains the larger radial displacements. However, for the thick enclosure model we observe that the relative on-track and off-track displacement amplitudes are nearly the same. The reason for this result is related to the geometry of the thick enclosure, since all other components of the model are similar to the components used in the thin enclosure model. In particular, in the thick enclosure a recess is present where the spindle motor and the pivot bearing are mounted. The recess provides a less rigid base for the spindle motor than the base of the thin enclosure, leading to additional displacements between spindle motor and pivot. This, in turn, results in higher relative displacements between slider and disk in the tangential direction of the disk. From the results for vibrations applied in the y-direction, we observe that the relative on-track displacement of the slider for both the thin and the thick enclosure models are smaller than the respective off-track displacements. The relative displacement amplitudes (both on-track and off-track) are smaller for the thin enclosure model compared to the thick enclosure model.

In addition to the in-plane vibrations, we have studied the response of the head/disk interface to vibrations applied normal to the enclosure. In this case the vibration amplitude was chosen to be ten times higher than in the previous investigation because of

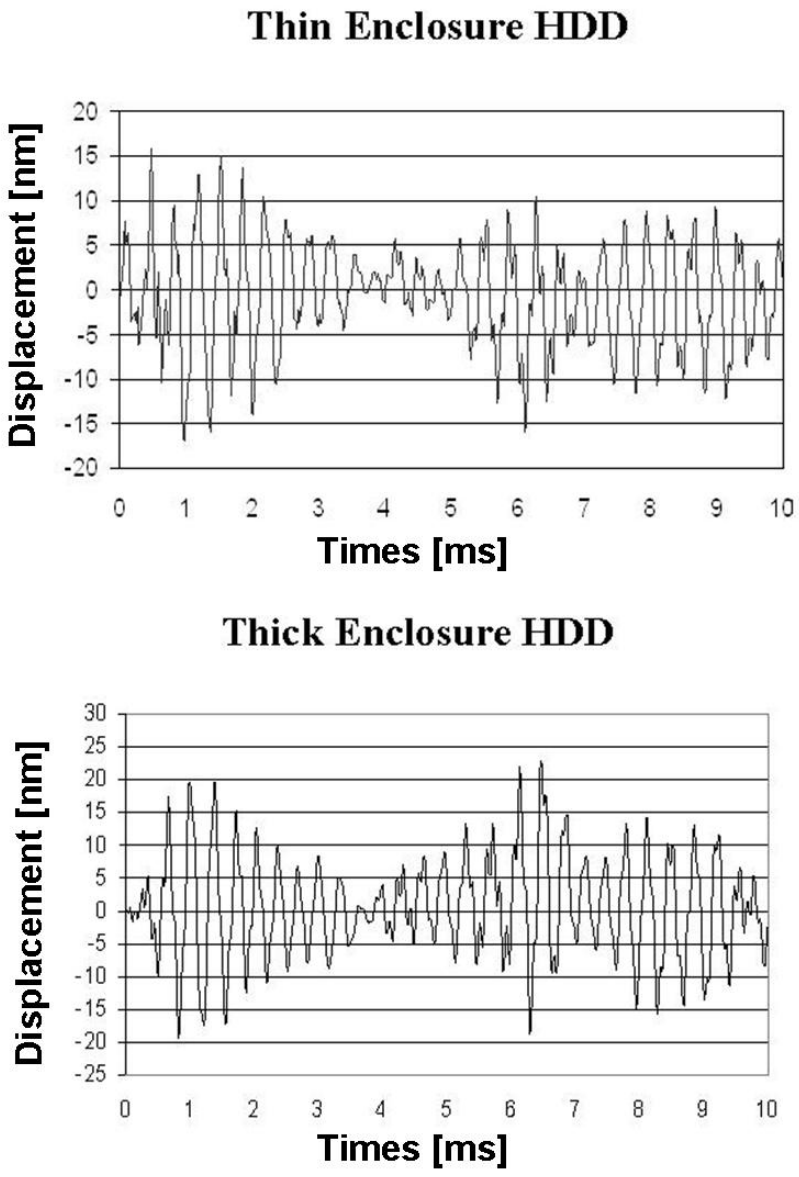

Figure 5.18: Relative displacement of slider TEC for applied (out-of-plane) z-direction vibration

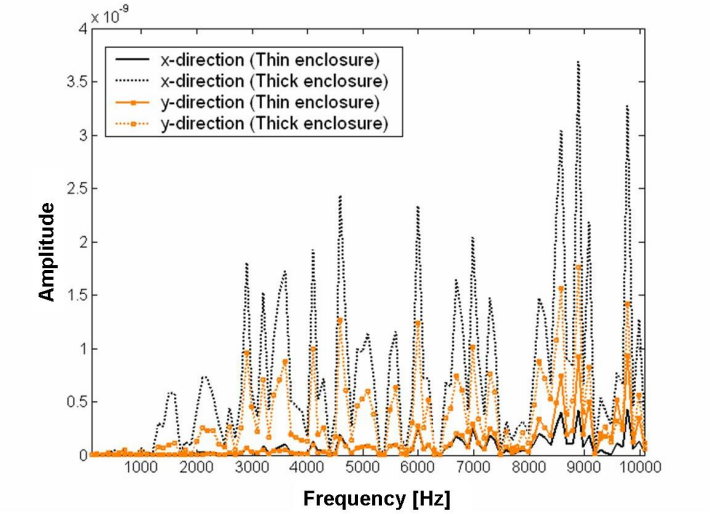

Figure 5.19: FFT of on-track relative displacement (in-plane vibration)

the high stiffness of the air bearing in the z-direction. The vibrations were applied at the bottom surface of the enclosure. For vibrations applied in the z-direction, we observe that the relative displacement of the slider trailing edge center is similar for both enclosure models (Figure 5.18). This result indicates that the air bearing dominates the response of the enclosures in the z-direction. Relative displacement in the z-direction is defined as the displacement of the trailing edge center node with respect to the enclosure displacement.

Figure 5.19 shows the Fast Fourier Transform (FFT) for the on-track relative displacements. The solid lines represent the results for the thin enclosure model and the dotted lines represent the results for the thick enclosure. The results for vibrations applied in both the x and the y-directions are shown. Since the applied vibrations have a frequency bandwidth between 1 and 10 kHz, no frequency peaks below 1 kHz are ob-

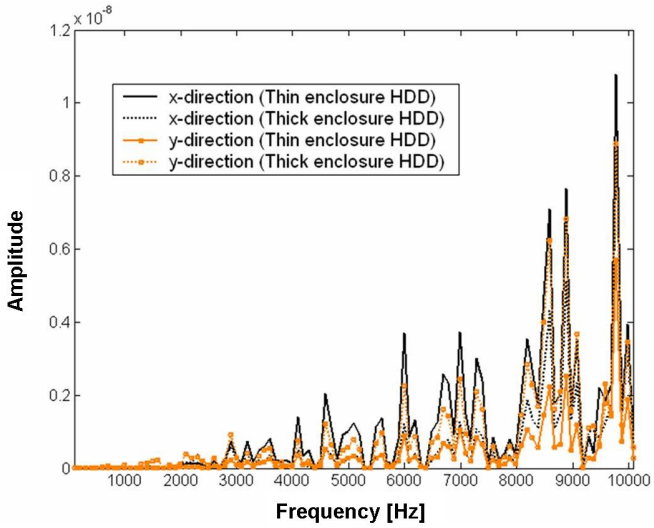

Figure 5.20: FFT of off-track relative displacement (in-plane vibration)

served. It can be seen that the FFT for the thin enclosure model has lower amplitudes in the entire frequency range compared to the thick enclosure model. This result is similar to the lower amplitudes of the respective relative displacements for in-plane vibrations. We also observe that all graphs show resonant peaks at the same frequencies. This indicates that all resonant peaks are caused by individual components of the hard disk drive rather than the enclosure. On the other hand, the different enclosure designs are seen to influence the relative amplitudes of the frequencies observed in the spectrum. The dominant peaks are the bending modes of the suspension, the gimbal modes and disk umbrella modes. Other peaks with higher frequency values are either combined modes of the head stack assembly or harmonics of the suspension bending mode.

Figure 5.20 shows the FFT for the off-track relative displacement data. We observe similar resonant peaks for both the thin and the thick enclosure models. In addition, we

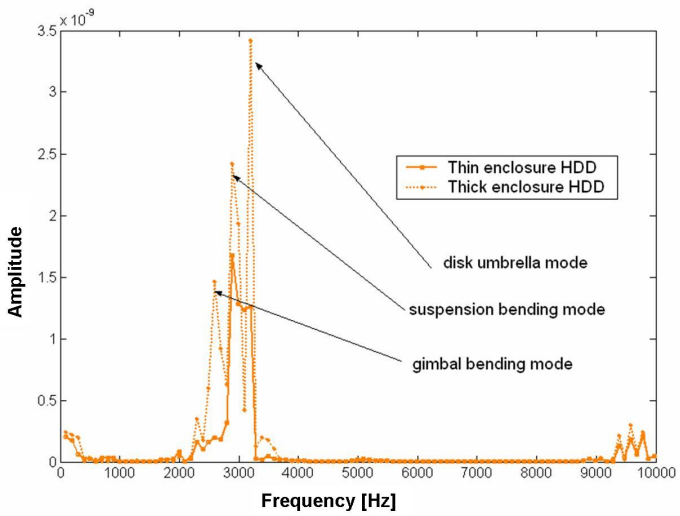

Figure 5.21: FFT of relative displacement (out-of-plane vibration)

note that the resonant peaks are the same for vibrations applied in the x-direction as well as the y-direction.

Figure 5.21 shows the FFT of the relative displacement in the z-direction for the thick and thin enclosure models. We observe that the dominant peaks are the first bending mode of the suspension (2.9 kHz), the first bending mode of the gimbal (2.6 kHz) and the umbrella mode of the disk (3.3 kHz). The amplitude of these modes is higher for the thick enclosure model compared to the thin enclosure model.

5.2.3 Summary for Vibrations in 1-inch HDDs

The dynamic response of the head disk interface was investigated numerically for two different designs of 1-inch hard disk drive enclosures, the so-called "thin" enclosure and the "thick" enclosure. First, a modal analysis for the two enclosure designs

was performed numerically. Then the in-plane and out-of-plane vibration response was determined for the HDD model with the two enclosure designs. From the simulation results, we observe that the thinner enclosure has better performance than the thick enclosure with respect to forced vibrations in terms of reduced amplitude of slider vibrations. Thus, we conclude that the design of 1-inch form factor hard disk drive enclosures has a significant effect on the dynamics of the head disk interface.

Acknowledgement

Part of the material in this chapter has been published in the *Microsystem Technologies Journal*: A. N. Murthy, M. Pfabe, J. Xu, and F. E. Talke, "Dynamic Response of 1-inch Form Factor Disk Drives to External Shock and Vibration Loads", Microsystem Technologies, published online, 2006.

The dissertation author was the primary investigator of this paper and was directly supervised by Prof. Frank E. Talke. The co-authors Mathias Pfabe and Jiafeng Xu have given their permission to include the material of the paper in this dissertation.

Part of the material in this chapter has been published in the *Microsystem Technologies Journal*: B. Feliss, A. N. Murthy, and F. E. Talke, "Microdrive Operational and Non-operational Shock and Vibration Testing,", Microsystem Technologies, published online, 2006.

The dissertation author was the primary investigator for the numerical analysis of this paper which was directly supervised by Prof. Frank E. Talke. The co-author Dr. Bert Feliss has kindly given his permission to include the experimental results of the paper (for comparison) in this dissertation.

Bibliography

[1] P. Bhargava, and D. B. Bogy, "Numerical Simulation of Operational-Shock in small form factor drives," submitted to ASME J of Tribology for publication

[2] E. M. Jayson and F. E. Talke, "Optimization of air bearing contours for shock performance of a hard disk drive," ASME J. of Tribology, vol. 127, pp. 878-883, October

[3] E. M. Jayson, J. M. Murphy, P. W. Smith and F. E. Talke, "Effects of air bearing stiffness on a hard disk drive subject to shock and vibration," ASME J of Tribology

[4] A. N. Murthy, B. Feliss, D. Gillis and F. E. Talke, "Experimental and Numerical Investigation of Shock Response in 3.5 and 2.5 inch form factor Hard Disk Drives", Microsystem Technologies, Vol.12 (no. 12): 1109-1116, 2006

[5] LS-Dyna, User and Theory manuals, Livermore Software Technology Corp

[6] GHI Systems, Inc, Linear Shock Machine , User manual and data sheet

[7] Polytec Inc, LDV user manuals

[8] Q. H. Zeng, and D. B. Bogy, "Numerical simulation of shock response of disk-suspension-slider air bearing systems in hard disk drives," Journal Microsystem Technologies

[9] Altair Hyperworks, Theory Manual, Altair Computing, Inc.

[10] Lee, S. J., Hong, S. K. and Lee, J. M., "A study of shock-resistance design of suspension subjected to impulsive excitation," IEEE Trans. on Magn., vol. 37, no. 2, pp. 826-830, 2001

[11] Lee, H. S, Chang, D. H., Sohn, J. S, Hong, M. P, and Choa, S. H., "Dynamic Absorber for Actuator Arm in A Disk Drive," Asia-Pacific Magnetic Recording Conference, 2000, pp MP13/1 - MP13/2

6

Theory of Hydrodynamic Lubrication and Application of the Reynolds Equation for the Head Disk Interface

In order to study the dynamics of the head disk interface during the operational state of a disk drive, one needs to solve the equation of motion of the disk drive together with the time-dependent Reynolds equation for the hyrdrodynamic lubrication of the head disk interface. Hydrodynamic lubrication can be present if two surfaces in relative motion are separated by a small distance. The governing equation for the flying behavior of a slider air bearing in a hard disk drive is the compressible Reynolds equation. Osborne Reynolds [3] was the first to derive a differential equation for imcompressible hydrodynamic lubrication by relating pressure, surface velocities, and film thickness. In this

chapter, the Reynolds equation and the slip flow correction due to rarefaction effects in the head disk interface are derived. The numerical solution of the Reynolds equation is described in the next chapter.

6.1 Derivation of the Reynolds Equation

The flying behavior of a magnetic recording slider and the formation of a self-acting airbearing are governed by the Reynolds equation [3] for compressible flow. The following assumptions are made in deriving the Reynolds equation for the head disk interface:

1. The head/disk spacing is much smaller than the slider dimensions
2. The air viscosity is constant
3. The flow is laminar
4. The inertia and body force of the air flow are negligible
5. The fluid is an isothermal gas, i.e., the air temperature is constant
6. The surfaces are smooth

A schematic of a typical slider bearing in a disk drive is shown in Figure 6.1. Here, B is the length of the slider; L is the width of the slider; U and V are disk velocities in the x and y directions, respectively; h is the spacing between the slider and the disk, and h_{min} is the minimum spacing at the trailing edge of the slider. The unknown velocity

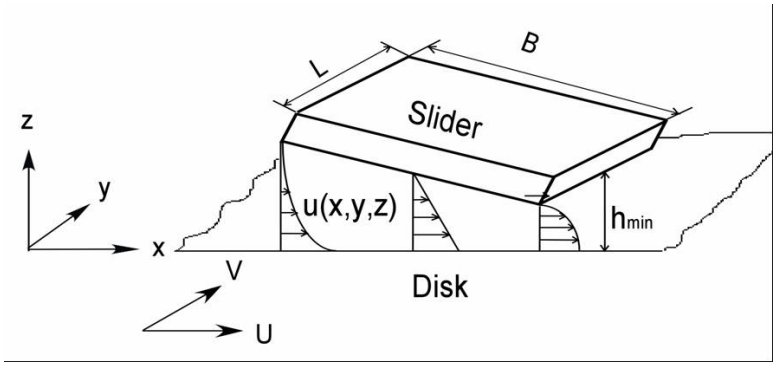

Figure 6.1: Schematic of a slider bearing

components are denoted by $u(x, y, z)$ and $v(x, y, z)$ in the x and y directions, respectively. The spacing h between slider and disk is much smaller than the length B of the slider.

The Reynolds equation is derived from the Navier-Stokes equation and the continuity equation. The Navier Stokes equation for compressible fluids is given by Eq. 6.1

$$\rho \frac{d\overrightarrow{v}}{dt} = \rho \overrightarrow{f} - \bigtriangledown p + \mu \cdot \triangle \overrightarrow{v} + \frac{\mu}{3} \bigtriangledown (\overrightarrow{v}) \tag{6.1}$$

where ρ is the density, $\overrightarrow{f}$ represents the body force, $\overrightarrow{v}$ is the velocity vector, p is the pressure, and μ is the viscosity of the fluid.

Neglecting the body forces which are mainly due to gravity, once can write Eq. 6.1 in Cartesian coordinates as:

$$\begin{aligned} \rho \frac{du}{dt} = -\frac{\partial p}{\partial x} + \frac{\partial}{\partial x}\left[2\mu \frac{\partial u}{\partial x} - \frac{2}{3}\mu\left(\frac{\partial u}{\partial x} + \frac{\partial v}{\partial y} + \frac{\partial w}{\partial z}\right)\right] + \\ \frac{\partial}{\partial y}\left[\mu\left(\frac{\partial u}{\partial y} + \frac{\partial v}{\partial x}\right)\right] + \frac{\partial}{\partial z}\left[\mu\left(\frac{\partial u}{\partial z} + \frac{\partial w}{\partial x}\right)\right] \end{aligned} \tag{6.2}$$

$$\rho\frac{dv}{dt} = -\frac{\partial p}{\partial y} + \frac{\partial}{\partial y}\left[2\mu\frac{\partial v}{\partial y} - \frac{2}{3}\mu\left(\frac{\partial u}{\partial x} + \frac{\partial v}{\partial y} + \frac{\partial w}{\partial z}\right)\right] + \frac{\partial}{\partial z}\left[\mu\left(\frac{\partial v}{\partial z} + \frac{\partial w}{\partial y}\right)\right] + \frac{\partial}{\partial x}\left[\mu\left(\frac{\partial u}{\partial y} + \frac{\partial v}{\partial x}\right)\right] \tag{6.3}$$

$$\rho\frac{dw}{dt} = -\frac{\partial p}{\partial z} + \frac{\partial}{\partial z}\left[2\mu\frac{\partial w}{\partial z} - \frac{2}{3}\mu\left(\frac{\partial u}{\partial x} + \frac{\partial v}{\partial y} + \frac{\partial w}{\partial z}\right)\right] + \frac{\partial}{\partial x}\left[\mu\left(\frac{\partial w}{\partial x} + \frac{\partial u}{\partial z}\right)\right] + \frac{\partial}{\partial y}\left[\mu\left(\frac{\partial v}{\partial z} + \frac{\partial w}{\partial y}\right)\right] \tag{6.4}$$

Performing an order of magnitude analysis, we obtain:

$$u = \mathcal{O}(U), v = \mathcal{O}(V); \quad x = \mathcal{O}(L), y = \mathcal{O}(B), z = \mathcal{O}(h)$$

Hence, the derivatives in the x, y and z-directions have the following orders of magnitude

$$\frac{\partial}{\partial x}\left[\mu\frac{\partial u}{\partial x}\right] \sim \mathcal{O}\left(\mu\frac{U}{B^2}\right) \tag{6.5}$$

$$\frac{\partial}{\partial y}\left[\mu\frac{\partial u}{\partial y}\right] \sim \mathcal{O}\left(\mu\frac{U}{B^2}\right) \tag{6.6}$$

$$\frac{\partial}{\partial z}\left[\mu\frac{\partial u}{\partial z}\right] \sim \mathcal{O}\left(\mu\frac{U}{h^2}\right) \tag{6.7}$$

From Eq. (6.5), (6.6), and (6.7), we observe that the magnitude of the term involving the derivative in the z-direction is much larger than the magnitude of the terms involving derivatives in the x and y directions, respectively, since $h \ll B$. Thus, we can neglect

the terms involving derivatives in the x and y directions as compared to terms involving derivatives in the z-direction, and Eq. 6.2-6.4 can be rewritten as follows

$$\begin{aligned} \rho\frac{du}{dt} &= -\frac{\partial p}{\partial x} + \frac{\partial}{\partial z}\left(\mu\frac{\partial u}{\partial z}\right) \\ \rho\frac{dv}{dt} &= -\frac{\partial p}{\partial y} + \frac{\partial}{\partial z}\left(\mu\frac{\partial v}{\partial z}\right) \\ \frac{\partial p}{\partial z} &= 0 \end{aligned} \tag{6.8}$$

The terms on the left hand side of Eq. 6.8 represent the inertia force and the terms on the right hand side represent the pressure and viscous forces. We can write the inertia forces as

$$\begin{aligned} \rho\frac{du}{dt} &= \rho\left(\frac{\partial u}{\partial t} + u\frac{\partial u}{\partial x} + v\frac{\partial u}{\partial y} + w\frac{\partial u}{\partial z}\right) \\ \rho\frac{dv}{dt} &= \rho\left(\frac{\partial v}{\partial t} + u\frac{\partial v}{\partial x} + v\frac{\partial v}{\partial y} + w\frac{\partial v}{\partial z}\right) \end{aligned} \tag{6.9}$$

An order-of-magnitude comparison of the ratio of inertia terms to the viscous terms shows that:

$$\frac{\rho u\frac{\partial u}{\partial x}}{\frac{\partial}{\partial z}\left(\mu\frac{\partial u}{\partial z}\right)} = \mathcal{O}\left(\frac{\rho\frac{U^2}{B}}{\mu\frac{U}{h^2}}\right) = \mathcal{O}\left(\frac{\rho UB}{\mu}\left(\frac{h}{B}\right)^2\right) \ll 1 \quad (since\, h \ll B) \tag{6.10}$$

From Eq. (6.10), we define a modified Reynolds number Re^* given by

$$Re^* = \frac{\rho UB}{\mu}\left(\frac{h}{B}\right)^2 = Re\cdot\left(\frac{h}{B}\right)^2 \tag{6.11}$$

Neglecting the inertia terms in Eq. 6.8, we obtain

$$\begin{aligned}\frac{\partial p}{\partial x} &= \frac{\partial}{\partial z}\left(\mu\frac{\partial u}{\partial z}\right)\\ \frac{\partial p}{\partial y} &= \frac{\partial}{\partial z}\left(\mu\frac{\partial v}{\partial z}\right)\end{aligned} \tag{6.12}$$

and

$$\frac{\partial p}{\partial z} = 0 \tag{6.13}$$

Eq. (6.12) represents the balance of pressure forces and viscous forces in a hydrodynamic lubrication film. Since the spacing between the slider and the disk is small, a large velocity gradient exists that generates shear forces. These shear forces are balanced by the pressure gradient in the slider bearing. The resulting flow is a combination of Couette flow (M. F. A. Couette, 1858-1943) and Poiseuille flow (J. Poiseuille, 1799-1869)

Eq. 6.13 implies that the pressure in the slider air bearing is not a function of z, i.e., the pressure is constant over the film thickness h. Pressure is only a function of x and y. Hence, the pressure gradients $\partial p/\partial x$ and $\partial p/\partial y$ can be treated as a constant when the two equations of Eq. 6.12 are integrated with respect to z. This results in two equations for the velocity profiles u and v after integration of Eq. 6.12 as shown below

$$\begin{aligned}\frac{\partial u}{\partial z} &= \frac{1}{\mu}\frac{\partial p}{\partial x}z + \frac{c_1}{\mu}\\ \frac{\partial v}{\partial z} &= \frac{1}{\mu}\frac{\partial p}{\partial y}z + \frac{c_2}{\mu}\end{aligned} \tag{6.14}$$

where $c_1$and c_2 are constants of integration.

For most fluid films, it can be assumed that viscosity μ is constant across the film thickness. Integrating Eq. 6.14 with respect to z once again gives

$$\begin{aligned} u &= \frac{1}{2\mu}\frac{\partial p}{\partial x}z^2 + \frac{c_1}{\mu}z + c_3 \\ v &= \frac{1}{2\mu}\frac{\partial p}{\partial y}z^2 + \frac{c_2}{\mu}z + c_4 \end{aligned} \tag{6.15}$$

The constants of integration in Eq. 6.15 can be determined by considering the boundary conditions of the flow in the bearing. The no-slip condition states that the flow velocity at a surface is equal to the surface velocity, i.e., there exists no slip between the flow and the surface. The conditions of no-slip in slider bearings are

$$\begin{aligned} at\, z = 0,\, u = U,\, v = V \\ at\, z = h,\, u = 0,\, v = 0 \end{aligned} \tag{6.16}$$

Applying the no-slip boundary conditions shown above, we can determine the constants of integration $c_1,\, c_2,\, c_3$, and c_4, and rewrite Eq. 6.15 as

$$\begin{aligned} u &= \frac{1}{2\mu}\frac{\partial p}{\partial x}\left(z^2 - zh\right) + U\left(1 - \frac{z}{h}\right) \\ v &= \frac{1}{2\mu}\frac{\partial p}{\partial y}\left(z^2 - zh\right) + V\left(1 - \frac{z}{h}\right) \end{aligned} \tag{6.17}$$

In Eq.6.17, u and v represent the flow velocity which is a linear superposition of a Poiseuille flow driven by the pressure gradient $\partial p/\partial x$ and $\partial p/\partial y$, and a Couette flow driven by the disk velocity.

The above velocity profiles are used in the continuity equation for compressible flow, shown in Eq. 6.18, to derive the Reynolds equation.

$$\frac{\partial \rho}{\partial t} + \nabla \cdot (\rho \overrightarrow{v}) = 0 \tag{6.18}$$

We can write Eq. 6.18 in Cartesian coordinates as

$$\frac{\partial \rho}{\partial t} + \frac{\partial}{\partial x}(\rho u) + \frac{\partial}{\partial y}(\rho v) + \frac{\partial}{\partial z}(\rho w) = 0 \tag{6.19}$$

Integrating this equation over the film thickness we obtain

$$\int_0^h \left[\frac{\partial \rho}{\partial t} + \frac{\partial}{\partial x}(\rho u) + \frac{\partial}{\partial y}(\rho v) + \frac{\partial}{\partial z}(\rho w) \right] dz = 0 \tag{6.20}$$

Integration and differentiation can be interchanged in Eq. (6.20) according to the Leibnitz rule:

$$\int_{h_1(x)}^{h_2(x)} \frac{\partial}{\partial x}[f(x,y,z)]\, dz = -f(x,y,z)\frac{\partial h}{\partial x} + \frac{\partial}{\partial x}\left(\int_{h_1(x)}^{h_2(x)} f(x,y,z) \right) dz \tag{6.21}$$

Using the Leibnitz rule of integration given in Eq. 6.21, we can determine the integral of each term in Eq. 6.20. For the u component, we obtain

$$\begin{aligned}\int_0^h \frac{\partial}{\partial x}(\rho u)\,dz &= -(\rho u)_{z=h}\frac{\partial h}{\partial x} + \frac{\partial}{\partial x}\left(\int_0^h (\rho u dz)\right) = \frac{\partial}{\partial x}\left(\int_0^h (\rho u dz)\right) \\ &= \frac{\partial}{\partial x}\int_0^h \rho\left[\frac{1}{2\mu}\frac{\partial p}{\partial x}\left(z^2 - zh\right) + U\left(1 - \frac{z}{h}\right)\right] dz \\ &= \frac{\partial}{\partial x}\left[-\rho\frac{1}{2\mu}\frac{\partial p}{\partial x}\left(\frac{1}{3}z^3 - \frac{1}{2}z^2 h\right) + \rho U\left(z - \frac{z^2}{2h}\right)\right]_0^h \\ &= \frac{\partial}{\partial x}\left[\frac{1}{2\mu}\frac{\partial p}{\partial x}\frac{1}{6}\rho h^3 + \frac{U}{2h}\rho h\right]\end{aligned} \tag{6.22}$$

Similarly, we can obtain the v component as

$$\begin{aligned}\int_0^h \frac{\partial}{\partial y}(\rho v)\,dz &= -(\rho v)_{z=h}\frac{\partial h}{\partial y} + \frac{\partial}{\partial y}\left(\int_0^h (\rho v dz)\right) = \frac{\partial}{\partial y}\left(\int_0^h (\rho v dz)\right) \\ &= \frac{\partial}{\partial y}\int_0^h \rho\left[\frac{1}{2\mu}\frac{\partial p}{\partial y}\left(z^2 - zh\right) + V\left(1 - \frac{z}{h}\right)\right] dz \\ &= \frac{\partial}{\partial y}\left[-\rho\frac{1}{2\mu}\frac{\partial p}{\partial y}\left(\frac{1}{3}z^3 - \frac{1}{2}z^2 h\right) + \rho V\left(z - \frac{z^2}{2h}\right)\right]_0^h \\ &= \frac{\partial}{\partial y}\left[\frac{1}{2\mu}\frac{\partial p}{\partial y}\frac{1}{6}\rho h^3 + \frac{V}{2h}\rho h\right]\end{aligned} \tag{6.23}$$

Finally, we can integrate the w component as

$$\begin{aligned}\int_0^h \frac{\partial}{\partial z}(\rho w)\,dz &= (\rho w)_{z=h} = \rho\frac{dh}{dt}\,|_{z=h} \\ &= \rho\frac{\partial h}{\partial t} + \rho u\frac{\partial h}{\partial x}\,|_{z=h} + \rho v\frac{\partial h}{\partial y}\,|_{z=h} = \rho\frac{\partial h}{\partial t}\end{aligned} \tag{6.24}$$

Combining Eq. 6.20 and Eq. 6.22 - Eq.6.24, we obtain

$$\frac{\partial}{\partial x}\left(\frac{\rho h^3}{\mu}\frac{\partial p}{\partial x}\right) + \frac{\partial}{\partial y}\left(\frac{\rho h^3}{\mu}\frac{\partial p}{\partial y}\right) = 6U\frac{\partial}{\partial x}(\rho h) + 6V\frac{\partial}{\partial y}(\rho h) + 12\frac{\partial}{\partial t}(\rho h) \tag{6.25}$$

For ideal gas, the density is directly proportional to the pressure and is given by

$$p = \rho RT \tag{6.26}$$

Substituting Eq.6.26 in Eq. 6.25, we obtain

$$\frac{\partial}{\partial x}\left(ph^3\frac{\partial p}{\partial x}\right) + \frac{\partial}{\partial y}\left(ph^3\frac{\partial p}{\partial y}\right) = 6\mu U\frac{\partial}{\partial x}(ph) + 6\mu V\frac{\partial}{\partial y}(ph) + 12\mu\frac{\partial}{\partial t}(ph) \tag{6.27}$$

Eq. 6.27 is the generalized Reynolds equation describing the hydrodynamic lubrication of a slider bearing for compressible flow. The terms on the left hand side of the Reynolds equation are the diffusive terms derived from the pressure driven Poiseuille flow. The velocity terms on the right hand side of the Reynolds equation are the convective terms derived from the Couette flow. The time-dependent term on the right hand side is referred to as the squeeze term and can be neglected for steady state conditions.

We define the following non-dimensional variables

$$\begin{aligned} P &= \frac{p}{p_a} \\ X = \frac{x}{B},\ Y &= \frac{y}{L} \\ H &= \frac{h}{h_{min}} \\ T &= \frac{t}{B/U} = t\omega \end{aligned} \tag{6.28}$$

where, $p_a$is the ambient pressure, B and L are the length and width of the slider bearing, $h_{min}$is the minimum spacing between the slider and the disk, and ω is a representative approximation of the angular frequency.

Introducing non-dimensional variables given in Eq. 6.28, we can write the non-dimensional Reynolds equation as

$$\frac{\partial}{\partial X}\left(PH^3\frac{\partial P}{\partial X}\right)+\frac{\partial}{\partial Y}\left(PH^3\frac{\partial P}{\partial Y}\right)=\Lambda_x\frac{\partial}{\partial X}(PH)+\Lambda_y\frac{\partial}{\partial Y}(PH)+\sigma\frac{\partial}{\partial T}(PH) \tag{6.29}$$

where Λ_x and Λ_y are the bearing numbers in the x and y directions, respectively, and σ is the squeeze number:

$$\begin{aligned}\Lambda_x &= \frac{6\mu UB}{p_a h_{min}^2}\\ \Lambda_y &= \frac{6\mu VL}{p_a h_{min}^2}\\ \sigma &= \frac{12\mu\omega B^2}{p_a h_{min}^2}\end{aligned} \tag{6.30}$$

6.2 Slip Flow Corrections for Very Low Spacing at the Head Disk Interface

The derivation of the Reynolds equation in the previous section is based on the continuum theory of fluid mechanics, i.e., no-slip boundary conditions are assumed. This assumption is valid for flows where the molecular mean free path is negligible compared to the typical dimensions the area of the flow. Also, the effect of molecular mean free path is negligible only if the fluid adjacent to a wall is in thermodynamic equilibrium, which is a condition that requires a very high frequency of molecular collisions with

the wall. For the case of hydrodynamic lubrication of slider bearings for the head disk interface, the fluid is air, and the spacing is of the same order of magnitude as the mean free path of the air flow. When the spacing becomes comparable to the mean free path, slip occurs between the air and the wall. This phenomenon is called "rarefaction effect". The ratio of the molecular mean free path to the fluid film thickness is denoted as the Knudsen number, and is used as a measure for rarefaction effects. The Knudsen number, Kn is defined as

$$Kn = \frac{\lambda}{h} = \frac{\lambda_a \, p_a}{hp} \tag{6.31}$$

where, λ is the molecular mean free path, λ_a is the mean free path of air at ambient pressure p_a, and h is the fluid film thickness.

The value of the Knudsen number, Kn, determines the degree of rarefaction occurring in a fluid flow. The following regimes are generally defined:

$$\begin{aligned} Kn < 0.01 \;\; &\text{continuum flow} \\ 0.01 < Kn < 3 \;\; &\text{slip flow} \\ Kn > 3, \; \frac{Kn}{Re^{0.5}} < 10 \;\; &\text{transition flow} \\ \frac{Kn}{Re^{0.5}} > 10 \;\; &\text{molecular flow} \end{aligned} \tag{6.32}$$

where Re is the Reynolds.

Due to the extremely small spacing of the head disk interface, the standard Reynolds equation for slider bearings must be corrected to account for the rarefaction effects or slip at the boundaries.

If the spacing between the slider and the disk is less than 600nm, the Knudsen number becomes greater than 0.1. In this case, the flow behavior deviates from a continuum flow, and the non-slip boundary conditions are no longer satisfied [12]. The boundary conditions for so-called first order slip were introduced by Burgdorfer [12] and boundary conditions for so-called second order slip were introduced by Hsia and Domoto [13] 1983. The most recent and generally accepted slip model was developed by Fukui and Kaneko [14]. This correction is based on the linearized Boltzmann equation.

The modified Reynolds equation can be written as (Wahl, 1994 [1])

$$\bigtriangledown \cdot \left(Qph^3 \bigtriangledown p\right) = 6\mu V \cdot \bigtriangledown (ph) + 12\mu \frac{\partial (ph)}{\partial t} \tag{6.33}$$

where p is the pressure, h is the spacing, μ is the viscosity, V is the velocity and Q is the dimensionless flow rate. Q is defined as the ratio of the Poiseuille flow rate Q_p to the continuum flow rate Q_{con} , i.e.,

$$Q = \frac{Q_p}{Q_{con}} \tag{6.34}$$

The continuum flow rate, $Q_{con}$is given by

$$Q_{con} = \frac{D}{6} \tag{6.35}$$

where D is the modified inverse Knudsen number, defined in terms of the local pressure p, the atmospheric pressure p_a, the spacing h, and the atmospheric mean free path λ_a, i.e.,

$$D = \frac{\sqrt{\pi}}{2} Kn^{-1} = \frac{\sqrt{\pi}}{2} \frac{h}{\lambda} = \frac{\sqrt{\pi}}{2} \frac{ph}{p_a \lambda_a} \tag{6.36}$$

The flow rate for the Poiseuille flow depends on the order of slip flow correction. The Poiseuille flow rate for the first order slip correction is given as

$$Q_{p1} = \frac{D}{6} + \frac{\sqrt{\pi}}{2} \tag{6.37}$$

For second order slip correction, the Poiseuille flow rate is

$$Q_{p2} = \frac{D}{6} + \frac{\sqrt{\pi}}{2} + \frac{\pi}{2D} \tag{6.38}$$

If the spacing decreases to about 30 nm, the Knudsen number is approximately 2 and the "Boltzmann" correction must be used (Fukui and Kaneko, 1990 [15]). The Poiseuille flow based on the Boltzmann equation is given as

$$\begin{aligned} Q_{pB} &= \frac{D}{6} + 1.0162 + \frac{1.0653}{D} - \frac{2.1354}{D^2} && (5 \leq D) \\ Q_{pB} &= 0.13852D + 1.25087 + \frac{1.5653}{D} - \frac{0.00969}{D^2} && (0.15 \leq D \leq 5) \\ Q_{pB} &= -2.22919D + 2.10673 + \frac{0.01653}{D} - \frac{0.0000694}{D^2} && (0.01 \leq D \leq 0.15) \end{aligned} \tag{6.39}$$

where Q_{pB} indicates the Boltzmann correction.

Using the non-dimensional variables of Eq. (6.28), we can write the Reynolds equation with rarefaction effects as:

$$\frac{\partial}{\partial X}\left(Q\,PH^3\frac{\partial P}{\partial X}\right)+\frac{\partial}{\partial Y}\left(Q\,PH^3\frac{\partial P}{\partial Y}\right)=\Lambda_x\frac{\partial}{\partial X}\left(PH\right)+\Lambda_y\frac{\partial}{\partial Y}\left(PH\right)+\sigma\frac{\partial}{\partial T}\left(PH\right) \tag{6.40}$$

where the rarefaction term Q is determined from either Eq. (6.37), (6.38), or (6.39); and Λ_x, Λ_y and σ are obtained from Eq. (6.30).

The Reynolds equation is a nonlinear partial differential equation which cannot be solved in closed form. To determine the pressure in the Reynolds equation, for the general case, iterative numerical methods are required. The airbearing simulator used in this dissertation uses a finite element solution of the Reynolds equation originally developed by Wahl [1] at the Center for Magnetic Recording Research (CMRR), University of California San Diego.

Bibliography

[1] Albert Burgdorfer, "The Influence of the Molecular Mean Free Path on the Performance of Hydrodynamic Gas Lubricated Bearings", *Transactions of the ASME*, Series D, vol. 81, pp. 94-100, 1959

[2] Y. Hsia, G. Domoto, "An Experimental Investigation of Molecular Rarefaction Effects in Gas Lubricated Bearings at Ultra-Low Clearances", *Transactions of the ASME, Journal of Lubrication Technology*, vol. 105, pp. 120-130, 1983

[3] S. Fukui and R. Kaneko, "Analysis of Ultra-Thin Gas Film Lubrication Based on Linearized Boltzmann Equation: First Report - Derivation of a Generalized Lubrication Equation Including Thermal Creep Flow", *Transactions of the ASME, Journal of Tribology*, Vol. 110, 1988, pp. 253-262

[4] S. Fukui and R. Kaneko, "A Database for Interpolation of Poiseuille Flow Rates for High Knudsen Number Lubrication Problems", *IEEE Transactions on Magnetics,* 24 (6), pp. 2751-2753, 1988

[5] S. Fukui and R. Kaneko, "Analysis of Flying Characteristics of Magnetic Heads with Ultra-Thin Spacings Based on the Boltzmann Equation", *Transactions of the ASME, Journal of Tribology*, Vol. 112, 1990, pp. 78-83

[6] Wahl, M., Lee, P., and Talke, F, "An Efficient Finite Element-Based Air Bearing Simulator for Pivoted Slider Bearings Using Bi-Conjugate Gradient Algorithms", *Tribology Transactions*, Vol.39 (no. 1): 130-138, 1996

7

Finite Element Solution of the Reynolds Equation and its Application to Slider Design

The finite element method is a good choice for solving partial differential equations over complex domains, when the domain changes, or when the desired precision varies over the entire domain. In the finite element method, a continuous domain (such as the air bearing surface in hydrodynamic lubrication problems) is divided into a finite number of elements. The change of an unknown dependent variable is approximated within each discrete element by an interpolation function ("shape function"). This is given as:

$$\Psi(x,y,z) = \sum_{i=1}^{N} N_i(x,y,z)\,\Psi_i \tag{7.1}$$

where Ψ is the unknown dependent variable, Ψ_i is the value of Ψ at node i, and $N_i$are the interpolation or shape functions.

The finite-element method originated from the need for solving complex elasticity and structural analysis problems in civil and aeronautical engineering. The development of the finite element methods can be traced back to the work by Alexander Hrennikoff (1941) [1] and Richard Courant (1942) [2]. Although the approaches used by these pioneers are significantly different, they shared one essential characteristic, i.e., mesh discretization of a continuous domain into a set of discrete sub-domains called "elements". Hrennikoff's work used an approach that discretizes the domain by using a lattice analogy [1], while Courant used an approach that divides the domain into finite triangular subregions for solution of second order elliptic partial differential equations that arise from the problem of torsion of a cylinder [2]. Courant developed finite element models and recalculated several earlier results for partial differential equations developed by Rayleigh, Ritz, and Galerkin. Significant development of the finite element method began in the middle to late 1950's for airframe analysis in the 1960's for use in civil engineering structural analysis [7], [8], [9]. The method was provided with a rigorous mathematical base in 1973 with the publication of Strang and Fix's book: "An Analysis of The Finite Element Method" [11], and has since been generalized into a branch of applied mathematics for numerical modeling of physical systems in a wide

variety of engineering disciplines.

The development of the finite element method in structural mechanics is often based on an energy principle, e.g., the virtual work principle or the minimum total potential energy principle, which provides a general, intuitive and physical basis that has a great appeal to structural engineers. However, in hydrodynamic lubrication problems, the weighted residual method based on the Galerkin formulation is more commonly used. The finite element solution of the Reynolds equation in this dissertation is based on the Galerkin weighted residual method.

7.1 Finite Element Solution of the Steady State Reynolds Equation

The simulator used in this dissertation uses a numerical technique based on the Galerkin weighted residual finite element method (Wahl [1]). The differential equation forming the residual function is the Reynolds equation developed for pivoted slider bearings.

Using the Reynolds equation as a residual function in the general equation for the weighted residual method, one obtains

$$\int_{\Omega} \left\{ \nabla \cdot \left(\overline{Q} p h^3 \nabla p \right) - 6\mu V \nabla \left(ph \right) + 12\mu \frac{\partial}{\partial t} \left(ph \right) \right\} W \, d\Omega = 0 \tag{7.2}$$

where Ω is the domain and W is a weight function.

Since Eq. 7.2 contains a 2^{nd} order derivative of pressure, the first term on the left hand side of Eq. 7.2 is expanded using the product rule of differentiation,

$$(\nabla \cdot A)\, B = \nabla \cdot (BA) - \nabla B \cdot A \tag{7.3}$$

where $A = \overline{Q} p h^3 \nabla p$ and $B = W$.

Eq. (7.2) can then be written as

$$\int_{\Omega} \{\nabla \cdot \left(\overline{Q} p h^3 \nabla p\right) W - \left(\overline{Q} p h^3 \nabla p\right) \cdot \nabla W - 6\mu V \cdot \nabla (ph)\, W + 12\mu \frac{\partial}{\partial t} (ph)\, W\}\, d\Omega = 0 \tag{7.4}$$

Applying the divergence theorem,

$$\int_{\Omega} \nabla \cdot A \, d\Omega = \oint_{\sigma} A\, n \, d\sigma \tag{7.5}$$

we obtain

$$\oint_{\sigma} \left(\overline{Q} p h^3 \nabla p W\right) n \, d\sigma + \int_{\Omega} \left\{ - \left(\overline{Q} p h^3 \nabla p\right) \nabla W - 6\mu V \nabla \cdot (ph)\, W - 12\mu \frac{\partial}{\partial t} (ph)\, W \right\} d\Omega = 0 \tag{7.6}$$

where σ is the boundary of the domain Ω , and n is the vector pointing outward and normal to the boundary σ.

For the steady state situation, we drop the time dependent term on the left hand side of Eq. 7.6, resulting in

$$\oint_{\sigma} \left(\overline{Q}ph^3\nabla p\right) n\, d\sigma - \int_{\Omega} \left\{\left(\overline{Q}ph^3\nabla p\right)\nabla W + 6\mu V\nabla\left(ph\right)W\right\} d\Omega = 0 \tag{7.7}$$

The boundary conditions consist of only the essential boundary conditions given below, i.e.,

$$p = p_a \quad \text{on the boundary } \sigma$$

The weighting functions can be chosen to be identically zero on the boundary since the pressure is known on the boundary. The line integral of the first term in Eq. (7.7) becomes zero as long as the pressure is specified on the boundary. Then Eq. (7.7) reduces to

$$\int_{\Omega} \left\{\left(\overline{Q}ph^3\nabla p\right)\nabla W + 6\mu V\nabla\left(ph\right)W\right\} d\Omega \;\; = \;\; 0 \tag{7.8}$$

Eq. (7.8) is non-linear in the pressure terms. To obtain a solution, the pressure terms are linearized using a Taylor series expansion. The higher order terms of the series are eliminated by using the following approximation for pressure:

$$p \approx p_0 + dp \tag{7.9}$$

where p_0 is the initial guess for the pressure. The approximation of pressure requires that the change in pressure dp between successive iterations is a small value and that p is close to p_0.

Using a similar Taylor seried expansion, $p\nabla p$ term in Eq. (7.8) is linearized as follows:

$$p\nabla p = (p_0 + dp)\,\nabla\,(p_0 + dp) = p_0\nabla p_0 + p_0\nabla\,(dp) + dp\nabla p_0 + dp\nabla\,(dp) \tag{7.10}$$

The last term in Eq. (7.10) is eliminated since it is negligible compared to the other terms. Using a similar approach, $\nabla(ph)$ can be written as follows:

$$\nabla\,(ph) = \nabla\,[(p_0 + dp)\,h] = p_0\nabla h + h\nabla p_0 + h\nabla\,(dp) + dp\nabla h \tag{7.11}$$

Substiuting Eq. (7.10)-(7.11) in Eq. (7.8), we get:

$$\begin{aligned}\iint_{\Omega} \left\{\overline{Q}h^3(dp\nabla p_0 + p_0\nabla dp)\cdot\nabla W + 6\mu\mathbf{V}\cdot(h\nabla dp + dp\nabla h)W\right\} d\Omega = \\ -\iint_{\Omega} \left\{\overline{Q}h^3 p_0\nabla p_0\cdot\nabla W + 6\mu\mathbf{V}\cdot(h\nabla p_0 + p_0\nabla h)W\right\} d\Omega\end{aligned} \tag{7.12}$$

Eq. (7.12) is arranged such that the right hand side contains terms that are only dependent on the initial guess p_0, which is known from the previous iteration step. The left hand side contains only linear terms of the unknown quantity dp. Iterative numerical methods can be used to solve Eq. (7.12). Then, the pressure p can be updated as $p = p_0 + dp$ and the procedure is repeated till the value of the change in pressure dp between successive iterations reaches a small value defined for the convergence.

Since the boundary is often irregular, the domain should be discretized into smaller components or elements over which a simple function may be defined. The integral over

the entire domain is replaced by a sum of integrations over individual elements in the domain.

The pressure is interpolated over each element in the domain by using shape functions as shown below:

$$p(x, y) = \sum_{i=1}^{N} N_i(x, y) \cdot p_i \tag{7.13}$$

where p_i are the pressure vlaues at the nodes and N_i are the shape functions corresponding to node i.

The elements often have distorted shapes and an isoparametric transformation is used to map these distorted elements as shown in Figure 7.1.

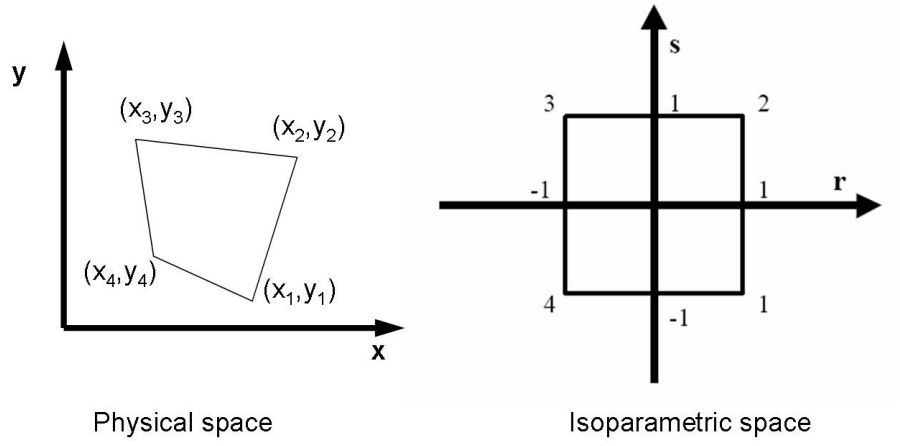

Figure 7.1: Isoparametric transformation

The shape functions are used to interpolate the pressure across the isoparametric

element as follows

$$p(r,s) = \sum_{i=1}^{4} N_i(r,s) \cdot p_i \tag{7.14}$$

Similar interpolation functions are used to transform the physical coordinates to the isoparametric space

$$x(r,s) = \sum_{i=1}^{4} N_i(r,s) \cdot x_i \tag{7.15}$$

$$y(r,s) = \sum_{i=1}^{4} N_i(r,s) \cdot y_i \tag{7.16}$$

where x_i and y_i are the coordinates for node i and the four bilinear shape functions N_i are given as follows:

$$\begin{aligned} N_1(r,s) &= \frac{1}{4}(1-r)(1-s) \\ N_1(r,s) &= \frac{1}{4}(1+r)(1-s) \\ N_1(r,s) &= \frac{1}{4}(1+r)(1+s) \\ N_1(r,s) &= \frac{1}{4}(1-r)(1+s) \end{aligned} \tag{7.17}$$

The numerical solution of the Reynolds equation with this type of approximation needs the derivatives of the interpolation or shape functions. This is given as follows:

$$\begin{aligned} \frac{\partial N_i}{\partial x} &= \frac{\partial N_i}{\partial r}\frac{\partial r}{\partial x} + \frac{\partial N_i}{\partial s}\frac{\partial s}{\partial x} \\ \frac{\partial N_i}{\partial y} &= \frac{\partial N_i}{\partial r}\frac{\partial r}{\partial y} + \frac{\partial N_i}{\partial s}\frac{\partial s}{\partial y} \end{aligned} \tag{7.18}$$

The derivatives of the physical coordinates with respect to the isoparametric coordinates are found using the inverse derivatives. Thus, differentiating Eq. (7.15) and Eq. (7.16) , we get

$$\begin{aligned}
\frac{\partial x}{\partial r} &= \sum_{i=1}^{4} \frac{\partial N_i}{\partial r} x_i \\
\frac{\partial x}{\partial s} &= \sum_{i=1}^{4} \frac{\partial N_i}{\partial s} x_i \\
\frac{\partial y}{\partial r} &= \sum_{i=1}^{4} \frac{\partial N_i}{\partial r} y_i \\
\frac{\partial y}{\partial s} &= \sum_{i=1}^{4} \frac{\partial N_i}{\partial s} y_i
\end{aligned} \tag{7.19}$$

In matrix form, Eq. (7.19) can be written as

$$\begin{Bmatrix} dx \\ dy \end{Bmatrix} = \begin{bmatrix} \sum_{i=1}^{4} \frac{\partial N_i}{\partial r} x_i & \sum_{i=1}^{4} \frac{\partial N_i}{\partial s} x_i \\ \sum_{i=1}^{4} \frac{\partial N_i}{\partial r} y_i & \sum_{i=1}^{4} \frac{\partial N_i}{\partial s} y_i \end{bmatrix} \begin{Bmatrix} dr \\ ds \end{Bmatrix} \tag{7.20}$$

where the matrix on the right hand side of Eq. (7.20) is called the Jacobian matrix.

Multiplying this equation by the inverse of the Jacobian matrix, we get

$$\begin{Bmatrix} dr \\ ds \end{Bmatrix} = \begin{bmatrix} \sum_{i=1}^{4} \frac{\partial N_i}{\partial s} y_i & -\sum_{i=1}^{4} \frac{\partial N_i}{\partial s} x_i \\ -\sum_{i=1}^{4} \frac{\partial N_i}{\partial r} y_i & \sum_{i=1}^{4} \frac{\partial N_i}{\partial r} x_i \end{bmatrix} \begin{Bmatrix} dx \\ dy \end{Bmatrix} \tag{7.21}$$

We can also write the differentials in isoparametric space dr and ds as follows:

$$\begin{Bmatrix} dr \\ ds \end{Bmatrix} = \begin{bmatrix} \frac{\partial r}{\partial x} \frac{\partial r}{\partial y} \\ \frac{\partial s}{\partial x} \frac{\partial s}{\partial y} \end{bmatrix} \begin{Bmatrix} dx \\ dy \end{Bmatrix} \tag{7.22}$$

Comparing Eq. (7.21) and Eq. (7.22), we get

$$\begin{aligned} \frac{\partial r}{\partial x} &= \frac{1}{\det J} \frac{\partial y}{\partial s} \\ \frac{\partial r}{\partial y} &= -\frac{1}{\det J} \frac{\partial x}{\partial s} \\ \frac{\partial s}{\partial x} &= -\frac{1}{\det J} \frac{\partial y}{\partial r} \\ \frac{\partial s}{\partial y} &= \frac{1}{\det J} \frac{\partial x}{\partial r} \end{aligned} \tag{7.23}$$

In matrix form, we can write

$$\begin{Bmatrix} \frac{\partial N_i}{\partial x} \\ \frac{\partial N_i}{\partial y} \end{Bmatrix} = \frac{1}{\det J} \begin{bmatrix} \sum_{k=1}^{4} \frac{\partial N_k}{\partial s} y_k - \sum_{k=1}^{4} \frac{\partial N_k}{\partial r} y_k \\ -\sum_{k=1}^{4} \frac{\partial N_k}{\partial s} x_k \sum_{k=1}^{4} \frac{\partial N_k}{\partial r} x_k \end{bmatrix} \begin{Bmatrix} \frac{\partial N_i}{\partial r} \\ \frac{\partial N_i}{\partial s} \end{Bmatrix} \tag{7.24}$$

where the determinant of the Jacobian matrix is defined as

$$\det J = \left(\sum_{k=1}^{4} \frac{\partial N_k}{\partial r} x_k \right) \left(\sum_{k=1}^{4} \frac{\partial N_k}{\partial s} y_k \right) - \left(\sum_{k=1}^{4} \frac{\partial N_k}{\partial s} x_k \right) \left(\sum_{k=1}^{4} \frac{\partial N_k}{\partial r} y_k \right) \tag{7.25}$$

Thus, we have the quadrilateral element formulation. For the isoparametric transformation used with the residual formulation as shown above, an analytical integration is not possible and a numerical integration scheme is implemented. Gaussian quadrature

method wherein the integration over the element is replaced by summing the function evaluations at the Gauss points is used:

$$\int_{-1}^{1}\int_{-1}^{1} f(r,s)drds = \sum_{m=1}^{N}\sum_{n=1}^{N} f(r_m,s_n)w_m w_n \tag{7.26}$$

where w are weighting functions that depend on the number of Gauss points used. An N-point Gaussian quadrature gives exact results for polynomials up to the order $2N$-1.

For bilinear equations, each element equation consists of four unknown nodal quantities. In matrix form, this is written as

$$\begin{bmatrix} k_{11} & k_{12} & k_{13} & k_{14} \\ k_{21} & k_{22} & k_{23} & k_{24} \\ k_{31} & k_{32} & k_{33} & k_{34} \\ k_{41} & k_{42} & k_{43} & k_{44} \end{bmatrix} \begin{Bmatrix} dp_1 \\ dp_2 \\ dp_3 \\ dp_4 \end{Bmatrix} = \begin{Bmatrix} r_1 \\ r_2 \\ r_3 \\ r_4 \end{Bmatrix} \tag{7.27}$$

In general, for each finite element in the domain, we can write:

$$[K]^e \cdot \{\triangle p\}^e = [R]^e \tag{7.28}$$

where $[K]^e$ is the "element stiffness matrix" and $[R]^e$ is the "force vector".

In Eq. (7.27), the individual quantities of the element stiffness matrix in isoparametric form can be written as

$$k_{ij} = \int_{-1}^{1}\int_{-1}^{1} \left\{ \overline{Q}h^3(\nabla p_0 \cdot \nabla N_i)N_j + \overline{Q}h^3 p_0 \nabla N_j \cdot \nabla N_i \right. \\ \left. +6\mu N_i \left(hV \cdot \nabla N_j + N_j V \cdot \nabla h\right) \right\} \det J \, drds \tag{7.29}$$

The right hand side of Eq. (7.27) can be calculated as follows

$$r_i = -\int_{-1}^{1}\int_{-1}^{1} \left\{ p_0 h^3 \left(\nabla p_0 \cdot \nabla N_i\right) + 6\mu N_i V \cdot \left(p_0 \nabla h + h \nabla p_0\right) \right\} \det J \, drds \tag{7.30}$$

The element stiffness matrix and the force vector can then be assembled for all the elements in the domain to obtain the global stiffness matrix and global force vector, as shown in Eq. (7.31),

$$[K] \cdot \{\triangle p\} = [R] \tag{7.31}$$

where $[K]$ is the "global stiffness matrix".

Eq. (7.31) can be solved for the pressure through successive iterations until the value of dp has reached a value satisfying the convergence criteria.

The mesh of finite elements is created using an automatic mesh generation program (GiD [24]). A typical mesh for a slider air bearing surface is shown in Figure 7.2(a). The mesh can contain up to 50,000 nodes and 100,000 elements. The mesh is much finer or denser near a change in air bearing surface heights. A fine mesh is required to accurately model the steep pressure gradient in these regions.

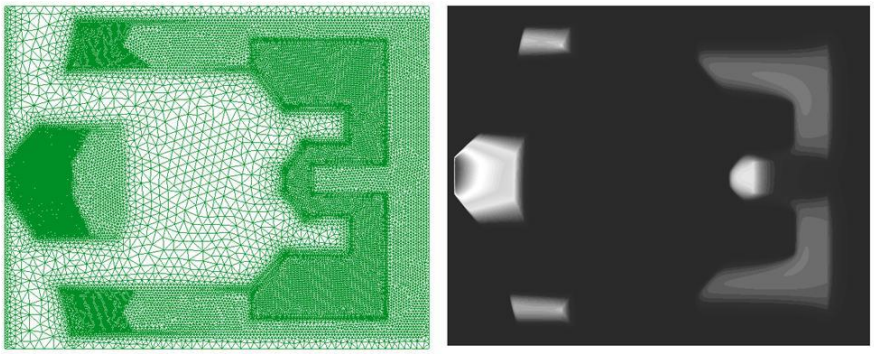

(a) (b)

Figure 7.2: (a) Finite element mesh and (b) pressure distribution for a typical slider in the head disk interface

A typical pressure distribution for a magnetic recording slider is shown in Figure 7.2(b). The largest pressure is at the center trailing edge pad. This region also corresponds to the minimum spacing and is the location of the magnetic read/write element.

The pressure distribution of the air bearing is determined by the geometry of the slider air bearing surface. The air bearing under the slider acts like a spring and has a certain stiffness. A perturbation method is used to determine the stiffness of the air bearing. Applying a small perturbation to the Reynolds equation we obtain an overall stiffness matrix as follows:

$$\begin{bmatrix} k_{zz} & k_{z\alpha} & k_{z\beta} \\ k_{\alpha z} & k_{\alpha\alpha} & k_{\alpha\beta} \\ k_{\beta z} & k_{\beta\alpha} & k_{\beta\beta} \end{bmatrix} = \begin{bmatrix} \int\int \frac{\partial p}{\partial z} dA & \int\int \frac{\partial p}{\partial \alpha} dA & \int\int \frac{\partial p}{\partial \beta} dA \\ \int \frac{\partial p}{\partial z}(x - x_p)\, dA & \int\int \frac{\partial p}{\partial \alpha}(x - x_p)\, dA & \int\int \frac{\partial p}{\partial \beta}(x - x_p)\, dA \\ \int\int \frac{\partial p}{\partial z}(y - y_p)\, dA & \int\int \frac{\partial p}{\partial \alpha}(y - y_p)\, dA & \int\int \frac{\partial p}{\partial \beta}(y - y_p)\, dA \end{bmatrix} \tag{7.32}$$

where k_{ij} represents the air bearing stiffness. The spring stiffness values used in the structural finite element model of the hard disk drive in the operational shock condition are the diagonal elements in Eq. (7.32) for the z-direction (z), the pitch (α), and the roll (β) directions.

7.2 Slider Equilibrium Equations

The pressure distribution for a specific spacing can be found by using the finite element solution of the Reynolds equation as shown in the previous section. However, the spacing between the slider and the disk is generally unknown and is a function of many parameters such as the disk velocity, the slider air bearing design and the radial position of the slider.

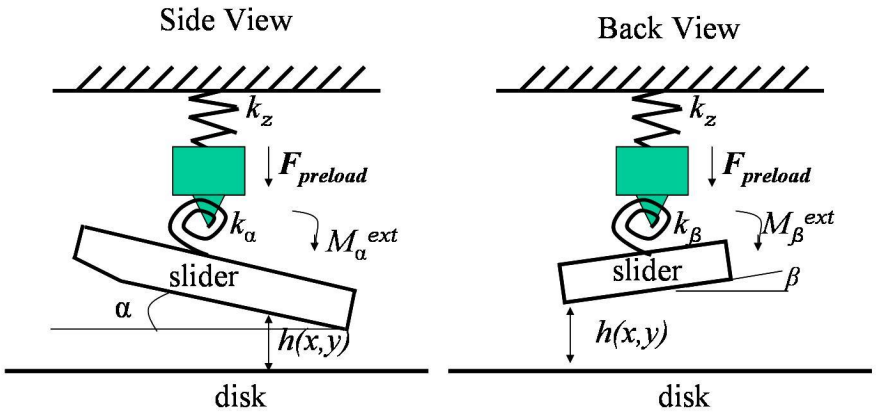

Figure 7.3: Schematic for a pivoted slider bearing

Figure 7.3 shows a schematic of the slider attached to the suspension-gimbal assembly at the pivot point. The three degrees of freedom are in the z-direction, pitch (α) and roll (β) directions. The gimbal or the flexure that carries the slider is attached to the suspension arm. Once the slider achieves its steady flying height over the rotating disk, an equilibrium exists between the suspension preload ($F^{preload}$) and the integrated pressure ($p\left(x,y\right)$) over the slider air bearing surface. From Figure 7.3, the equations of motion for slider equilibrium in the vertical, pitch and roll directions are as follows:

$$\begin{aligned}
\int_A \int \left[p\left(x,y\right)-p_a\right] dA - F^{preload} &= k_z dz \\
\int_A \int \left[p\left(x,y\right)-p_a\right]\left(x-x_p\right) dA - M_\alpha^{ext} &= k_\alpha d\alpha \\
\int_A \int \left[p\left(x,y\right)-p_a\right]\left(y-y_p\right) dA - M_\beta^{ext} &= k_\beta d\beta
\end{aligned} \tag{7.33}$$

where, $F^{preload}$is the suspension preload in the z-direction, M_{α}^{ext} is the external pitch moment applied by the suspension, and M_{β}^{ext} is the external roll moment applied by the suspension. The pressure is denoted by $p\left(x,y\right)$and p_a is the ambient pressure. The pivot point coordinates are denoted by x_p and y_p. The suspension stiffness in the z, pitch and roll directions are represented by k_z, k_{α}, and k_{β} respectively. In addition, dz, $d\alpha$, and $d\beta$ are the vertical and angular differential displacements from the equilibrium position in the z, pitch and roll directions, respectively.

In matrix notation, Eq. (7.33) can be written as follows:

$$\begin{Bmatrix} \int\limits_A \int \left[p\left(x,y\right)-p_a\right] dA - F^{preload} \\ \int\limits_A \int \left[p\left(x,y\right)-p_a\right]\left(x-x_p\right) dA - M_{\alpha}^{ext} \\ \int\limits_A \int \left[p\left(x,y\right)-p_a\right]\left(y-y_p\right) dA - M_{\beta}^{ext} \end{Bmatrix} = \begin{bmatrix} k_z & 0 & 0 \\ 0 & k_{\alpha} & 0 \\ 0 & 0 & k_{\beta} \end{bmatrix} \begin{Bmatrix} dz \\ d\alpha \\ d\beta \end{Bmatrix} \tag{7.34}$$

7.3 Slider Air Bearing Design

7.3.1 Slider Form Factors

The evolution of slider form factors was shown in Chapter 1.5. Since the mid 1990's, so-called "sub-ambient" pressure sliders are commonly used in disk drives. Sub-ambient pressure sliders are designed with a "cavity" in the center of the slider body where the air bearing pressure decreases below sub-ambient pressure due to a sudden increase in

spacing. This cavity acts as a reverse Rayleigh step bearing (see Figure 7.4).

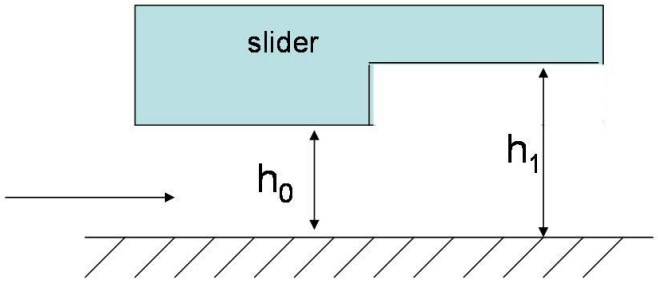

Figure 7.4: Schematic of reverse Rayleigh step bearing

The sub-ambient pressure in the cavity is partially balanced by the positive pressure (above ambient pressure) that is generated on the intermediate and the top surface of the air bearing (see Figure 7.5). Current hard disk drives use the "pico" or "femto" slider form factors. Figure 7.5(a) and (b) show the pico and femto slider designs, respectively.

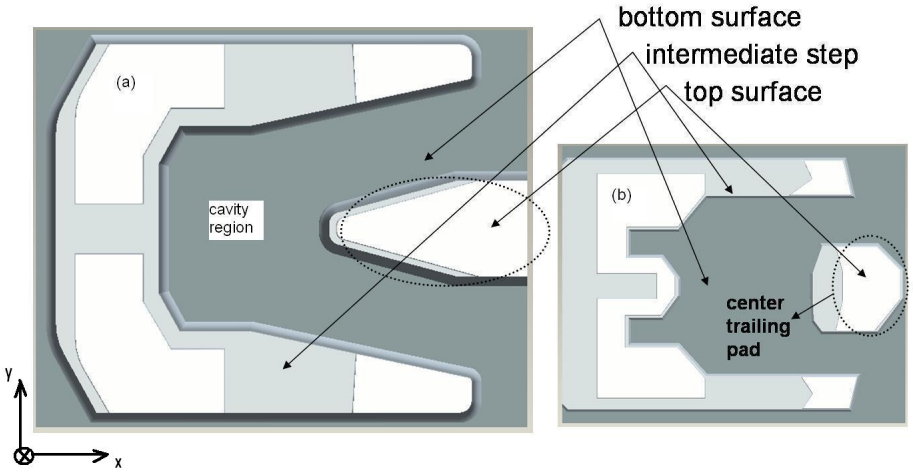

Figure 7.5: Slider form factors: (a) pico and (b) femto

7.3.2 Slider Design and Finite Element Mesh Generation

Slider geometry can be modeled using any computer aided design (CAD) programs. Some of the commercially available CAD programs are ProEngineer, Solidworks, AutoCAD, Solid Edge, etc. In this thesis, ProEngineer and Solidworks were used to create the 3-D geometry of the slider. By convention, the air bearing surface of the slider is in the x-y plane and the air bearing steps are in the z-direction. The origin of the slider design is chosen such that any vertex of the slider body in the x, y or the z-direction have positive coordinates.

Figure 7.5(a) shows the air bearing surface for a pico slider design. For this slider, the intermediate surface is extruded in the direction that is out of plane of the paper from the cavity region by a distance of 2.5 μm. The top surface is extruded from the intermediate air bearing surface by a distance of 260 nm. The transition between one air bearing step to the next air bearing step is critical in air bearing design. These transition walls are not vertical in reality since the slider is manufactured by etching techniques. Etched sliders usually have curved or angled transition walls between air bearing steps. In the slider model, “spline”, “round”, or “chamfer” design tools are used in ProEngineer to simulate the etched transition shape.

The next step in the air bearing simulation is the mesh generation. The quality of the mesh in a finite element analysis determines the accuracy of the solution. The air bearing simulator uses bilinear quadrilateral and triangular shell elements in the finite element analysis. Quadrilateral elements are used in the areas of the air bearing surface where

the geometry is smooth and not complicated. However, in areas such as the air bearing steps and complicated geometry, triangular elements are used in order to conform to the true geometric shape of the slider bearing. The mesh generation is achieved using a mesh generation program (GiD). The mesh generated using GiD for the slider air bearing shown in Figure 7.5(a) is shown in Figure 7.6. The mesh contains 31398 nodes and 62442 elements for the air bearing surface. From Figure 7.6 we observe that the model contains a fine mesh on the center trailing pad and the air bearing step regions. Since the slider has a pitch, the center trailing pad is the region of closest proximity to the disk and also the region of the highest air bearing pressure.

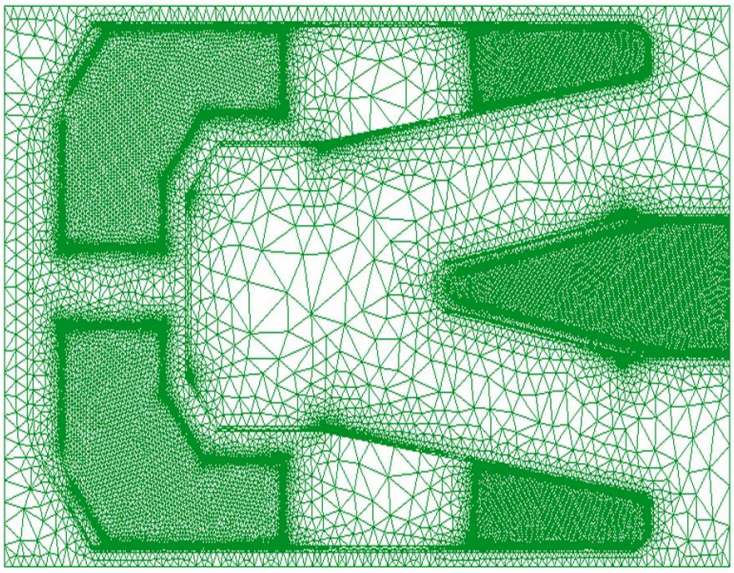

Figure 7.6: Finite element mesh for pico slider design

Finite element analysis of the steady state Reynolds equation is used to calculate the equillibrium position and the air bearing pressure distribution. Figure 7.7 shows the

pressure distribution for the slider shown in Figure 7.5(a)

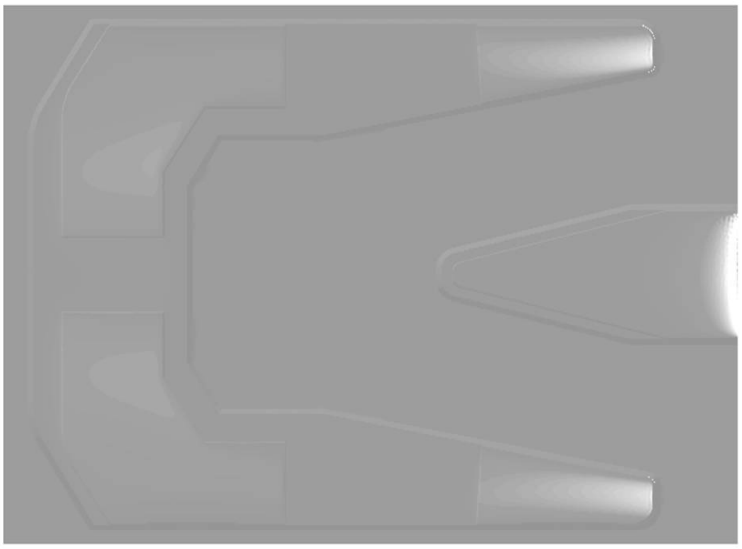

Figure 7.7: Pressure distribution for the pico slider design

Figure 7.8 shows the flying height as a function of the disk speed for pico slider design shown in Figure 7.5(a). This slider is designed to fly at 4 nm over the middle diameter of a 2.5 inch (63 mm) diameter disk at a rotational speed of 7200 rpm. Figure 7.8 shows that the minimum spacing is a weak function of disk velocity. ID, MD and OD represent the inner, middle and outer diameter of the disk, respectively.

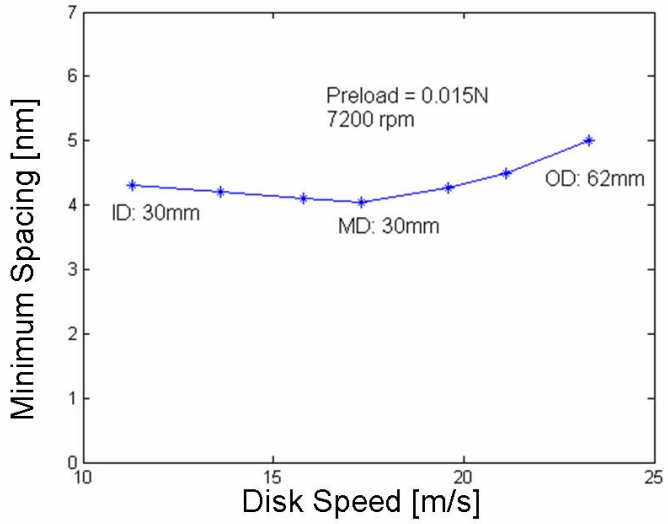

Figure 7.8: Flying height as a function of disk speed for pico slider design

Figure 7.9 shows the flying height as a function of the disk radius for the femto slider design shown in Figure 7.5(b). This slider is designed to fly over a 1 inch (25 mm) diameter disk at a rotational speed of 3600 rpm. Figure 7.9 shows that the minimum spacing is lower at the inner diameter of the disk compared to the outer diameter of the disk.

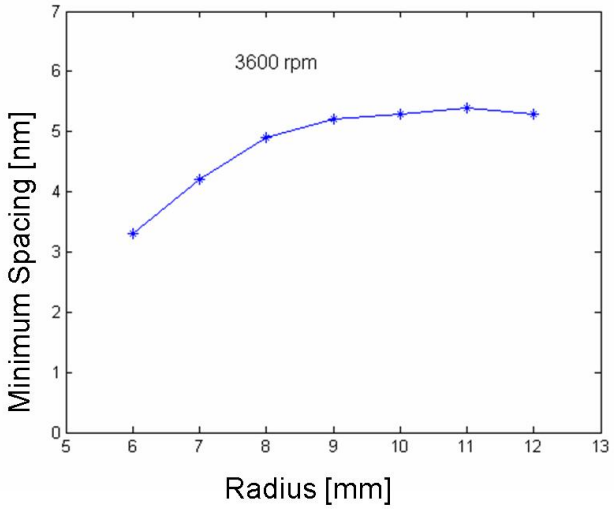

Figure 7.9: Flying height as a function of disk radius for femto slider design

7.4 Finite Element Solution of the Time Dependent Reynolds Equation

In addition to the space domain, the time domain must also be taken into account in seeking a finite element solution of the time-dependent Reynolds equation. Using a similar procedure as before, we now have to discretize the pressure in the x, y space as well as in the time domain.

$$p(x, y, t) = \sum_{i=1}^{N} N_i(x, y) \cdot p_i(t) \tag{7.35}$$

In this formulation we note that the pressure at the nodes is a function of time and the

shape function are functions of x and y. An equation of this form can be solved using the separation of variables approach. In the solution of the time-dependent Reynolds equation, it is convenient to introduce a new variable as follows:

$$\Theta = ph \tag{7.36}$$

In areas where the spacing is small, the pressure is high and in areas where the spacing is large, the pressure is low. Therefore, introducing the new variable as in Eq. (7.36) causes a "smoothing" effect and allows for better convergence. The dimensional time-dependent Reynolds equation can be written as:

$$\frac{\partial \Theta}{\partial t} \cdot \int_{\Omega} 12\mu W N d\Omega + \int_{\Omega} \left\{ \nabla W \cdot \left[\overline{Q}\left(\Theta\right) \left(h\Theta\nabla\Theta - \Theta^2 \nabla h \right) \right] - 6\mu V \Theta W \right\} d\Omega = 0 \tag{7.37}$$

Similar to the steady state Reynolds equation, the Galerkin weighted residual finite element method is used for the solution of the time-dependent Reynolds equation. Weissner et al. developed the "dynamic load/unload simualtor" for slider air bearings at the Center for Magnetic Recording Research (CMRR) based on the Galerkin weighted residual formualtion. The details of the numerical methods used in this approach is given in Appendix B.

The finite element solution for the time-dependent Reynolds equation obtained in Appendix B was used to study the dynamic response of sliders to a disk step response and also to external shock loads.

7.4.1 Slider Response to Step on the Disk

The transient flying behavior of a slider was simulated by a numerically generated step on the disk. A cosine shaped disk bump with a profile given by Eq. (7.38) was aligned with the center line of the slider along the slider length.

$$h_{step} = \frac{\mathrm{A}}{2}\left(1 + \cos\frac{\pi d}{\lambda}\right) \tag{7.38}$$

In Eq. (7.38), A is the height of the disk step (4-6 nm), d is the diameter of the disk step (0.1-0.25 mm), and λ is the wavelength of the disk step (0.4-0.5 mm).

A typical result for the disk step response is shown in Figure 7.10. Figure 7.10 shows the minimum sapcing, pitch and roll for the pico slider as a function of time. From Figure 7.10(a) we observe that the slider with a design flying height of 4 nm flies over a disk step and the flying height drops down to about 1.9 nm. The slider regains the nominal flying height as it crosses the disk step and the slider vibration dampens out within a few milliseconds. From Figure 7.10(b) and 7.10(c) we observe a similar change in the pitch and roll motion of the slider, respectively.

The details of the slider flying characteristics and the difference between textured and untextured sliders will be explained in the next chapter.

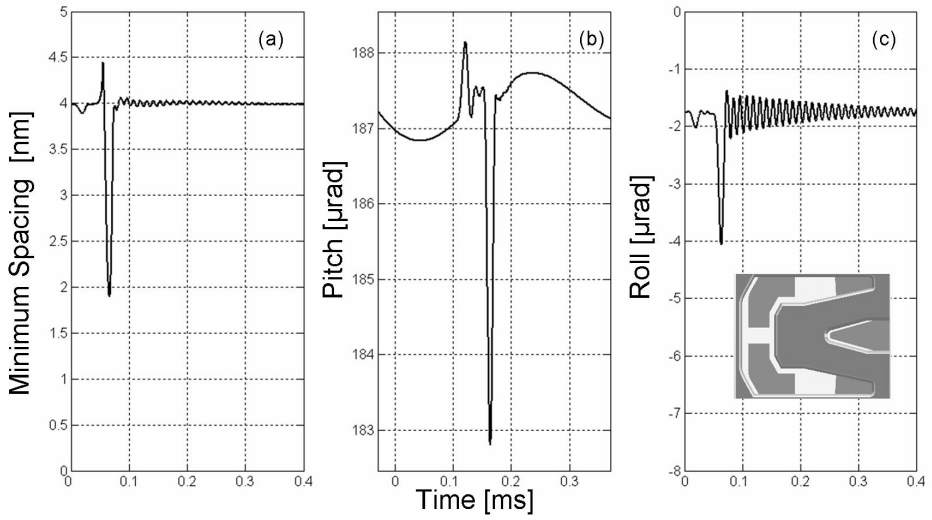

Figure 7.10: (a) Minimum spacing, (b) pitch and (c) roll motion of the slider flying over a disk step

7.4.2 Slider Response to Operational Shock

As explained in Chapter 2, a finite element structural model of a hard disk drive was developed to simulate operational shock response. To get the air bearing response to operational shock, we decouple the equation as follows. The stiffness of the air bearing used in the structural model was obtained from the finite element solution of the steady state Reynolds equation. The steady state solution was used to determine the slider equilibrium position. The stiffness matrix as given in Eq. (7.32) is used in the finite element structural model of the head gimbal assembly. The primary stiffness values used in the finite element structural model are the diagonal elements of Eq. (7.32). These diagonal elements represent the z-direction, pitch and roll direction stifness values, respectively.

The structural model was used to determine the structural response of the hard disk drive for the operational state. The time dependent values of the normal force, pitch and roll moments on the slider are determined from the numerical solution of the finite element structural model. The external force and moments for the shock load that are time dependent quantities, must be computed and taken into account in the solution of the Reynolds equation. This creates an additional load due to shock that results in a change in the air bearing load. This change in air bearing load results in a change in the slider flying height, pitch and roll characteristics.

In the next step, a finite element solution of the time-dependent Reynolds equation was used to determine the slider response to an external shock load. At each time step, the shock load is applied to the slider by adding the external force and moments to the air bearing load obtained form the finite element analysis of the structure.

Figure 7.11 shows typical results for the change in slider minimum spacing, pitch and roll for an operational shock simulation of 50 G for 2 ms. From Figure 7.11 we observe that the slider attains a steady nominal flying height of 11 nm and an external shock of 50 G amplitude and 2 ms pulse width is applied. The minimum spacing of the slider reduces to about 6 nm due to the shock event and the slider vibration dampens out in time. If the shock amplitude is large, there is a possibility of the air bearing to break and the slider contact or slap onto the disk creating unstable head disk interface due to shock.

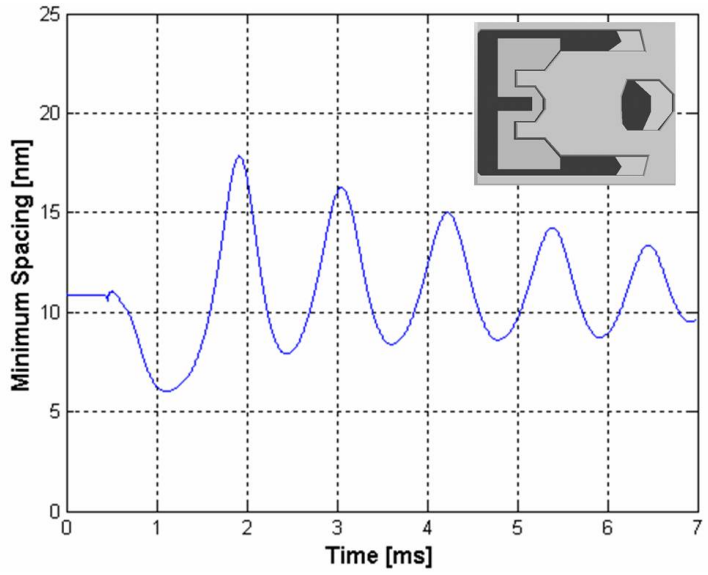

Figure 7.11: Minimum spacing, pitch and roll of femto slider subjected to operational shock of 50G - 2 ms

The slider response to a disk step and an external shock is used in the next chapter to determine the effect of texture on the slider flying characteristics.

Bibliography

[1] A. Hrennikoff, " Solution of problems of elasticity by the frame-work method," *ASME Journal of Applied Mechanics*, vol. 8, 1941, A619-A715

[2] R. Courant, "Variational Methods for the Solution of Problems of Equilibrium and Vibration", *Bull. Am. Math. Soc.*, Vol. 49., 1943, pp. 1-23

[3] O. Reynolds, "On the Theory of Lubrication and its Application to Mr. Beauchamp Tower's Experiments Including an Experimental Determination of the Viscosity of Olive Oil", Philosophical Transactions of the Royal Society London, Series A, vol. 177, pp 157-234, 1886

[4] W. A. Gross, "Gas Film Lubrication", *John Wiley & Sons*, 1962

[5] D. Dowson, "Hydrodynamic Lubrication: Bearings and Thrust Bearings", *Elsevier*, 1997

[6] C. Cercignani, "Rarefied Gas Dynamics", *Cambridge University Press, First Edition*, 2000

[7] J. Argyris, "Energy Theorems and Structural Analysis", *Butterworths Scientific Publications*, 1960

[8] M. Turner, R. W. Clough, H. C.Martin and L. J. Topp, "Stiffness and Deflection Analysis of Complex Structures", *Journal of Aeronautical Science* 23 (9), pp. 805-823, 1956

[9] E. L. Wilson, and R. W. Clough, "Dynamic Response by Step-by-Step Matrix Analysis", *Proc. Symp. On Use of Computers in Civil Engineering*, Lisbon, Portugal, 1962

[10] R. W. Clough, E. L. Wilson, "Early Finite Element Research at Berkeley", *Fifth U.S. National Conference on Computational Mechanics*, Aug. 4-6, 1999

[11] G. Strang and G. Fix, " An Analysis of the Finite Element Method", 1973

[12] Albert Burgdorfer, “The Influence of the Molecular Mean Free Path on the Performance of Hydrodynamic Gas Lubricated Bearings”, *Transactions of the ASME*, Series D, vol. 81, pp. 94-100, 1959

[13] Y. Hsia, G. Domoto, “An Experimental Investigation of Molecular Rarefaction Effects in Gas Lubricated Bearings at Ultra-Low Clearances”, *Transactions of the ASME, Journal of Lubrication Technology*, vol. 105, pp. 120-130, 1983

[14] S. Fukui and R. Kaneko, “Analysis of Ultra-Thin Gas Film Lubrication Based on Linearized Boltzmann Equation: First Report - Derivation of a Generalized Lubrication Equation Including Thermal Creep Flow”, *Transactions of the ASME, Journal of Tribology*, Vol. 110, 1988, pp. 253-262

[15] S. Fukui and R. Kaneko, “A Database for Interpolation of Poiseuille Flow Rates for High Knudsen Number Lubrication Problems”, *IEEE Transactions on Magnetics,* 24 (6), pp. 2751-2753, 1988

[16] S. Fukui and R. Kaneko, “Analysis of Flying Characteristics of Magnetic Heads with Ultra-Thin Spacings Based on the Boltzmann Equation”, *Transactions of the ASME, Journal of Tribology*, Vol. 112, 1990, pp. 78-83

[17] Wahl, M., Lee, P., and Talke, F, “An Efficient Finite Element-Based Air Bearing Simulator for Pivoted Slider Bearings Using Bi-Conjugate Gradient Algorithms” , *Tribology Transactions*, Vol.39 (no. 1): 130-138, 1996

[18] Baugh, E. Weissner, S. Talke, F.E., ”Biquadratic Models for Slider Airbearing Surfaces”, *IEEE Transactions on Magnetics*, Vol.34 (no. 4): 1816-1818, 1998

[19] Weissner, S., Zander, U., and Talke, F.E., “A New Finite-Element Based Suspension Model Including Displacement Limiters for Load/Unload Simulations” *Transactions of the ASME*, Vol.125 (no. 1): 162-167, 2003

[20] Jayson, E. M., Murphy, J. Smith, P. W. Talke, F.E., “Effects of Air Bearing Stiffness on a Hard Disk Drive Subject to Shock and Vibration”, *Journal of Tribology*, Vol.125 (no.): 343-249, 2003

[21] Huang, W., Bogy, D., “ The Effect of Accomodation Coefficient on Slider Air Bearing Simulation”, *ASME Journal of Tribology*, 122: 427-435, 2000

[22] C. Pozrikidis, “Numerical Computation in Science and Engineering”, *Oxford University Press*, 1998

[23] Thomas J. R. Hughes, “The Finite Element Method: Linear, Static and Dynamic Finite Element Analysis”, Prentice-Hall, 1987

[24] GiD, *Users Manual*

8

Analysis of Surface Textured Air Bearing Sliders with Rarefaction Effects

8.1 Overview

To improve the tribological performance of a sliding interface, surface texturing has been used in a number of applications such as mechanical seals, piston rings, thrust bearings and the head/disk interface in hard disk drives. Etsion et al. [1] studied the effect of texture on mechanical seal surfaces. They found that texturing improved the friction and wear properties of the seal interface and increased the load carrying capacity. Kligerman et al. [2] investigated the effect of texture design parameters on piston

rings. They determined optimum values of texture depth and density for which a minimum in the friction force occurred. Brizmer et al. [3] performed a similar analysis for parallel thrust bearings and compared the performance of textured parallel thrust bearings with that of inclined slider bearings and stepped slider bearings. The authors concluded that loads comparable to those of inclined and stepped slider bearings can be generated in parallel thrust bearings using micro-texturing. Kligerman and Etsion [4] studied the pressure generation of textured gas seals using a finite element solution of the compressible Reynolds equation. In all of the above investigations, laser surface texturing was used to create uniformly distributed indentations, i.e., texture features with spherical shape. Laser texturing has also been used in hard disk drives to reduce stiction. Knigge et al. [5] and Khurshudov et al. [6] investigated the effect of texturing the disk surface to reduce stiction during contact start stop (CSS). Hu and Bogy [7] investigated the effect of laser texturing on the effect of pressure generation of sub-ambient pressure sliders. Zhou et al. [8] and Su et al. [9] studied the effect of slider texturing by ion beam etching on stiction and friction during contact start stop. Gui et al. [10] and L. -J. Fu et al. [11] studied the effect of "padded" sliders. They found that the stiction and friction behavior improved for padded sliders on smooth disks. In this study, we investigate numerically the effect of texture on the flying characteristics of magnetic recording sliders. The objective in this study is to determine the effect of texture design on the pressure generation in the regions of the slider where the flying height is smallest. To generate detailed pressure curves as a function of the texture design dimensions and optimize the

flying characteristics of a typical magnetic recording slider (Figure 1(a)), a large numerical effort is required. In order to start the analysis with texture design parameters that are likely to be near the optimum texture design, we first investigate a simplified model consisting of an infinitely wide plane slider with one row of texture features. In this part of the study, we use an approach similar to Kligerman et al. [4] but include the Boltzmann slip correction (Fukui and Kaneko, [12]) for rarefied gas flow. We numerically study the effect of texture starting with a single row of uniformly distributed spherical indentations and evaluate the effect of texture diameter, depth, and density (ratio of the textured area to the total area) on the average pressure. The study of the fundamental case of one row of texture gives insight into the effect of pressure generation and allows us to find the most desirable texture geometry. In the second part of the study, we investigate the effect of pitch on the "single-row-of-texture" model and compare the results to a plane inclined untextured slider bearing. In the last part of the study, we use the optimum texture parameters (diameter, depth, density) obtained from the "single-row-of-texture" model and investigate the steady state and transient flying characteristics of a textured actual air bearing slider. The simulation results show that textured sliders exhibit reduced flying height modulation and better damping characteristics compared to untextured sliders.

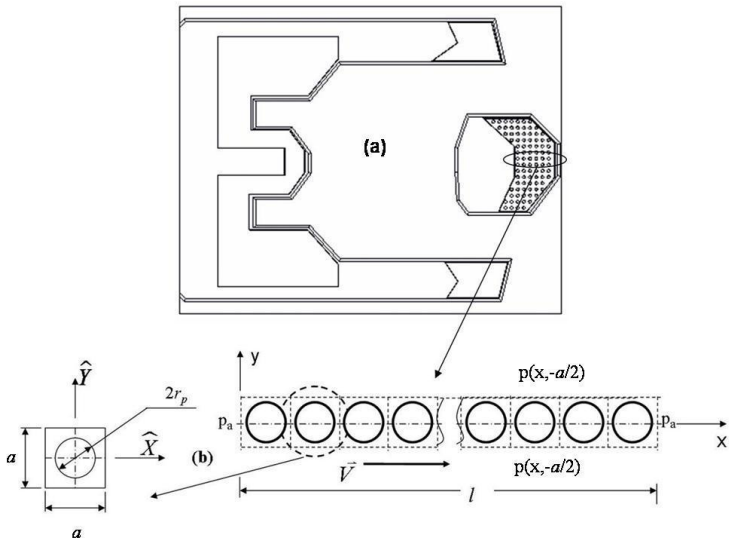

Figure 8.1: (a) Air bearing surface of slider with texture, (b) one row of texture with boundary conditions and definition of single texture cell

Figure 8.1(a) shows a typical magnetic recording slider with texture applied at the center trailing pad of the slider. Figure 8.1(b) indicates a single row of spherical indentations from the trailing pad of the slider shown in Figure 8.1(a). In Figure8.1(b), each of the indentations is defined over a square cell of side length 'a'. The radius of each spherical indentation is denoted by r_p and the indentation is centered in the imaginary square cell. The density S_p of the texture is defined as the ratio of the area covered by the indentation to the area of the indentation cell, i.e. .

In Figure 8.1(b) the pressure is ambient at the beginning and the end of a row of

indentations, i.e.,

$$p\left(x=0,y\right)=p\left(x=l,y\right)=p_a \tag{8.1}$$

If we assume that the bearing is infinitely wide in the y-direction, the pressure is periodic from row to row. In this case, periodicity conditions can be applied between adjacent rows, i.e.,

$$p\left(x,\, i\frac{a}{2}\right)=p\left(x,\, i\frac{-a}{2}\right) \tag{8.2}$$

where $i=1,2,3,.....n$ is the row number.

For very small spacing, the steady state compressible Reynolds equation with rarefaction effect is given by:

$$\frac{\partial}{\partial x}\left(Q\left(Kn\right)ph^3\frac{\partial p}{\partial x}\right)+\frac{\partial}{\partial y}\left(Q\left(Kn\right)ph^3\frac{\partial p}{\partial y}\right)=6\mu\overrightarrow{V}\frac{\partial\left(ph\right)}{\partial x} \tag{8.3}$$

where x and y are the coordinates in the length and width directions, respectively; p is the pressure; h is the spacing; $\overrightarrow{V}$ is the velocity of the moving surface; μ is the viscosity, and $Q(Kn)$ is the rarefaction term for slip flow correction. The term $Q(Kn)$ is based on the ratio of the flow rate for Poiseuille flow to the continuum flow rate (Fukui and Kaneko, [(12)], see Chapter 6).

In Figure 8.2, a cross section through a row of indentations is shown for the case that the slider is parallel to the moving disk surface. In Figure8.2, the clearance is denoted

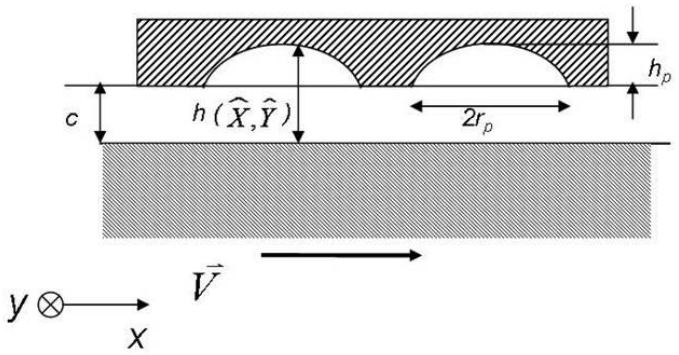

Figure 8.2: Schematic for film thickness and geometry of indentations

by c. In addition, $h\left(\widehat{X},\widehat{Y}\right)$ is the local film thickness, and h_p is the depth of an individual spherical indentation. For a single indentation, the following non-dimensional definitions are introduced:

$$\overline{X}=\frac{\widehat{X}}{r_p};\ \overline{Y}=\frac{\widehat{Y}}{r_p};\ H\left(\overline{X},\overline{Y}\right)=\frac{h\left(\widehat{X},\widehat{Y}\right)}{c} \tag{8.4}$$

Using Eq. 8.4, it was shown by Kligerman and Etsion, [4] that the local non-dimensional film thickness is given by:

$$H\left(\overline{X},\overline{Y}\right)=\begin{cases}1+\sqrt{\left(\dfrac{\varepsilon}{2\delta}+\dfrac{1}{8\varepsilon\delta}\right)^2-\left(\overline{X}^2+\overline{Y}^2\right)\dfrac{1}{4\delta^2}}-\left(\dfrac{1}{8\varepsilon\delta}-\dfrac{\varepsilon}{2\delta}\right) & \\ \qquad\qquad\qquad\qquad\qquad\qquad \text{for}\left(\overline{X}^2+\overline{Y}^2<1\right) & \\ 1 \qquad\qquad\qquad\qquad \text{for}\left(\overline{X}^2+\overline{Y}^2>1\right)\end{cases} \tag{8.5}$$

where ε is the aspect ratio of the indentation and δ is the non-dimensional clearance.

For a row of indentations, the film thickness (Eq. 8.5) is repeated for each individual indentation cell and the non-dimensional parameters for the entire row are as follows:

$$X = \frac{x}{l};\; Y = \frac{y}{l};\; H\left(X,Y\right) = \frac{\left(x,y\right)}{c};\; P = \frac{p}{p_a} \tag{8.6}$$

Using the non-dimensional quantities given by Eq. 8.6, we obtain the non-dimensional Reynolds equation for a row of indentations as:

$$\frac{\partial}{\partial X}\left(Q\left(Kn\right)^3\frac{\partial P}{\partial X}\right) + \frac{\partial}{\partial Y}\left(Q\left(Kn\right)PH^3\frac{\partial P}{\partial Y}\right) = \frac{\lambda}{\delta^2}\frac{\partial\left(PH\right)}{\partial X} \tag{8.7}$$

where $\lambda = 3\mu\overrightarrow{V}l/2r_p^2p_a$ is the non-dimensional bearing parameter, $\delta = c/2r_p$is the non-dimensional clearance, and $\Lambda = \lambda/\delta^2$ is the bearing number. Eq. (8.7) was solved numerically using a staggered grid approach (Lacey and Talke [13]) for the pressure P and film thickness H.

8.2 Numerical Results for One Row of Texture

Figure 8.3(a) shows the pressure distribution for a single indentation. We observe that the pressure decreases at the diverging region (A) of the indentation and then increases gradually towards the converging region (B) of the indentation in the direction of flow with the maximum pressure at the converging edge of the indentation (B). The average pressure for a single cell with one indentation was found to be 6 to 8 % above ambient pressure. The pressure profile at the sides of an indentation cell (i.e., at $(x, y = \pm\, a/2)$) is identical due to the assumption of periodic boundary conditions.

To study the effect of texture size, density, and position of texture, we have per-

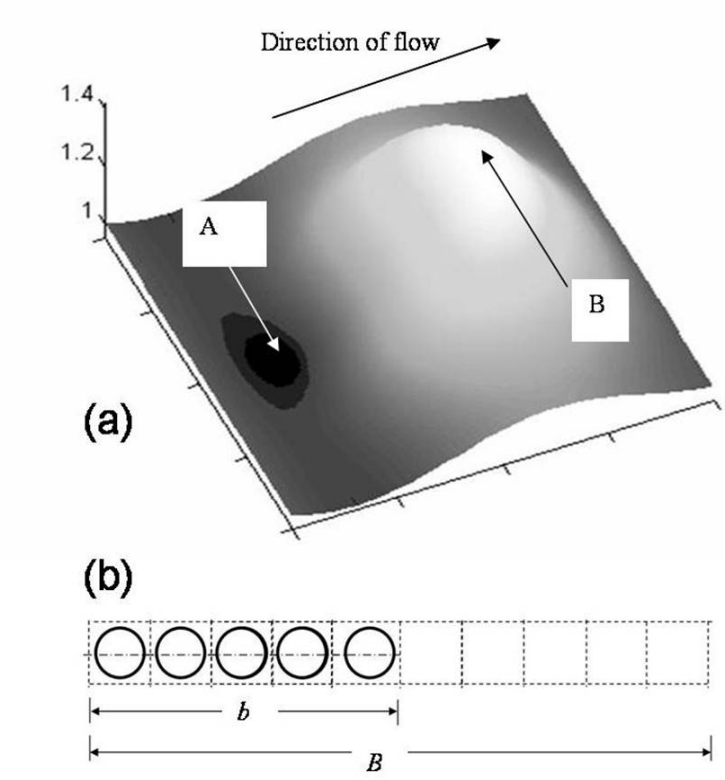

Figure 8.3: Pressure distribution for one indentation

formed a parametric analysis for one row of indentations. The non-dimensional texture parameters used in the study are a) S_p= texture area density (ratio of area of textured surface to total area of surface), b) ε = texture aspect ratio (ratio of the depth of the indentation to the diameter of the indentation), and c) γ = ratio of the length of the textured portion of a row to the total length of the row (Figure 8.3(b)). As is shown in Figure 8.3(b), the texture portion parameter $\gamma = b/B$. For full texture, $\gamma = 1$.

In this study, the texture density S_p was chosen to lie between 0.1 and 0.6, ε was chosen to be between 0.0025 and 0.025, and δ was chosen between 0.0002 and 0.004. The values of the parameter λ were chosen to be less than 0.035 based on the actual values of the viscosity, the disk velocity and the ambient pressure for air bearings, resulting in a bearing number Λ between 1000 and 67500. The parameter γ was chosen between 0.1 and 1.

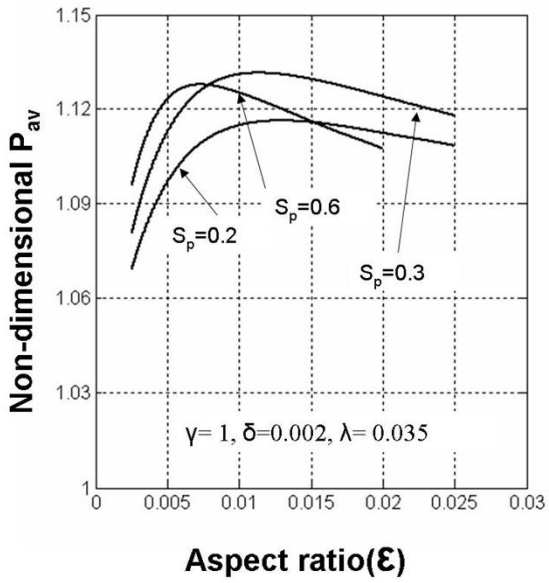

Figure 8.4: Non-dimensional average pressure vs. texture aspect ratio (ε) for full surface texturing

Figure 8.4 shows the non-dimensional average pressure as a function of the non-dimensional aspect ratio (ε) for texture densities S_p of 0.2, 0.3, and 0.6, respectively. For the data shown in Figure 4, $\gamma = 1$, corresponding to one indentation in each cell. We observe that the average pressure increases initially with ε, reaches a maximum value, and then decreases gradually as the aspect ratio ε increases. The aspect ratio at which the average pressure reaches a maximum is a function of the texture density (S_p). We note that the aspect ratio, at which the average pressure reaches its maximum, shifts to the left for increasing texture density. We also observe from Figure 8.4 that the maximum value of the non-dimensional average pressure varies only slightly if the area

density ratio S_p is changed from 0.2 to 0.6.

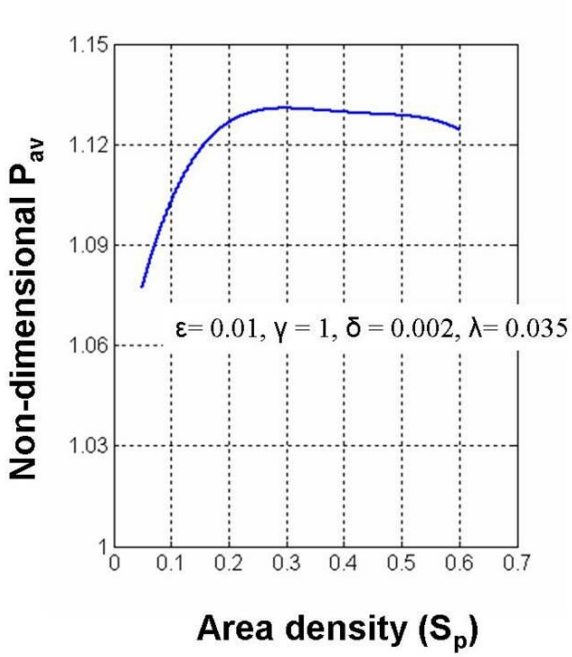

Figure 8.5: Non-dimensional average pressure vs. texture area density (S_p) and full surface texture

Figure 8.5 shows the non-dimensional average pressure as a function of the texture area density for an aspect ratio ε = 0.01 and a texture portion parameter $\gamma = 1$. We observe that the curve is nearly flat in the range from 0.2<S_p<0.6. For an area density S_p >0.6, the indentation geometry of one cell overlaps the neighboring indentation geometry. Therefore, only texture densities S_p < 0.6 are evaluated.

In the next part of the investigation, we studied the effect of partial texturing. Figure 8.6(a) shows the non-dimensional average pressure as a function of the texture portion parameter γ. A texture aspect ratio ε = 0.01 and texture area densities S_p = 0.3 and

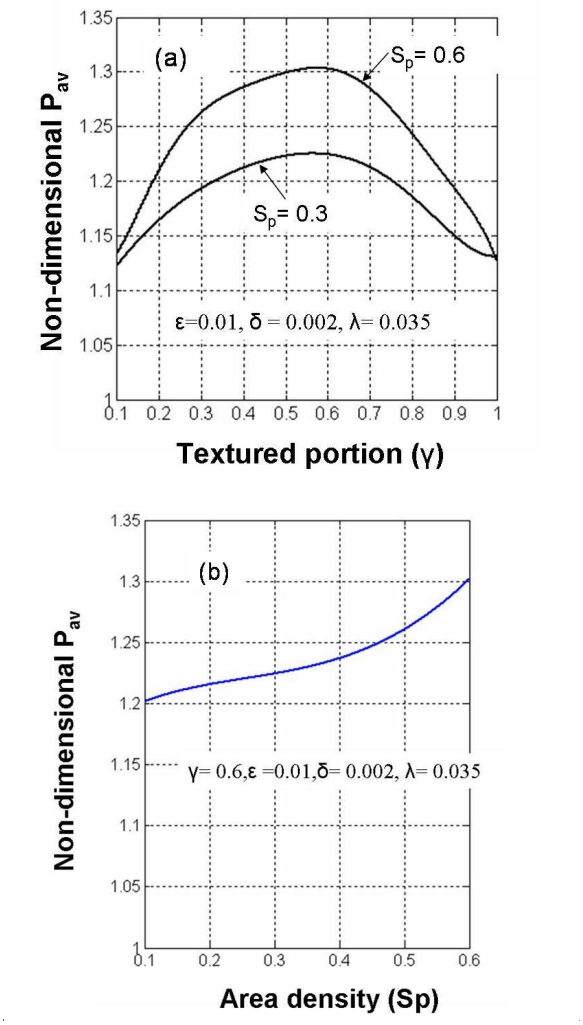

Figure 8.6: Non-dimensional average pressure vs. (a) texture portion parameter (γ) for two S_p values, and (b) vs. texture area density (S_p) for γ = 0.6

0.6, respectively, were selected for the data shown in Figure 8.6(a). From Figure 8.6(a), we observe that an optimum exists for the non-dimensional average pressure near γ = 0.6. The optimum non-dimensional average pressure for full surface texture (γ = 1) was observed for a texture area density of Sp = 0.3 (Figure 8.5). If the average pressure is plotted as a function of texture density S_p for partial surface texture, we observe that the texture density S_p does not have an optimum, i.e., the non-dimensional average pressure increases with increasing texture density. This is shown in Figure 8.6(b) where the non-dimensional average pressure is plotted against the texture density S_p for the optimum texture portion parameter γ = 0.6 and an aspect ratio ε = 0.01.

In order to determine the effect of texture aspect ratio (ε) for partial surface texture, we have studied the non-dimensional average pressure for varying aspect ratios. Figure 8.7 shows the non-dimensional average pressure as a function of the texture aspect ratio ε, with the optimum texture portion parameter, γ = 0.6. Figure 8.7 shows that the optimum aspect ratios are indeed similar to full texture as indicated in Figure 8.4, i.e., for an area density, S_p = 0.3, the optimum aspect ratio is ε = 0.01 and for an area density, Sp = 0.6, the optimum aspect ratio is ε = 0.0075. From the numerical results shown above we note that the optimum texture parameters for full texturing are approximately as follows: area density S_p = 0.3; aspect ratio ε = 0.01. In the case of partial texturing, the optimum texture parameters are: area density S_p = 0.6 (or highest possible); aspect ratio ε = 0.0075, and texture portion parameter γ = 0.6.

Figure 8.8 shows the non-dimensional pressure for optimum full surface texture pa-

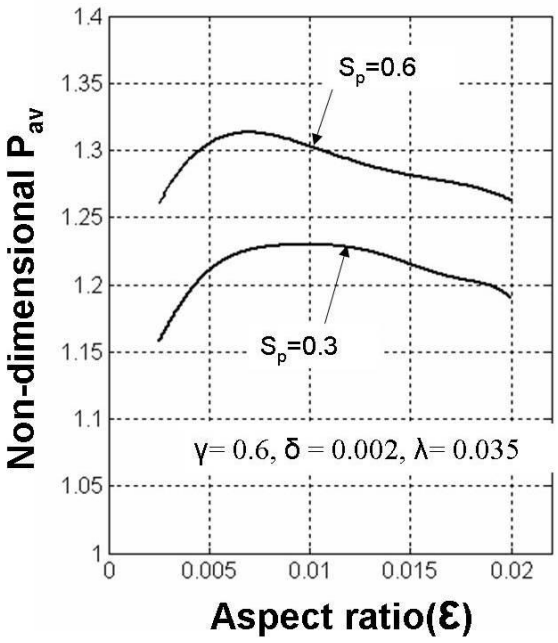

Figure 8.7: Non-dimensional average pressure vs. texture aspect ratio (ε) for partial surface texture

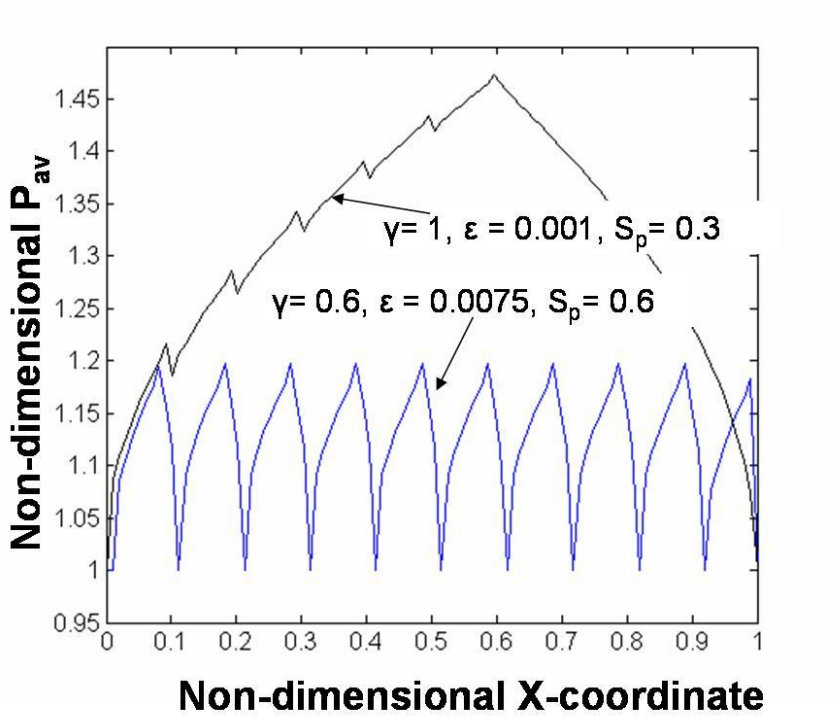

Figure 8.8: Non-dimensional pressure distribution across the centerline of the row of indentations in the x-direction for full and partial surface texture

rameters (S_p = 0.3, ε = 0.01, and γ = 1) along the centerline of a single row of indentations in the x-direction. Figure 8.8 also shows the non-dimensional pressure for optimum partial surface texture parameters (S_p = 0.6, ε = 0.0075, and γ = 0.6) along the centerline of the row of indentations in the x-direction. From Figure 8.8 (full surface texture), we observe that the pressure profile for full surface texture is periodic for each indentation in the x-direction and that the local pressure of an indentation is not affected by the neighboring indentations. However, the pressure profile for partial surface texture increases gradually from the first indentation to the last indentation and the maximum pressure occurs along the last indentation corresponding to γ = 0.6. This non-uniform pressure profile is due to the influence of each indentation on its neighboring indentation. The net effect is that the amplitude of the average pressure increases for partial texturing compared to the case of full texturing.

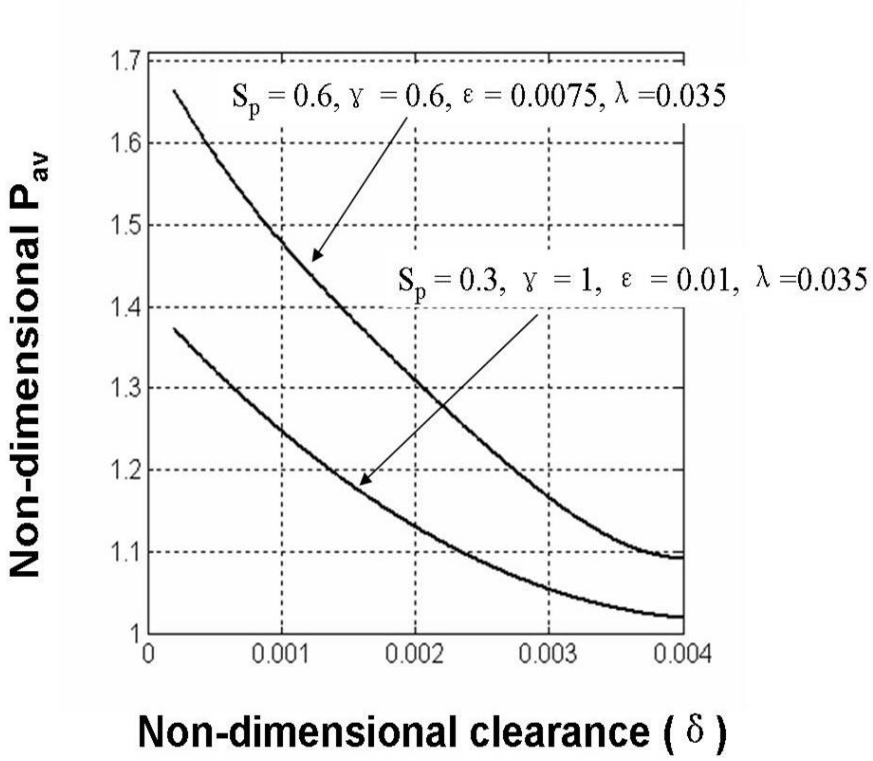

Figure 8.9: Non-dimensional average pressure as a function of the non-dimensional clearance (δ) for optimum full surface texture and partial texture parameters

Figure 8.9 shows the non-dimensional average pressure as a function of the non-dimensional clearance ($\delta = c/2r_p$) for optimum full surface texture and partial texture parameters. The actual clearance values used in the numerical calculation are in the range from 1 nm to 20 nm. From Figure 8.9, we observe that the non-dimensional average pressure increases as the clearance decreases for both full surface texture and partial surface texture. For δ>0.003, we observe that the non-dimensional average pressure is nearly constant, only slightly above ambient pressure. However, for δ values less than 0.003, we observe that the effect of δ on the non-dimensional average pressure is sig-

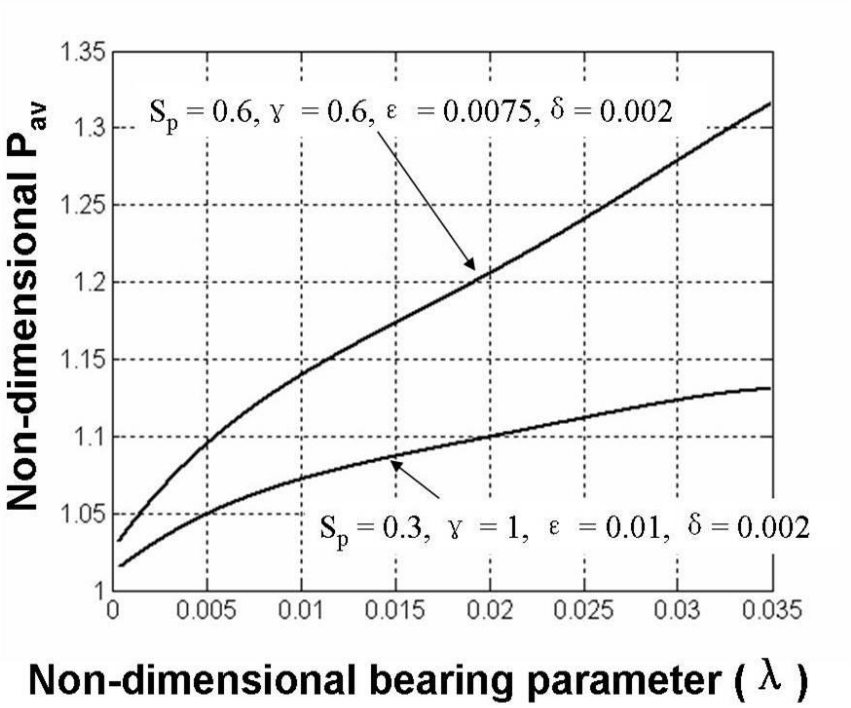

Figure 8.10: Non-dimensional average pressure as a function of the non-dimensional bearing parameter (λ) for optimum full surface texture and partial texture parameters

nificant and that the slope of the curve, representing the air film stiffness, is fairly steep. This shows that the stiffness of the bearing increases as the clearance decreases when surface texture is added.

Figure 8.10 shows the non-dimensional average pressure as a function of the non-dimensional bearing parameter (λ) for optimum full surface texture and partial texture parameters. From Figure 8.10, we observe that the non-dimensional average pressure increases as the bearing parameter increases. Since the bearing parameter λ is a function of the velocity, it is apparent that the average hydrodynamic pressure increases with

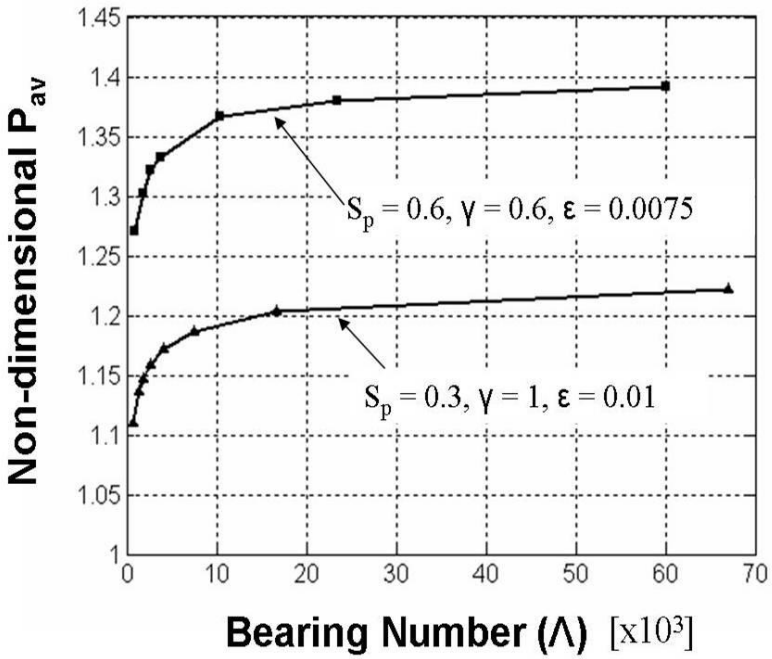

Figure 8.11: Non-dimensional average pressure as a function of the bearing number (Λ) for different aspect ratios (ε) and full surface texture

increasing velocity. We observe a similar trend for both partial and full texturing. The conventional definition of the bearing number, Λ given by $\Lambda = \lambda/\delta^2$, is that it is inversely proportional to the square of the air bearing clearance. Thus, in Figure 8.9, low clearance values imply high bearing numbers and vice versa.

Figure 8.11 shows the non-dimensional average pressure as a function of the bearing number Λ for optimum full surface texture and partial texture parameters. We observe that the average pressure increases with increasing bearing number for both full and partial surface texturing. This is expected since the clearance decreases for increasing

bearing numbers. We observe from Figure 8.11, that the change in the average pressure generated is very small in the range of bearing numbers between 10,000 and 70,000.

8.3 Effect of Pitch Angle and Comparison to Plane Inclined Slider Air Bearing Surface

An actual magnetic recording slider flies over the rotating disk with a positive pitch angle, i.e., only a small portion of the trailing edge region of the air bearing is close to the disk surface. The flying height in this region is referred to as the minimum spacing which is on the order of 10 nm in commercially available present day disk drives. To investigate the effect of pitch angle on the pressure generation, we have studied the single-row-of-texture model for the case of an inclined slider bearing. The plane inclined slider bearing and the single-row-of-texture model (with pitch) are shown schematically in Figure 8.12.

Figure 8.13 shows the non-dimensional average pressure as a function of the non-dimensional aspect ratio (ε) for texture density S_p = 0.3 and a pitch angle of 50 ţrad. Figure 8.14 shows the non-dimensional average pressure as a function of the texture density S_p for an aspect ratio ε = 0.01. The value of the pitch angle chosen is on the same order as that of actual air bearing slider used in this study (50 μrad). From Figures 8.13 and 8.14, we observe that the trend of the non-dimensional average pressure is similar to the one observed for a single-row-of-texture with parallel surfaces. We also

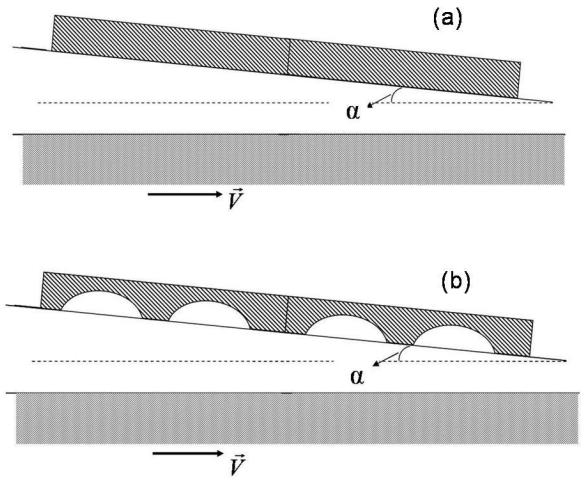

Figure 8.12: Schematic of (a) plane inclined slider bearing and (b) single-row-of-texture model with pitch (α_{cr})

observe that the amplitude of the non-dimensional pressure is higher than that for the parallel surface texture model. This effect is due to the inclination of the slider model which creates a net average pressure, even in the absence of texture.

In Figure 8.15 we compare the results for the textured slider with pitch to that for a plane inclined slider bearing of the same size without texture. From Figure 8.15, we observe that the non-dimensional average pressure increases with increasing pitch angle for both the textured model and the inclined slider bearing with no texture. We note that above a pitch angle of 150 μrad, the non-dimensional average pressure for the plane inclined slider bearing is higher than that for the corresponding textured case. Thus, above a critical value α_{cr} of the pitch angle, the effect of texture on the average pres-

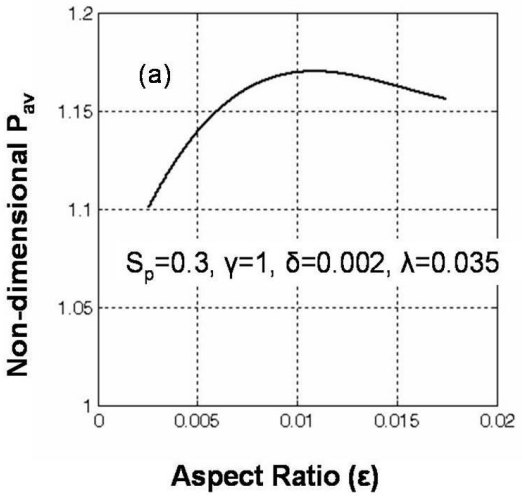

Figure 8.13: Non-dimensional average pressure vs. aspect ratio (ε) for texture model with pitch

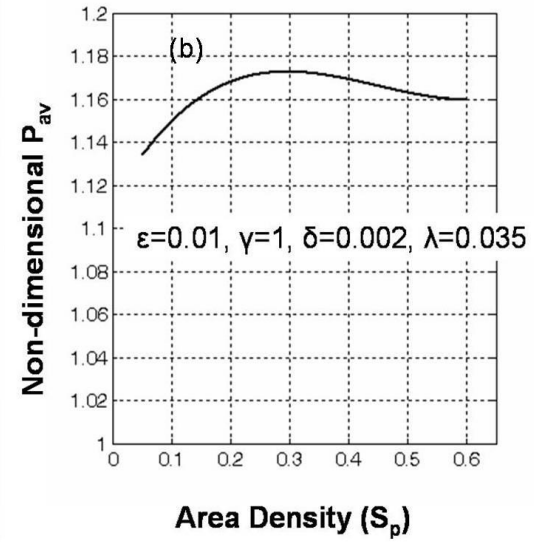

Figure 8.14: Non-dimensional average pressure vs. texture area density (S_p) for texture model with pitch

sure generation changes from increasing the average pressure to decreasing the average pressure, i.e., above the critical pitch angleα_{cr}, texture reduces the load carrying capacity while for pitch angles below the critical value, texture increases the load carrying capacity. This phenomenon is also observed in numerical simulations of actual slider, as will be shown later in this chapter. From Figure 8.15, we observe that the difference in the average pressure for textured parallel slider with zero pitch and the textures slider with 50 μrad pitch is less than 2 $\%$. We also note that the optimum texture aspect ratio and texture density are similar for both the parallel slider with surface texture and the textured slider with 50 μrad pitch. Thus, the optimum design parameters of surface texture that were obtained from the single row of texture model with the slider parallel to the disk surface can be used for the analysis of the actual slider even with the aspect of pitch included.

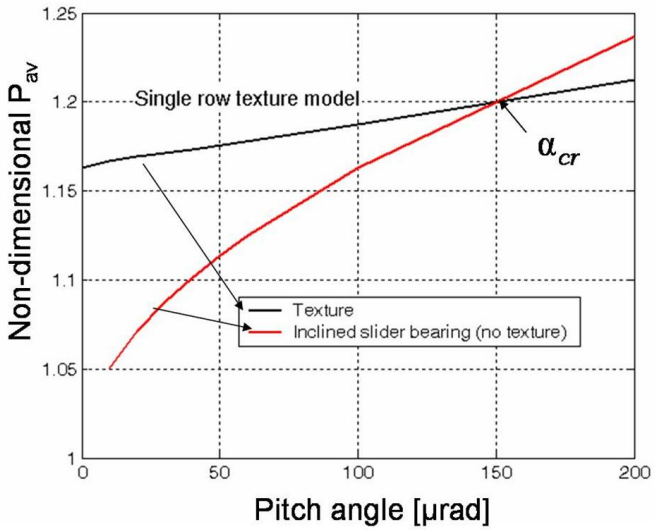

Figure 8.15: Non-dimensional average pressure as a function of pitch angle for single row textured model and for the inclined slider bearing with no texture

8.4 Steady State Flying Characteristics of Textured Sliders

In this section, we use the texture parameters found in the previous study and investigate the effect of texturing on the steady state flying characteristics of a typical magnetic recording slider. A comparison of the steady state flying characteristics were performed for textured and untextured magnetic recording sliders. The center trailing pads (high pressure region of the air bearing surface) of the pico and femto slider designs (Figure 8.16) were textured “numerically”. Figure 8.17 shows the inclusion of surface texture

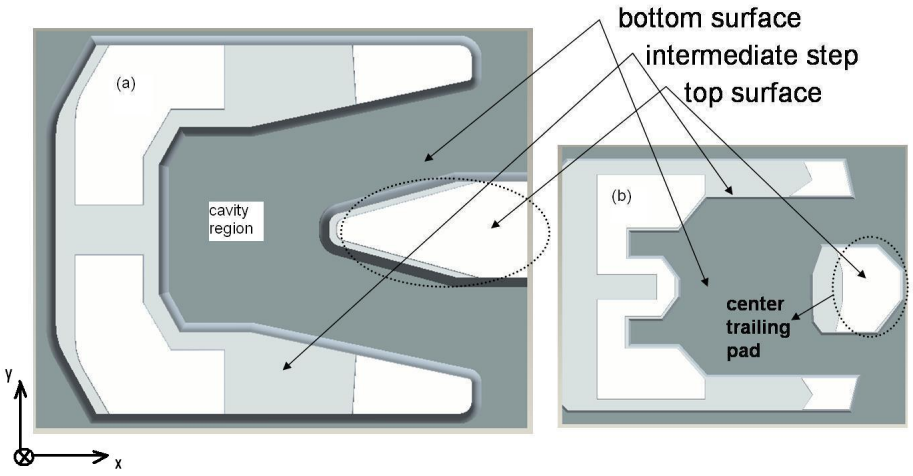

Figure 8.16: Slider air bearing design Pico (left), Femto (right)

on the center trailing pad of the slider air bearing surface.

Figure 8.18 shows the air bearing pressure distribution for both the untextured and the textured sliders (femto slider design). From Figure 8.18, we observe that texturing on the center trailing pad results in local high pressure peaks in the converging regions of each indentation. We also observe that the steady state flying height decreases for the textured slider compared to the untextured slider.

Figure 8.19 shows the non-dimensional average pressure for the untextured and textured slider (femto ABS design) as a function of the pitch angle. From Figure 8.19, we observe that the critical pitch angle α_{cr} is much smaller (about 14 μrad) for the actual slider than for the single-row-of-texture model.

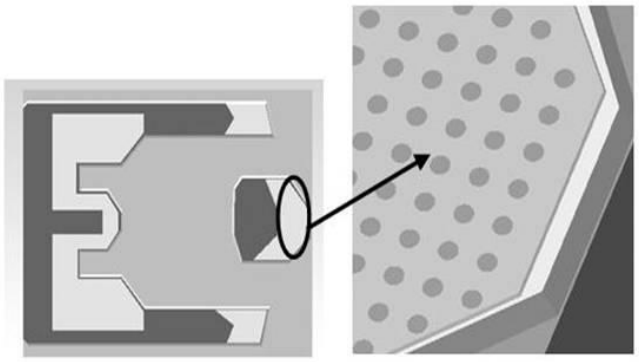

Figure 8.17: Surface texture on center trailing pad

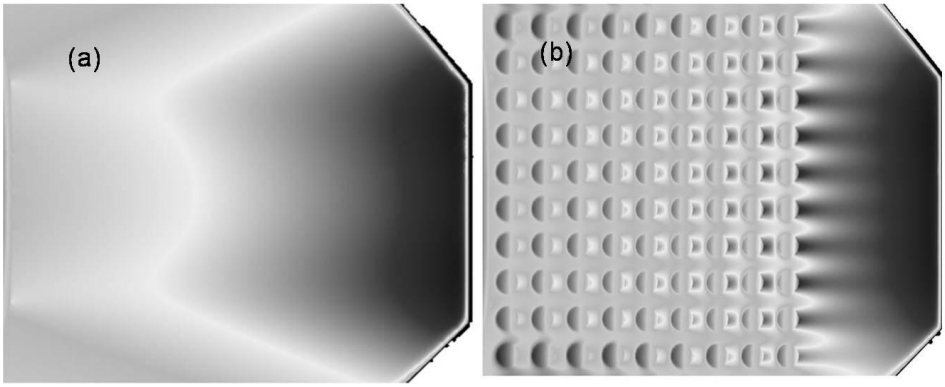

Figure 8.18: Pressure distribution on the center trailing pad for (a) untextured and (b) textured slider (Femto design)

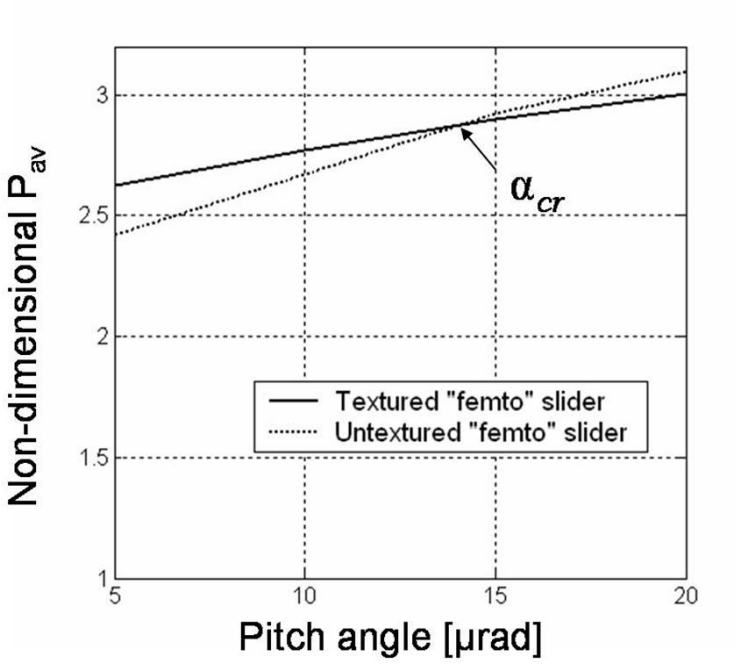

Figure 8.19: Non-dimensional average pressure as a function of pitch angle for untextured and textured magnetic recording slider (Femto design)

8.5 Dynamic Flying Characteristics of Textured Sliders

For the time dependent case, the Reynolds equation (see derivation in Chapter 6) is given by:

$$\nabla \cdot \left(Qph^3 \nabla p\right) = 6\mu \overrightarrow{V} \nabla \left(ph\right) + 12\mu \frac{\partial \left(ph\right)}{\partial t} \tag{8.8}$$

where p is the pressure, h is the spacing, is the disk velocity, μ is the viscosity, Q is the rarefaction term denoting the ratio of the Poiseuille flow rate to the continuum flow rate, and t is time. The rarefaction effects are considered by using the Boltzmann slip correction (Fukui and Kaneko, [(12)]).

To study the transient response of textured sliders, we have used the finite element formulation described in Chapter 6. A dynamic disturbance was simulated by numerically creating a step on the disk and studying the response of the slider to this disturbance. Both, untextured and textured sliders were used in our investigation. Figure 8.20 shows the response of the pico slider design shown in Figure 8.16 to a step in the disk. The flying height change is shown in Figure 8.20(a) for both an untextured and a textured slider, respectively, while Figures 8.20(b) and 8.20(c) show the pitch and roll for both types of sliders. From Figure 8.20(a), we observe that the steady state flying height of the textured slider is slightly lower than that of the untextured slider. We also observe that the maximum perturbation of the textured slider from the nominal flying height is less than that of the untextured slider. Furthermore, the minimum flying height, the minimum pitch and the minimum roll of the textured slider are slightly higher than the

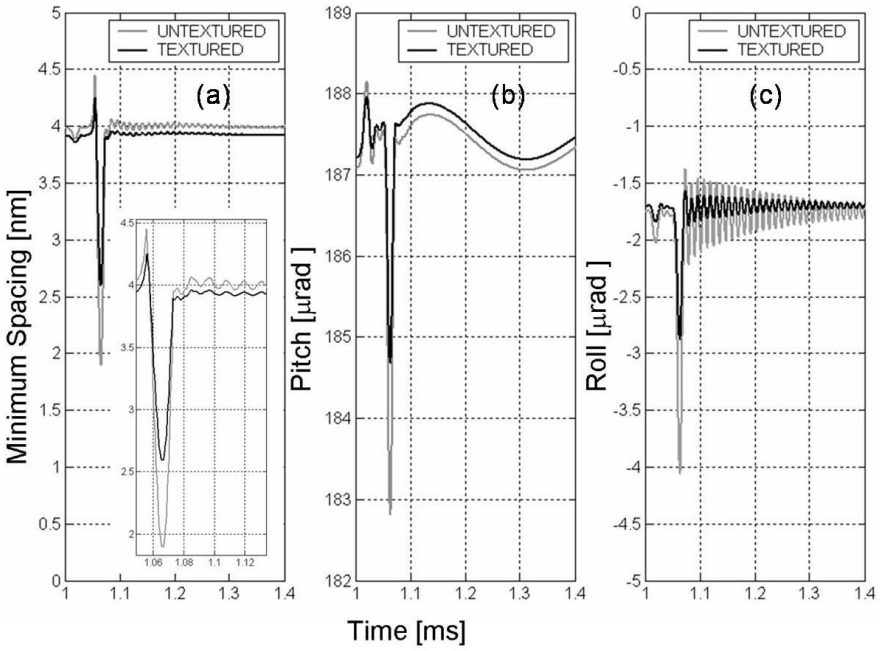

Figure 8.20: (a) Flying height modulation, (b) pitch, and (c) roll behavior for untextured and textured slider due to interaction with disk bump (Pico design)

corresponding values of the untextured slider. This seems to indicate a small increase in stiffness of the air bearing due to surface texture.

Figure 8.21 shows the flying height modulation for the femto slider design of Figure 8.16. We observe that the transient behavior of the minimum spacing is similar to the flying behavior of the pico slider design. We also observe from Figure 8.21(b) that the transient response of the slider displacement due to the disk bump dampens out faster for the textured slider than for the untextured slider. The minimum flying height observed for the textured slider is approximately 3.8 nm, whereas the minimum flying height for the untextured slider is about 1 nm. A larger minimum flying height in response to

a transient disk bump interaction implies that the likelihood of head disk contacts is reduced. Thus, the probability of impacts with the disk surface is reduced for textured sliders compared to the case of untextured sliders.

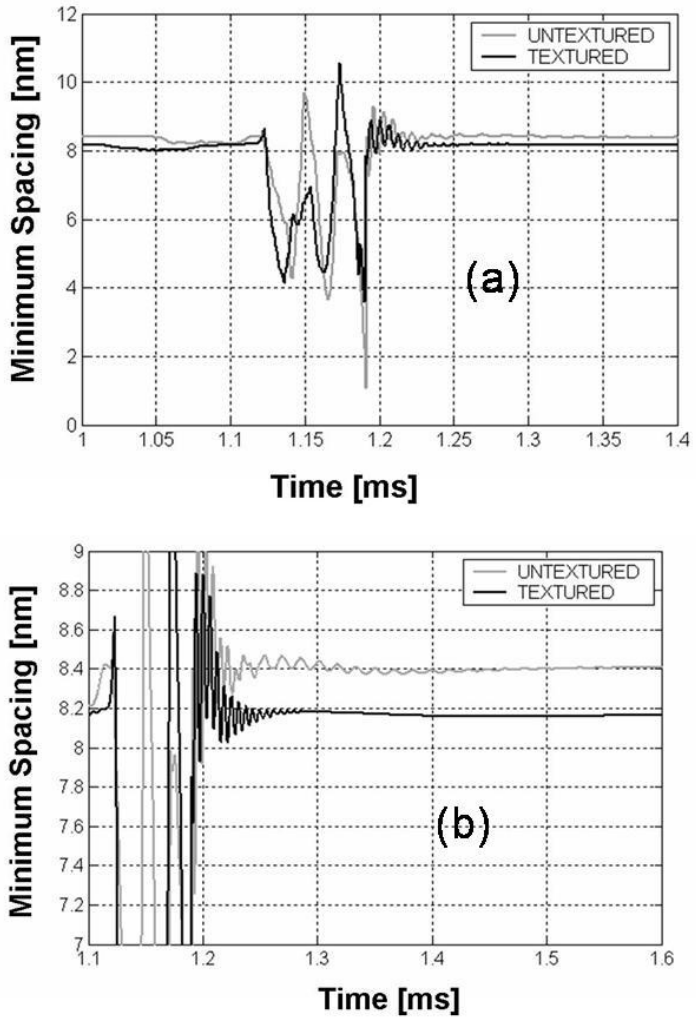

Figure 8.21: (a) Flying height modulation, (b) zoom in on the free response of slider displacement for untextured and textured slider after interaction with disk bump (femto design)

8.6 Operational Shock for Textured Sliders

To study the shock response during rotation of the disk (operational shock), the air bearing was modeled as a spring-mass system with springs in the z-direction as well as the pitch and roll directions. The force and moments on the slider were computed from the structural model and used subsequently in the solution of the time dependent Reynolds equation to determine the dynamic response of the air bearing to an applied external shock. The same procedure was used for both textured and untextured sliders. In a previous investigation by Zhou et al. [(8)] it was shown that texturing of sliders improves their tribological performance. To investigate the potential benefits of texturing on the shock response of sliders, we have numerically created a uniform texture pattern on the high pressure areas of the air bearing surface (Figure 8.17).

Figure 8.22 shows the flying height modulation for an untextured and a textured slider, respectively, for the same shock load, while Figure 8.23 shows the pitch and roll response. From Figure 8.22, we observe that the steady state flying height of the textured slider is slightly lower than that of the untextured slider. We also observe that the perturbation from the nominal flying height due to the shock is smaller for the textured slider than for the untextured slider. This indicates that damping of the air bearing is improved as a consequence of texturing. We also observe a similar effect in the pitch and roll response for textured sliders. The air bearing response to operational shock was similar to the results obtained for the disk step response in terms of lower amplitude of perturbation and better damping for the textured slider compared to that of

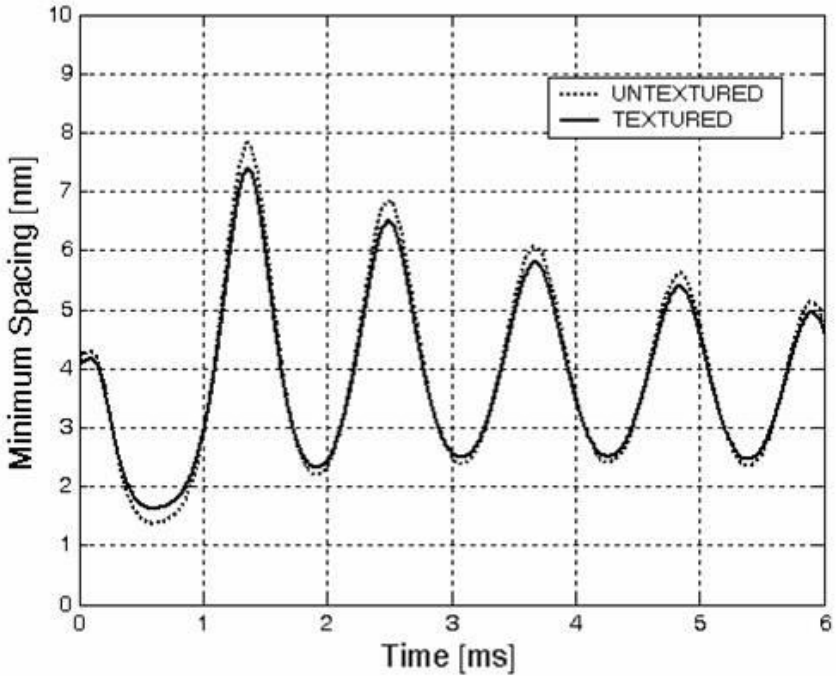

Figure 8.22: Flying height modulation of untextured and textured slider due to external shock (Pico design) (100G - 2ms half sine shock input)

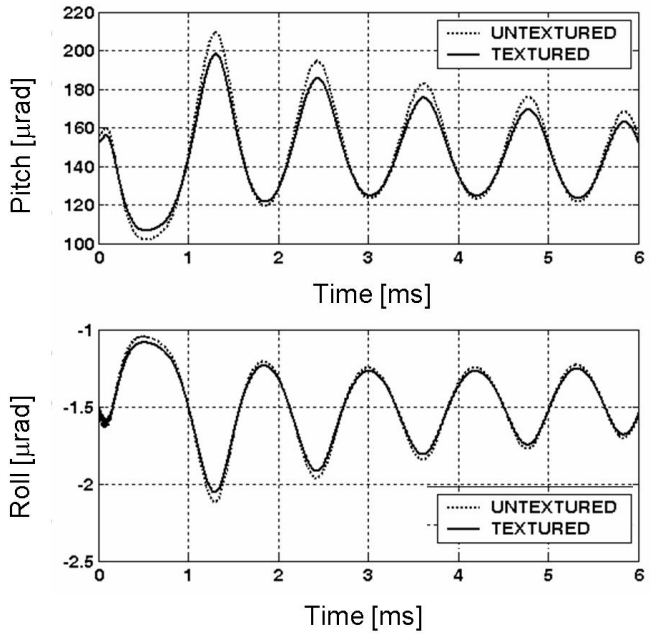

Figure 8.23: Pitch and roll for untextured and textured slider due to external shock (Pico design) (100G - 2ms half sine shock input)

the untextured slider.

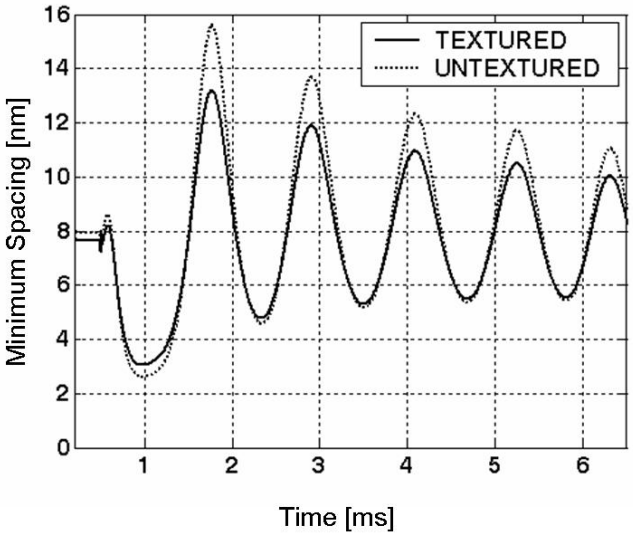

Figure 8.24: Flying height modulation of untextured and textured slider due to external shock (femto design) (100G - 2ms half sine shock input)

Figure 8.24 shows the dynamic flying height for the textured and untextured femto slider design used in this study. We observe that the textured slider shows lower displacement amplitudes in the positive and negative z-direction from the nominal flying height compared to the untextured slider. The peak-to-peak amplitude of the flying height modulation for the textured slider is approximately 10 nm as compared to 13 nm for the untextured slider. Thus, texturing the high pressure area of the air bearing surface reduces the likelihood of the slider impacting the disk surface. Sliders for 1-inch form factor drives are designed for rotational speeds between 3600 rpm and 4200 rpm, i.e.,

for linear velocities less than 3 m/s. The air bearing design plays an important role in maintaining a stable flying height and prevent head disk contact causing failure of the interface under shock and vibration loads. The simulation results show that texturing of the air bearing surface improves the dynamic characteristics of sliders to external shock loads.

8.7 Summary for Textured Sliders

The single-row-of-texture model for the parallel slider case showed an increase in the average pressure as a consequence of surface texture. An increase in average pressure generated was observed for both full surface texture and partial surface texture. The magnitude of the increase in the average pressure was higher for partial surface texture than for full surface texture. From the study of the inclined slider with a single-row-of-texture, we found that a critical value of the pitch angle exists above which the effect of texture changes from increasing the average pressure to decreasing the average pressure compared to an untextured slider. This phenomenon was found for an actual magnetic recording slider as well. Thus, in the design of textured air bearing sliders for magnetic recording applications, the pitch angle of the slider at steady state and transient positions is an important parameter which determines the effect of texturing. If the pitch angle is less than the critical pitch angle, surface texture will result in increased average pressure and hence increased load carrying capacity compared to an untextured slider.

If the equilibrium pitch angle is larger than the critical value of the pitch angle, texturing will have the opposite effect. For example, at steady state equilibrium, the value of the pitch angle for a typical "femto" slider was found to be approximately 55 μrad. Calculating the average pressure as a function of the pitch angle (5 μrad to 20 μrad), we found that the critical value of the pitch angle was approximately 15 μrad for the textured magnetic recording slider. Since the equilibrium value of the pitch angle of the textured slider under consideration is 55 μrad, it is apparent that texturing of the slider causes a decrease in the minimum flying height for steady state conditions compared to an untextured slider. Thus, a reduction in the load carrying capacity of the textured slider compared to the untextured slider is observed. An additional effect of texturing was found by Zhang et al. [16] with respect to intermolecular forces. In their work on textured sliders, Zhang et al. [16] have shown that surface texture is effective in reducing the effect of intermolecular forces. This can be explained as follows: the area of the surface in close proximity to the disk surface is reduced due to texturing and hence the area over which intermolecular forces act. Thus, texturing has an additional important effect on the flying characteristics of very low flying sliders. From our dynamic simulation results, we observe that the perturbation in the flying height of a very low flying slider from its nominal flying height is smaller for a textured slider than for an untextured slider. This indicates that surface texturing improves the stiffness of the bearing in the z-direction resulting in smaller amplitudes of perturbation for a textured slider than that for an untextured slider subjected to similar dynamic excitation. The lower

the perturbation, the smaller is the possibility of the slider coming into close proximity or into contact with the disk surface. The effect of intermolecular forces increases as the spacing between the slider and the disk decreases below 3 nm. From our simulation results, we observe that the free response of a slider after a dynamic excitation shows an improvement in damping characteristics of textured sliders compared to untextured sliders. The advantage of the single-row-of-texture model is that the texture design parameters could be parametrically analyzed to determine the optimum texture properties based on the desired effect for load carrying capacity or the flying height of the slider bearing. The trends observed in our single-row-texture-model were useful in analyzing the effect of texture on complicated air bearing surfaces of magnetic recording sliders.

8.8 Conclusion

Parallel slider bearings with surface texture generate a net load carrying capacity while untextured parallel sliders do not.

Surface texture reduces the load carrying capacity of an inclined slider above a critical pitch angle (with respect to the untextured slider), but increases the load carrying capacity below the critical pitch angle.

The dynamic flying characteristics of textured magnetic recording sliders show improved performance in terms of flying height modulation, stiffness and damping.

Texturing of air bearing sliders improves the dynamic performance of the head disk

interface.

Acknowledgment

Partial support of the work in this chapter was obtained through the National Science Foundation (NSF) under Grant CMS0408658

Part of the material in this chapter has been published online in the journal *Tribology Letters*: A. N. Murthy, I. Etsion and F. E. Talke, "Analysis of Surface Textured Air Bearing Sliders with Rarefaction Effects", 2007.

The dissertation author was the primary investigator of this paper and was directly supervised by Prof. Frank E. Talke. The co-author Prof. Itzhak Etsion has given his permission to include the material of the paper in this dissertation.

Part of the material in this chapter has been published in the *Microsystem Technologies Journal*: A. N. Murthy, M. Pfabe, J. Xu, and F. E. Talke, "Dynamic Response of 1-inch Form Factor Disk Drives to External Shock and Vibration Loads", Microsystem Technologies, published online, 2006.

The dissertation author was the primary investigator of this paper and was directly supervised by Prof. Frank E. Talke. The co-authors Mathias Pfabe and Jiafeng Xu have given their permission to include the material of the paper in this dissertation.

Bibliography

[1] Etsion, I., Kligerman, Y., and Halerpin, G., "Analytical and Experimental Investigation of Laser-Textured Mechanical Seal Faces," *Tribology Transactions*, 42, 3, pp 511-516, (1999)

[2] Kligerman, Y., Etsion, I. and Shinkarenko, A., "Improving Tribological Performance of Piston Rings by Partial Surface Texturing," *ASME Journal of Tribol*ogy, 127, pp 632-638, (2005)

[3] Brizmer,V., Kligerman,Y. and Etsion, I., "A Laser Surface Textured Parallel Thrust Bearing," *Tribology Transactions*, 46, pp 397-403, (2003)

[4] Kligerman,Y. and Etsion, I., "Analysis of the Hydrodynamic Effects in a Surface Textured Circumferential Gas Seals," *Tribology Transactions*, 44, pp 472-478, (2001)

[5] Knigge, B., Zhao, Q., Talke, F.E., and Baumgart, P., "Tribological Properties and Environmental Effects of Nano and Pico Sliders on Laser Textured Media," *IEEE Transactions on Magnetics*, Vol.34 (no. 4): 1732-1734, 1998

[6] Khurshudov, A., Knigge, B., Talke, F.E., Baumgart, P., and Tam, A., "Tribology of Laser-Textured and Mechanically-Textured Media," *IEEE Transactions on Magnetics*, Vol.33 (no. 5): 3190-3192, 1997

[7] Hu, Y., and Bogy, D. B., "Effects of Laser Textured Disk Surfaces on Slider"s Flying Characteristics," *ASME Journal of Tribology*, 120, 2, pp 266-271, (1998)

[8] Zhou, L., Beck, M., Gatzen, H.H., Kato, K., Vurens, G., and Talke, F.E., "The Effect of Slider Texture on the Tribology of Near Contact Recording Sliders", *Tribology Letters*, Vol.16 (no. 4): 297-306, (2004)

[9] L. Su, S. K. Deoras, F.E. Talke, "Investigation of Tribological and Read-Write Performance of Textured Sliders,"*IEEE Transactions on Magnetics*, 41, 10, 3025-3027 (2005)

[10] J.Gui, H.Tang, Li-P.Wang, G.C.Rauch, Z.Boutaghou, J.Hanchi, T.Picthford, P.Segar, "Slip sliding away: A novel HDI and its tribology," *Journal of Applied Physics*., 87, 9, 5383-5388 (2000)

[11] L. -J. Fu, B. Knigge, F. E. Talke and T. Yamamoto. "Stiction of 'Padded,' 'Stepped' and 'Crowned' Pico Sliders," *Journal of Information Storage Processing Systems*, 2, 117-123, (2000)

[12] Fukui, S. and Kaneko, R., "Analysis of Ultra-Thin Gas Film Lubrication Based on Linearized Boltzmann Equation: First Report"Derivation of a Generalized Lubrication Equation Including Thermal Creep Flow," *ASME Journal of Tribol*ogy, 110, pp. 253-262 (1988)

[13] Lacey, C., Talke, F. E., "A Tightly Coupled Numerical Foil Bearing Solution," *IEEE Transactions on Magnetics,* Vol.26 (no. 6): 3039-3043, 1990

[14] Wahl, M., Lee, P., Talke, F. (1996), "An Efficient Finite Element-Based Air Bearing Simulator for Pivoted Slider Bearings using Bi-Conjugate Gradient Algorithms," *STLE Tribology Transactions*, 39 (1)

[15] Duwensee, M., Suzuki, S., Lin, J., Wachenschwanz, D., Talke, F.E., "Simulation of the head disk interface for discrete track media," *Microsystem Technologies*, Published On line: Nov., 2006

[16] Zhang, J., Su, L., Talke, F.E., "Effect of surface texture on the flying characteristics of pico sliders", *IEEE Transactions on Magnetics*, 41, 10, 3022-3024, 2005

9

Numerical Simulation of the Head/Disk Interface for Patterned Media

9.1 Overview

The use of patterned media is a new approach proposed to extend the recording densities of hard disk drives beyond 1 Tb/in^2. Bit patterned media (BPM) overcome the thermal stability problems of conventional media by using single-domain islands for each bit of recorded information, thereby eliminating the magnetic transition noise [1]. Considering steady state conditions, we have transferred the pattern from the disk surface onto the slider surface and have investigated the pressure generation due to the bit pattern. To reduce the numerical complexity, we have generated the bit pattern only in the areas of the slider near the trailing edge, where the spacing is small. Cylindrical

protrusions were modeled using very small mesh size on the order of nanometers to obtain the flying characteristics for the entire slider air bearing surface (ABS) using the "CMRR" finite element Reynolds equation simulator [18, 10]. The effect of pattern height, pattern diameter, slider skew angle, and slider pitch angle on flying height of a typical slider is investigated.

9.2 Introduction to Patterned Media

Patterned media for hard disk drives can be used in the form of discrete tracks or discrete bits. In discrete track recording, the bits are stored on discrete circumferential tracks on the disk. In bit patterned media, each bit is stored on a single magnetic domain or "island". Magnetic transitions no longer occur between random grains as in conventional media, since distinct boundaries between islands are formed both in the circumferential and the radial directions on the disk. Several investigations have been published that discuss the head disk interface for patterned media. Wachenschwanz et al. [2] reported an increase in the signal to noise ratio (SNR) and a better write efficiency for discrete track type of patterned media. Head/disk interfaces for patterned media are complicated to manufacture and pose challenging problems from a tribological viewpoint. The air bearing domain in bit patterned media is highly influenced by the existence of surface features on the disk. Island-like cylindrical structures on the disk surface in the radial and circumferential directions change the air bearing pressure

contours of the head/disk interface compared to a conventional head/disk interface with a "smooth" disk. Duwensee et al. [3] studied the influence of discrete track pattern on pressure generation in slider bearings. They reported that very high and localized air bearing pressure peaks occur in discrete track head/disk interfaces, and that the slider pitch angle was independent of the DTR parameters.

Gui et al. [4] and Fua et al. [5] studied padded sliders and reported that padded sliders have benefits in terms of reducing head/disk interactions and friction during contact start stop. W.-L. Li et al. [6] studied the pressure of pattern on two-rail slider bearings and found that patterned sliders showed better stiction properties than unpatterned sliders. They also found that an increase in the pattern pitch and pattern height decreases the flying height. Tagawa et al. [7] investigated the effect of longitudinally grooved slider surfaces on the flying behavior of a two rail slider flying over a smooth disk surface. Tagawa and Mori [8], [9] extended the work reported in [7] to head disk interface for patterned media. They considered surface pattern that were on the order of 5 μm to 20 μm in width and length direction and 10 nm to 40 nm for the pattern height, respectively. They determined the pressure distribution for a two rail, positive pressure slider and observed an increase in the flying height due to surface pattern. In a more recent investigation, Duwensee et al. [10] have numerically studied the head disk interface for discrete track recording. They investigated the effect of groove depth on the flying height and flying attitude for a constant ratio of groove width to groove pitch. They proposed an empirical expression for the flying height loss as a function of groove depth,

groove pitch and groove width. Their calculation used a very fine mesh descretization in the region of the slider air bearing surface that is closest to the disk. A typical model consisted of 2.7×10^6 finite elements, 1.3×10^6 nodes, and required large computer memory.

Alternative techniques such as homogenization and Direct Simulation Monte Carlo (DSMC) methods have also been implemented to study the influence of surface pattern on the slider or disk surface. Buscaglia and Jai [12], applied homogenization techniques to the Reynolds equation to take fine but periodic surface structures into consideration. They presented the spacing between slider and disk as the sum of a high frequency contribution which is known and a low frequency contribution that is unknown. The high frequency part represents the periodic spacing variations due to surface features on the disk or on the slider. The unknown part must be computed during the numerical solution of the Reynolds equation. Homogenization techniques allow a coarser domain discretization than direct simulation methods. However, the local resolution of the pressure distribution of the air bearing is reduced due to homogenization. If details of the pressure distribution on the order of the surface features are of importance, the homogenization technique is not suitable. Alexander et al. [13] and Huang et al. [14, 15] applied the DSMC method to check the validity of the modified Reynolds equation for high Knudsen number flow in "smooth" head/disk interfaces in two and three dimensions, respectively. They reported that the DSMC method compared close to the simualtion results obtained by solving the Reynolds equation. Duwensee et al. [16]

have used the DSMC method to study the pressure generation in a nano slider covering one groove and land region for DTR type disk.

In this chapter, we present a direct numerical simulation that investigates the head/disk interface for patterned media by considering the entire slider air bearing surface. A finite-element-based solution of the Reynolds equation is used to obtain the steady state flying characteristics of the patterned head disk interface. In areas of high pressure and low spacing, a very fine mesh is selected to investigate the effect of the ultra small features and determine the influence of pattern on the air bearing pressure. In areas of higher spacing, a coarser finite element mesh was chosen, since the influence of surface features is decreasing with increasing spacing. The numerical approach is similar to that used by Duwensee et. al [10] in the study of the head disk interface for discrete track media.

9.3 Simulation Model for Patterned Slider

Figure 9.1 shows the transfer of the bit pattern from the disk surface to the slider air bearing surface (ABS). As can be seen, the pattern is present on the center trailing pad of the slider and is modeled as cylindrical protrusions of diameter d, height h, and pitch p. The protrusions are uniformly distributed representing the pattern from the disk in the radial and circumferential directions.

Figure 9.2 shows the definition of the patterned slider parameters. In Figure 9.2, 'p'

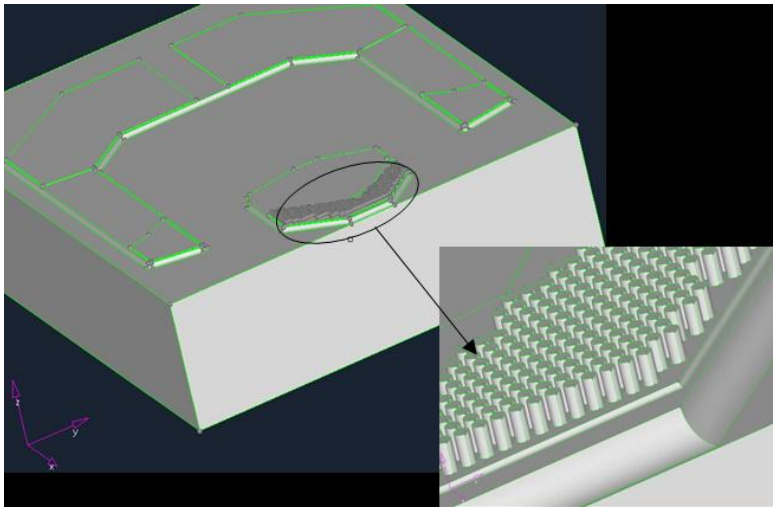

Figure 9.1: Schematic of pattern transfer from disk to trailing pad of slider air bearing

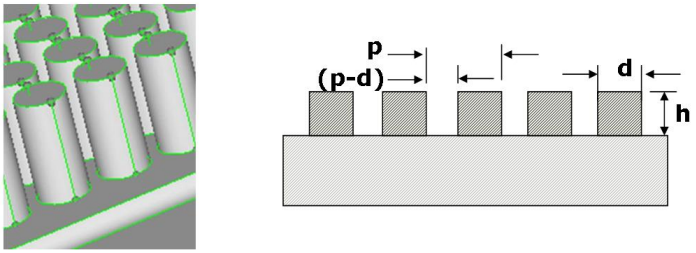

Figure 9.2: Definition of pattern pitch (p), pattern diameter (d), and pattern height (h)

denotes the pattern pitch, ’d’ denotes the pattern diameter, and ’h’ denotes the pattern height. The same pitch p is used both in the length and the width directions of the slider. The nearest distance between two pattern features in both the length and the width directions of the slider is ’(p-d)’.

The air bearing pressure distribution and equillibrium position are obtained by a finite element solution of the steady state Reynolds equation [18, 3] as explained in chapters 6 and 7.

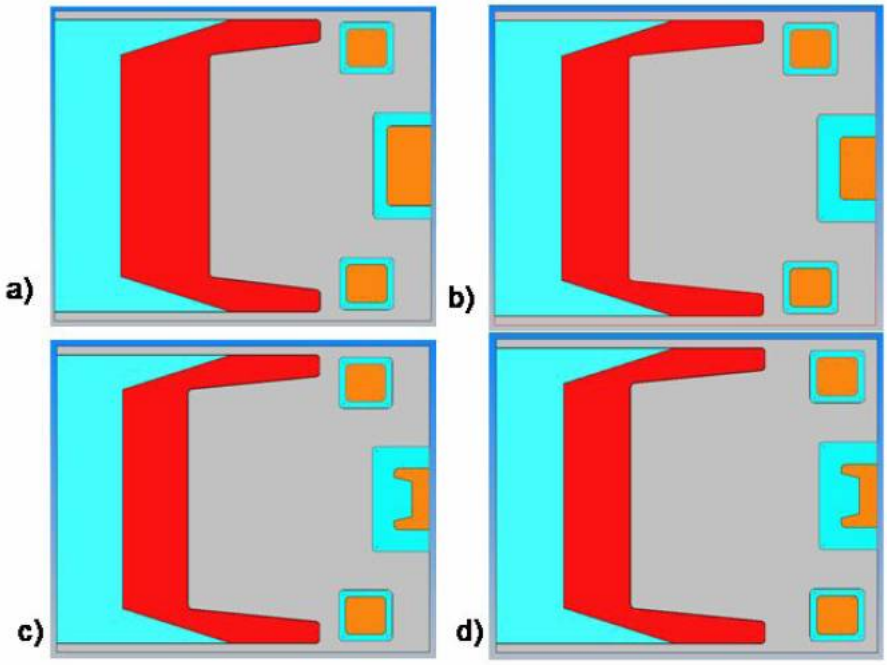

Figure 9.3: Femto form factor slider air bearing designs 1, 2, 3 and 4 (labeled a,b,c and d respectively) [10]

Four “femto” form factor slider designs with different steady state flying characteristics were investigated as a function of pattern design parameters (Figure 9.3). These

slider designs were previously investigated by Duwensee et al. [10] for discrete track media. The four femto sliders shown in Figure 9.3 have steady state flying heights of 30 nm, 14 nm, 15 nm, and 19 nm, respectively, on a conventional smooth disk. The four femto sliders are design modifications of the femto slider shown in Figure 9.3(a). The steady state pitch angles of the four femto designs on a smooth disk surface are 250 μrad, 170 μrad, 166 μrad, and 154 μrad, respectively.

In the initial calculation, a fairly large pattern diameter of 3 μm was used for the slider shown in Figure 9.1 to obtain the pressure generation around the pattern features. Large diameter pattern features were chosen for visualizing the effect of pattern on air bearing pressure.

For the four femto designs shown in Figure 9.3, pattern heights between zero and 40 nm ($0 < d < 40$ nm) were investigated. A pattern diameter between 200 nm and 800 nm was used with a constant pattern pitch of 1000 nm. In addition, the influence of skew angle (ranging from zero to 20 deg), the effect of slider pitch angle, and the effect of pattern diameter were investigated. Due to the small pattern features on the trailing edge center pad, a very fine mesh discretization was required. A uniform mesh density over the complete air bearing surface would result in numerical models with several tens of millions of nodes. To reduce the model size, a non-uniform mesh was used for the simulation. Very small elements were used in the area where the pattern features are present and increasingly larger sized elements elsewhere. In particular, between 30 to 50 elements were created for each individual pattern . The number of pattern features

on the trailing edge center pad of the femto slider designs were on the order of 5 to 8 thousand. For example, slider design 3 (9.3(c)) had a center trailing pad area of about 140 μm $\times$ 40 μm resulting in 5600 pattern features. The total number of nodes and elements for this slider model was on the order of 0.7×10^6 and 1.4×10^6, respectively.

9.4 Numerical Simulation Results

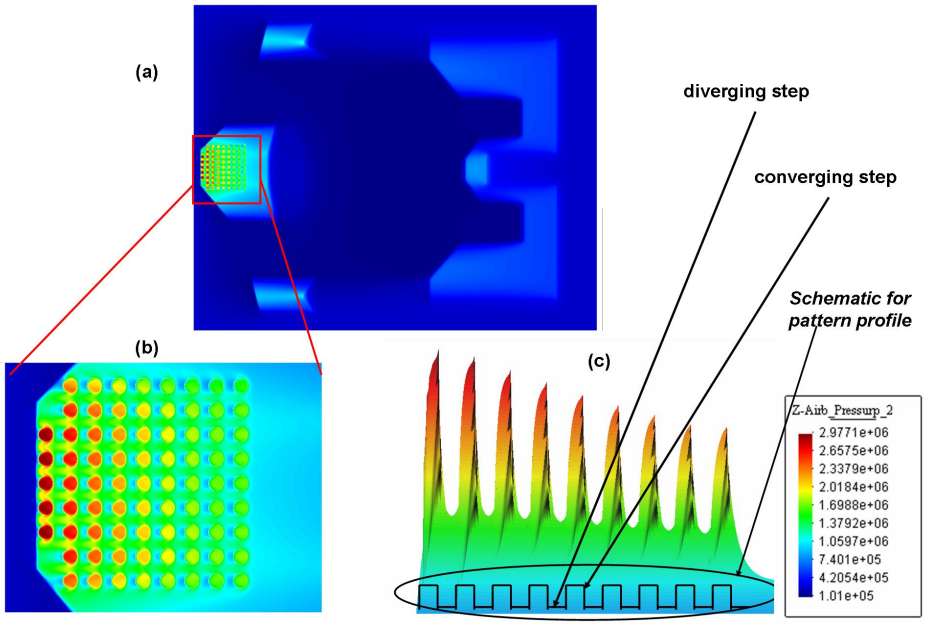

Figure 9.4: Steady state pressure distribution for: (a) patterned air bearing slider, (b) zoom in plot for pressure on the center trailing pad with pattern, (c) side view along the slider centerline

Figure 9.4 shows the steady state pressure distribution for the femto air bearing design shown in Figure 9.1. In Figure 9.4, a large pattern diameter of about 3 μm was

chosen to elucidate the pressure generated around individual pattern features. Figure 9.4(b) shows the pressure for the pattern features on the center trailing pad. We observe that large pressure changes occur locally at each pattern feature. Figure 9.4(c) shows the side view of the pressure along the slider centerline. We observe that the pressure increases locally around the converging portions of each pattern feature. In the diverging spacing region of the pattern feature, the pressure decreases. A single pattern feature is similar to a Rayleigh step bearing with converging and diverging sections. We also observe from Figure 9.4(c) that the maximum pressure occurs on the pattern features closest to the trailing edge of the slider due to the pitch angle of the slider.

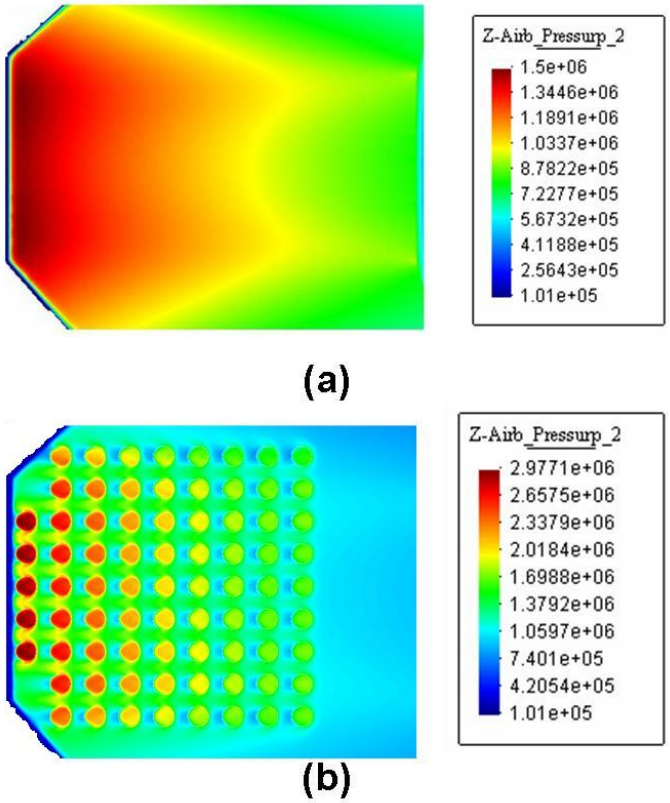

Figure 9.5: Steady state pressure distribution for (a) an non-patterned ABS and (b) a patterned ABS

Figure 9.5 shows the comparison of the pressure distribution for an non-patterned slider and a patterned slider. The diameter and height of the pattern used in Figure 9.5(b) are 3 μm and 20 nm, respectively. From Figure 9.5(b) we observe that the pressure distribution on the center trailing pad, where the pattern is present, is quite different from Figure 9.5(a). The maximum pressure generated for a patterned slider is larger than the maximum pressure for a non-patterned slider.

In Figure 9.6, we have plotted the pressure profile along the width of the slider.

We observe that high pressure peaks occur at each pattern feature, superimposed on a smooth background pressure. These pressure peaks are present over each pattern feature in both the length and width directions of the slider. The top surface of each pattern feature is the area in closest proximity to the disk surface. These areas represent the minimum spacing. The recessed regions of the patterned features and the other regions of the air bearing surface are farther away from the disk surface. Hence, an increase of local air bearing pressure in areas close to the disk surface is to be expected. The high pressure spikes are likely to cause lubricant migration or lubricant depletion.

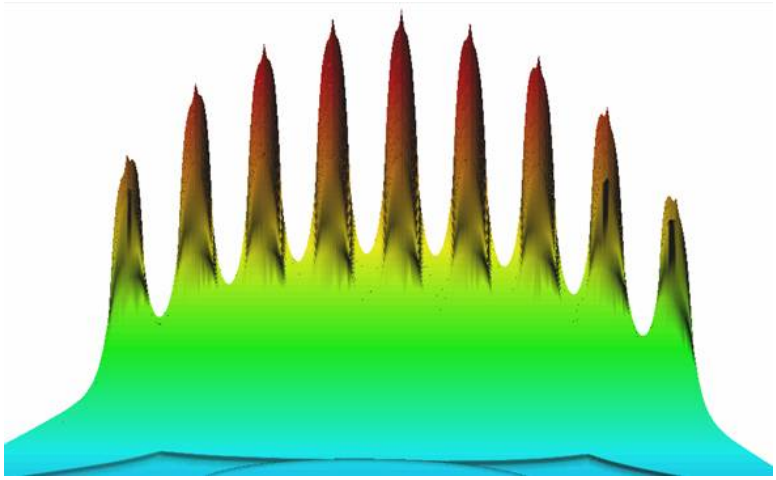

Figure 9.6: Pressure peaks due to pattern on ABS

To investigate the effect of pattern height, pattern diameter, slider skew and pitch angles on flying height, a parametric study was performed.

Figure 9.7 shows the trailing edge center spacing as a function of the pattern height for the femto slider designs shown in Figure 9.3. For this calculation, the ratio of diameter to pitch of the pattern features was kept constant at 0.5. From Figure 9.7, we observe

that the trailing edge center spacing decreases with increasing pattern height. We also observe that the slope of the flying height versus pattern height curve is similar for all four slider air bearing designs.

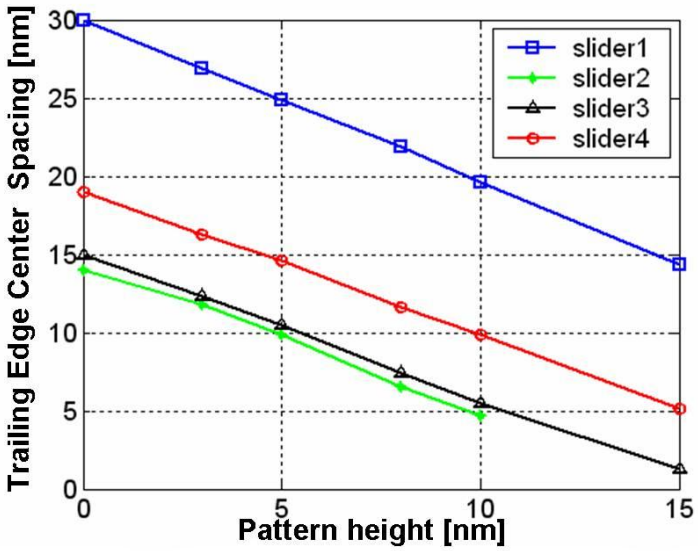

Figure 9.7: Trailing edge center spacing as a function of pattern height for slider designs 1, 2, 3 and 4 keeping d/p constant at 0.5

The flying height loss of the four femto sliders as a function of pattern height h is plotted in Figure 9.8 for a ratio of d/p = 0.5. We observe that the flying height decreases linearly as a function of the pattern height. That trend is similar for all four slider designs.

The steady state flying height of a patterned slider disk interface with a constant ratio of d/p = 0.5 can be estimated by subtracting $\triangle FH$ from the flying height on a conventional smooth head disk interface. The dotted line in Figure 9.8 was obtained

using the following equation:

$$\triangle FH = 2\,h\,\frac{d}{p} \tag{9.1}$$

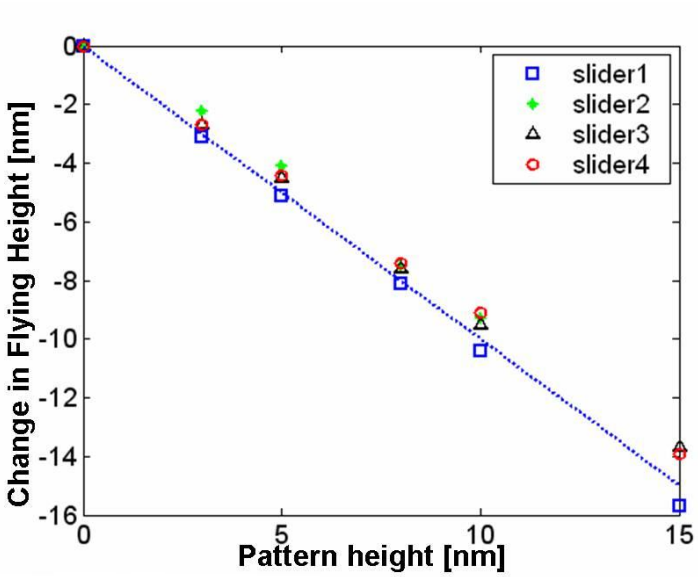

Figure 9.8: Change in Flying Height as a function of pattern height for femto slider designs (d/p = 0.5)

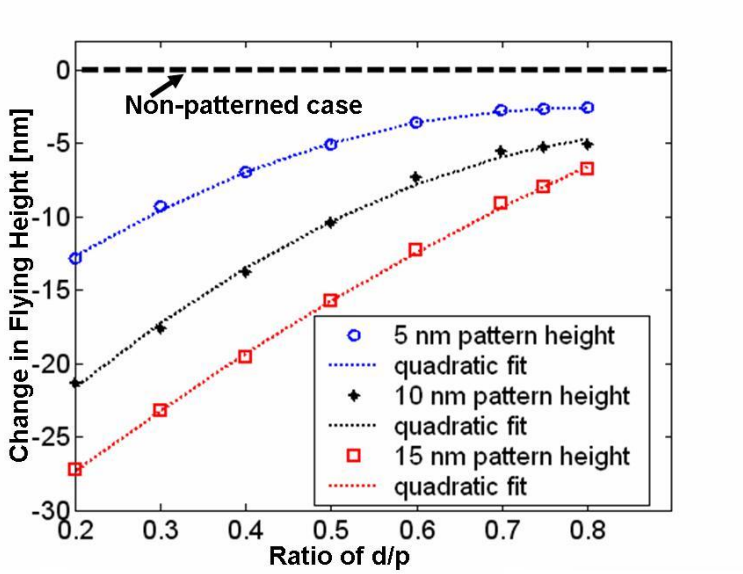

Figure 9.9: Change in flying height as a function of the ratio d/p for femto slider design 1

Figure 9.9 shows the change in flying height as a function of the pattern diameter. The change in flying height is plotted as a function of the ratio d/p. The dashed horizontal line in Figure 9.9 corresponds to the non-patterned case. In Figure 9.9, the pattern diameter was varied between 200 nm and 800 nm keeping the pattern pitch constant at 1000 nm. From Figure 9.9 we observe that the change in flying height is non-linear as a function of the pattern diameter. The solid, dotted, and dashed lines in Figure 9.9 represent a quadratic fit for a pattern height of 5 nm, 10 nm, and 15 nm, respectively.

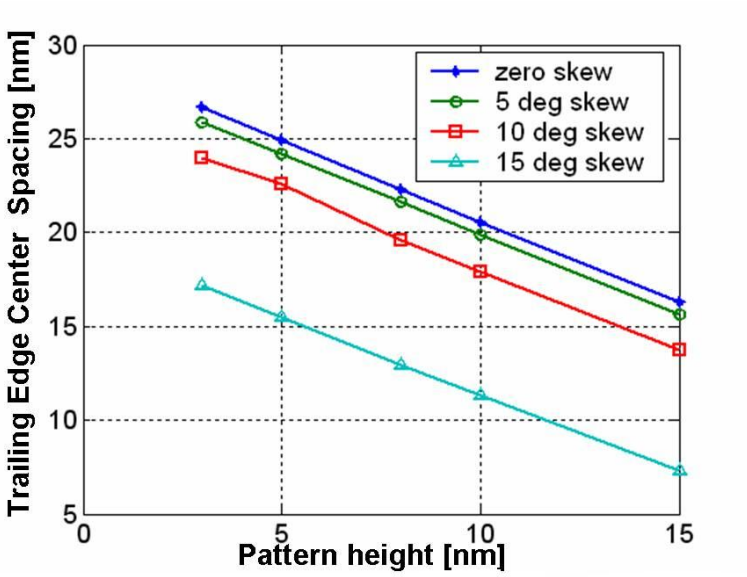

Figure 9.10: Trailing edge center spacing as a function of slider skew angle for femto slider design 1

Figure 9.10 shows the trailing edge center spacing of femto slider design 1 as a function of the pattern height for skew angles of zero, five, ten, and twenty degrees (0, 5, 10, 20 deg), respectively. The ratio of the pattern diameter to the pattern pitch was chosen to be one half (d/p = 0.5). A linear decrease in the trailing edge center spacing is observed with increasing pattern height, indicating that Eq. (9.1) applies also for non-zero skew cases.

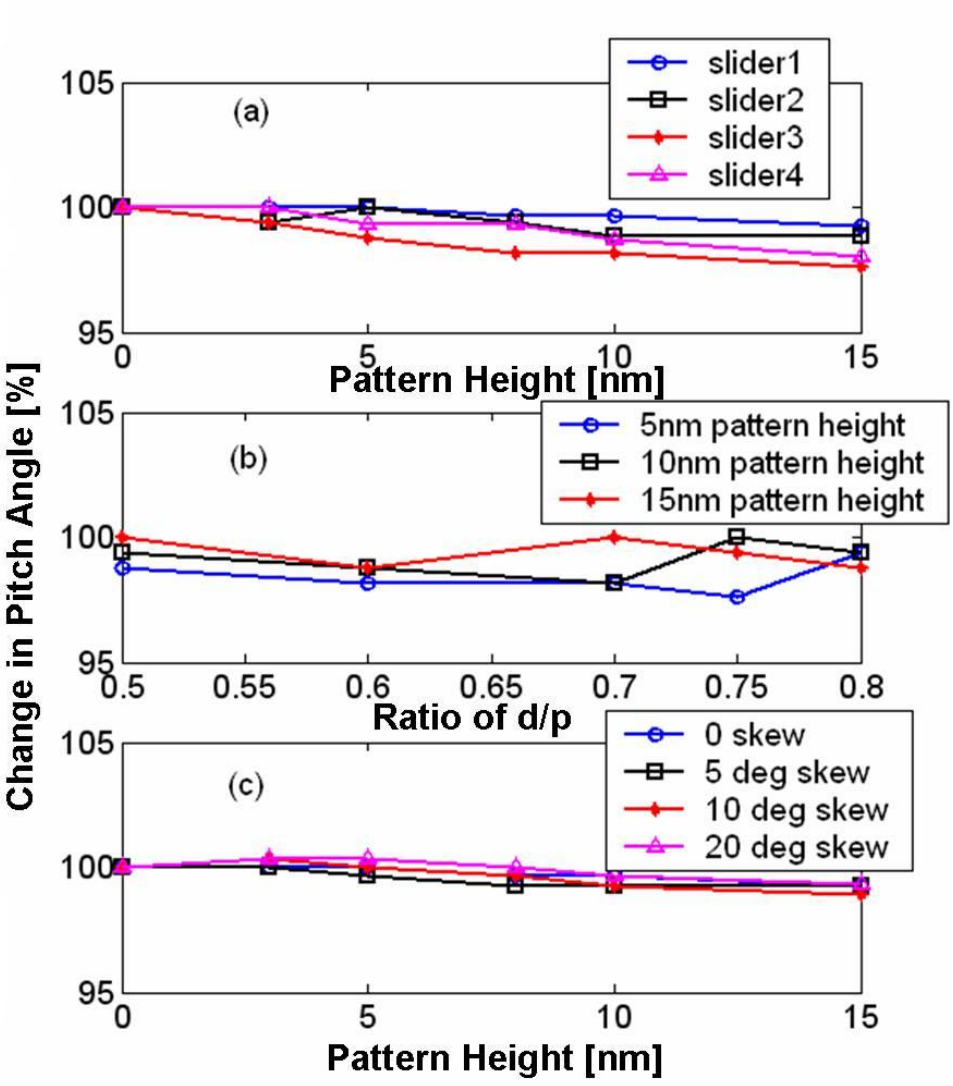

Figure 9.11: Pitch angle change versus (a) pattern height for different femto slider designs, (b) ratio d/p (slider design 3) and (c) pattern height for different skew angles (slider design 3)

The effect of the slider pitch angle on pattern height is shown in Figure 9.11. From the simulation results, we observe that the change in the slider pitch angle is almost

independent of slider air bearing design, pattern height, the ratio d/p, and the slider skew angle. From Figure 9.11, we conclude that the presence of pattern with diameter on the order of several nanometers does not effect the pitch angle of the slider body.

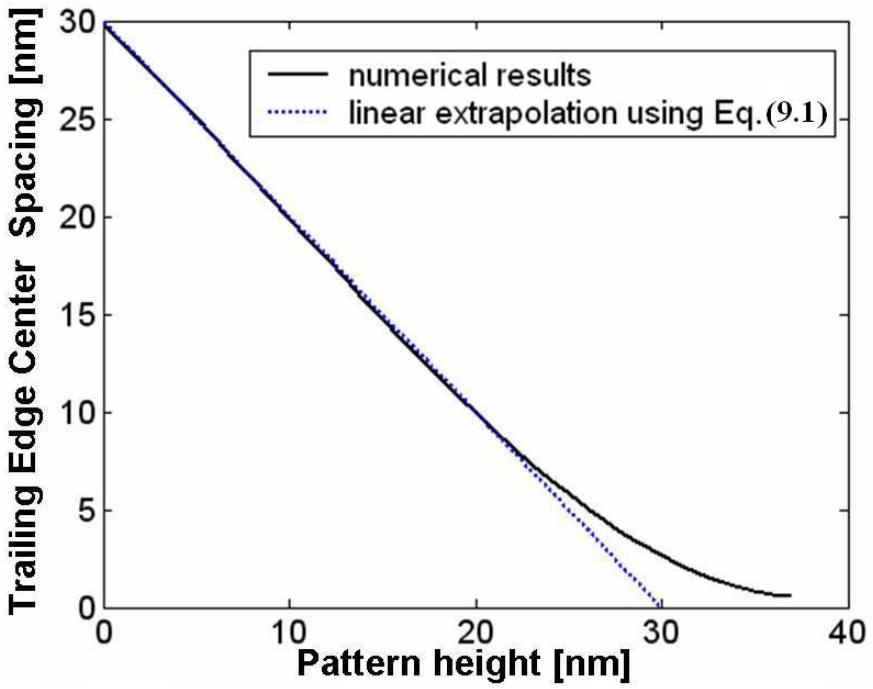

Figure 9.12: Trailing edge spacing versus pattern height (slider 1)

To determine the general relationship between flying height and pattern height, the trailing edge center spacing was computed by increasing the pattern height for slider design 1 until the flying height reaches zero, i.e., until contact between slider and disk occurs (Figure 9.12). In the claculation for Figure 9.12, the pattern diameter and pitch were 500 nm and 1000 nm, respectively. From the linear extrapolation of the flying height using Eq. (9.1) for slider design 1, we observe that contact occurs for a pattern

height of 30 nm. However, from the numerical simualtion using the finite element solution of the Reynolds equation, we observe that the numerical results for flying height deviate from the predicted values for pattern heights larger than 20 nm for slider design 1. Thus it is apparent that the linear approximation for flying height loss is valid for only small pattern heights. Beyond a critical value of pattern height, the change in flying height is non-linear and a full air bearing simualtion is necessary to compute the change in flying height correctly.

9.5 Discussion and Summary

From our simulation results we observe that the flying height decreases as a function of pattern height and the ratio of pattern diameter to pattern pitch. Our calculations show that the redcution in flying height is a linear function of the pattern height for small values of pattern height. Beyond a certain value for the pattern height, the change in flying height becomes non-linear. For the patterned slider simulations shown in this chapter, Eq. (9.1) can be used to predict the change in flying height for small pattern heights and for a ratio of pattern diameter to pattern pitch equal to one half.

Duwensee et al. [10] obtained an empirical equation that predicts the change in flying height for discrete track reording (DTR) media as follows:

$$\triangle FH = groove\,depth \times \frac{groove\,width}{groove\,pitch} \quad \text{(Duwensee et al. [10])}$$

Comparing this equation to our simualtion results for a bit-patterned slider disk interface, we observe that the groove depth of discrete track disks is analogous to the pattern height of a bit patterned disk, and that the groove width is analogous to the area recessed around a pattern feature. In addition, the groove pitch is similar to the pattern pitch. For a DTR interface, the flying height loss is linearly proportional to the groove depth and the ratio of groove width to groove pitch for any value of groove depth and groove width for a constant groove pitch [10]. This is due to the fact that the length of the groove and the land regions of the discrete track are the same and that the groove pattern is uni-directional.

A non-linear change in flying height was observed for a bit patterned slider disk interface when the pattern diameter was varied. The change in flying height was found to be a quadratic function of the pattern diameter. This result is to be expected since a change in the pattern diameter not only changes the pattern profile along the width of the slider, but also along the length of the slider. For the DTR interface, a change in width changes the pattern profile only along the width of the slider. For a range of different pattern diameters and pitch ratios, a functional relationship would have to be written as $\triangle FH = f(\text{h}) \times f(\text{d/p})$. The value of $f(\text{d/p})$ is different for various ratios of pattern diameter to pattern pitch.

For a DTR interface, an area ratio representing the ratio of recessed area due to groove width to the area due to groove pitch can be written as w/p. For the patterned

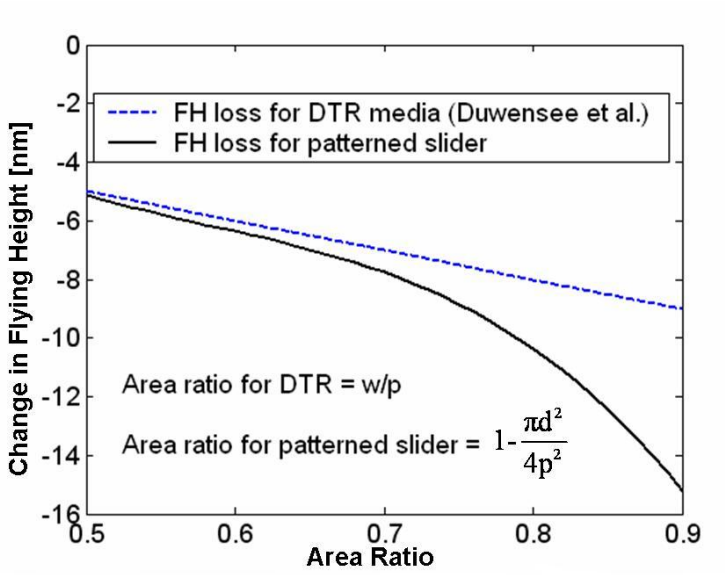

Figure 9.13: Comparison of change in flying height for discrete track recording and bit patterned slider as a function of the area ratio (slider 1, 10 nm groove depth or pattern height)

slider disk interface, a similar area ratio can be obtained as:

$$\frac{A_{recessed}}{A} = 1 - \frac{\pi d^2}{4p^2} \tag{9.2}$$

To compare the two types of patterned media, we plotted in Figure 9.13 the change in flying height as a function of the area ratio as defined in Eq. (9.2). In Figure 9.13, the pattern height was 10 nm and the groove depth was 10 nm for DTR media. The results are shown for slider design 1. The data for the DTR media was obtained using the empirical equation obtained by Duwensee et al. [10]. From Figure 9.13, we observe that the flying height loss increases as the area ratio increases for both DTR and bit patterned slider disk interface. However, the change in flying height for the bit patterned interface

is higher as the area ratio increases compared to the DTR interface. This latter result is to be expected since side flow is more prevalent in the discrete bit patterned case than the discrete track case. In Figure 9.13, an area ratios less than 0.5 would represent pattern diameter values that are close to the pattern pitch values. Area ratios greater than 0.9 would represent small pattern diameters on the order of tens of nanometers. For smaller pattern diameters, the change in flying height increases by a larger amplitude for the bit patterned interface compared to the DTR interface, as the recessed area ratio increases.

9.6 Conclusions

1. High pressure peaks occur locally over each pattern feature. These high pressure areas are likely to cause lubricant loss over the bit areas.

2. From the parametric analysis of several femto slider designs, it was found that the slider flying height decreases linearly with increasing pattern height. The flying height decreases quadratically with the ratio of d/p.

3. The flying height loss of a discrete bit patterned media is a linear function for small values of pattern height keeping pattern diameter and pattern pitch constant.

4. The slider pitch angle was found to be independent of pattern height, slider design and skew angle.

5. The flying height loss is larger for a bit patterned slider disk interface compared

to a discrete track interface for the same recessed area of pattern.

Acknowledgment

Part of the material in this chapter has been submitted to ASME Information Storage and Processing Systems: A. N. Murthy and F. E. Talke, “Numerical Simulations of the Head/Disk Interface for Patterned Media”, 2007.

The dissertation author was the primary investigator of this paper directly supervised by Prof. Frank E. Talke.

Bibliography

[1] Albrecht, M., Rettner, C.T., Thomson, T., McClelland, G.M., Hart, M.W., Anders, S., Best, M.E., Terris, B.D., "Magnetic Recording on Patterned Media", *Joint NAPMRC 2003*, 6-8 Jan. 2003 Pg 36

[2] Wachenschwanz, D., Jiang, W., Roddick, E., et al., "Design of a Manufacturable Discrete Track Recording Medium", *IEEE Trans. Mag.*, 41 (2), pp. 670-675, 2005

[3] Duwensee, M., Suzuki, S., Lin, J., Wachenschwanz, D., and Talke, F., "Air Bearing Simulation of Discrete Track Recording Media", *IEEE Trans. Mag.*, 42 (10), Oct., pp. 2489-2491, 2006

[4] Gui J; Tang H; Wang L-P; Rauch G. C; Boutaghou Z; Hanchi J; Pitchford T; Segar P, "Slip Sliding Away: A Novel Head Disk Interface and its Tribology", *Journal of Applied Physics,* 87: 5383-5388, 2000

[5] Fua T-C; Suzuki S, "Low Stiction/Low Glide Height Head Disk Interface for High-Performance Disk Drive", *Journal of Applied Physics,* 85:5600-5605, 1999

[6] W.-L. Li, S.-C. Lee, C.-W. Chen, F.-R. Tsai, M.-D. Chen, W.-T. Chien, "The Flying Height Analysis of Patterned Sliders in Magnetic Hard Disk Drives", *Microsystem Technologies*, 11 (2005) 23-31, (2005)

[7] Tagawa, N., and Bogy, D., "Air Film Dynamics for Micro-textured Flying Head Slider Bearings in Magnetic Hard Disk Drives", *ASME J. Trib.*, 124, pp. 568-574, (2002)

[8] Tagawa, N., Hayashi, T., and Mori, A., "Effects of Moving Three-dimensional Nano-textured Disk Surfaces on Thin Film Gas Lubrication Characteristics for Flying Head Slider Bearings in Magnetic Storage", *ASME J. Trib.*, 123, pp. 151-158, (2001)

[9] Tagawa, N., and Mori, A., "Thin Film Gas Lubrication Characteristics of Flying Head Slider Bearings over Patterned Media in Hard Disk Drives", *Microsystem Technologies*, 9, pp. 362-368, (2003)

[10] Duwensee, M., Suzuki, S., Lin, J., Wachenschwanz, D., and Talke, F., “Simulation of the Head Disk Interface for Discrete Track Media”, published on-line, *Microsystem Technologies,* (2006)

[11] Murthy, A. N., Etsion, I., Talke, F. E., "Analysis of Surface Textured Air Bearing Sliders with Rarefaction Effects", submitted for publication to *Tribology Letters* (2007)

[12] Buscaglia, G., and Jai, M., Homogenization of the Generalized Reynolds Equation for Ultrathin Gas Films and its Resolution by FEM”, *ASME J. Trib.*, 126, pp. 547-552, (2004)

[13] Alexander, F., Garcia, A., and Alder, B.,“Direct Simulation Monte Carlo for Thin-film Bearings”, *Phys. Fluids*, 6 (12), pp. 3854-3860, (1994)

[14] Huang, W., Bogy, D., and Garcia, A., “Three-dimensional Direct Simulation Monte Carlo Method for Slider Air Bearings”, *Phys. Fluids*, 9 (6), pp. 1764-1769, (1997)

[15] Huang, W., and Bogy, D., “An Investigation of a Slider Air Bearing with an Asperity Contact by a Three Dimensional Direct Simulation Monte Carlo Method”, *IEEE Trans. Mag.*, 34 (4), pp. 1810-1812, (1998)

[16] Duwensee, M., Suzuki, S., Lin, J., Wachenschwanz, D., and Talke, F., ”Direct Simulation Monte Carlo Method for the Simulation of Rarefied Gas Flow in Discrete Track Recording Head/Disk Interfaces”, submitted to *ASME J. Trib.*, (2007)

[17] Fukui, S. et al., "Analysis of Ultra-Thin Gas Film Lubrication Based on Linearized Boltzmann Equation: First Report-Derivation of a Generalized Lubrication Equation Including Thermal Creep Flow," *ASME Journal of Tribology*, 110, pp. 253-262 (1988)

[18] Wahl, M., Lee, P., and Talke, F., “An Efficient Finite Element-based Air Bearing Simulator for Pivoted Slider Bearings Using Bi-conjugate Gradient Algorithms”, *STLE Trib. Trans.*, 39 (1), (1996)

[19] Fukui, S., and R., K., “A Database for Interpolation of Poiseuille Flow Rates of High Knudsen Number Lubrication Problems”, *ASME J. Trib.*, 112, p. 78, (1990)

10

Summary and Conclusions

10.1 Summary

Hard disk drive technology has made an amazing progress to date since the introduction of the first hard disk drive more than fifty years ago. The storage capacity has increased from 4.4 MB in 1956 to 1 Tb now for a single drive. The areal density has increased substantially from 2 Kb/in^2 to 150 Gb/in^2 now. At the same time, the flying height of the head disk interface has decreased from 20 μm to 8 nm in current hard disk drives. Various components of a typical hard disk drive and its head disk interface were described in Chapter 1. The research presented in this dissertation focussed on the investigation of the effect of shock, vibration, surface texture and surface pattern on the dynamics of the head disk interface.

The Galerkin weighted residual finite element method was used to develop a solution

of the continuum mechanics equations. For the analysis of shock events, the momentum equation is written in the form of a weighted residual and then integrated which leads to the weak form of the momentum equation. The domain is discretized into small sub-regions or elements to seek an approximate solution of the problem. For the non-linear dynamic solver, a Lagrangian formulation is implemented to find the time dependent deformation of the components in a hard disk drive model. A contact algorithm is utilized to model the interface between various components of the hard disk drive such as the slider, suspension, gimbal (or flexure), and disk.

The first structural model studied was the non-operational model for a load/unload type hard disk drive. In this model the disk is not spinning and the slider is parked away from the disk on a load/unload ramp through the suspension lift-tab. The hard disk drive geometry, mesh, boundary conditions, loads, and materials are also defined using a commercially available finite element program (Altair Hypermesh). The transient analysis is computed using a non-linear dynamic solver (LS-Dyna). The effect of shock amplitude, shock pulse width, and design parameters such as the suspension and gimbal thickness on the suspension lift-tab and dimple separation was studied. Stress analysis was performed for high stress regions in the head/disk interface, such as the bending region of the gimbal and suspension.

The second structural model studied was the operational model for a typical hard disk drive. In the operational model the air bearing was modeled between the slider and the disk. The air bearing was approximated using five linear springs. The stiffness of

these springs represents the air bearing stiffness in the z-direction, as well as pitch and roll direction.

The response of the head disk interface to shock was studied experimentally and numerically in three form factor hard disk drives. The different hard disk drives analyzed were 3.5 inch, 2.5 inch, and 1 inch form factors. The displacement of the actuator arm, the suspension and the slider due to shock was measured using a laser Doppler vibrometer for both non-operational and operational states of the disk drive. A detailed comparison of experimental and numerical results for the three form factor disk drives was conducted. In addition, structural models including two different hard disk drive enclosures for 1 inch form factor were developed. The response of the head disk interface to external vibrations applied in the x, y, and z directions were analyzed and a comparison of the two enclosure designs was conducted.

The Reynolds equation governing the head disk interface in hard disk drives was derived. Since the head disk spacing is on the order of 8 nm in current disk drives, slip flow corrections or "rarefaction" effects must be considered. The Reynolds equation with Boltzmann slip flow correction developed by Fukui and Kaneko was derived for the head disk interface with small clearance. A finite element solution of the steady state and time dependent Reynolds equation was described in Chapter 6.

An numerical model was later developed to study the effect of texture on the dynamics of the head disk interface for high Knudsen number flow. Optimum texture parameters, such as the texture density, texture aspect ratio, and texture portion were

determined for partial and full surface texture of slider air bearings. These optimum texture parameters were used to analyze the effect of texture on actual magnetic recording sliders. Numerical results showed that surface texture improves the dynamics of the head disk interface with respect to improved stiffness and damping characteristics.

In the last part of this thesis, steady state pressure generation for bit patterned media was studied. A numerical model with bit pattern transferred onto the slider air bearign surface was developed to investigate the steady state pressure distribution due to bit pattern in the head disk interface. The effect of pattern height, pattern diameter, slider skew angle, and slider pitch angle on flying height of a typical slider was investigated. It was found that the flying height decreases as a function of pattern height and the ratio of pattern diameter to pattern pitch. Simulation results showed that the redcution in flying height is a linear function of the pattern height for small values of pattern height and a quadratic function of the ratio of pattern diameter to pattern pitch.

10.2 Conclusions

In this dissertation, numerical and experimental techniques were used to investigate the dynamics of the head disk interface. First, the effect of shock and vibration on three different form factor (3.5 inch, 2.5 inch, and 1 inch) hard disk drives was studied both experimentally and numerically. In addition, the effect of surface texture and surface pattern on the slider flying characteristics was studied numerically by using a finite

element formulation of the Reynolds equation with rarefaction effects.

Based on the above investigations, the following conclusions can be drawn:

Non-operational shock in load/unload hard disk drives

From the simulation results, we found that lift-tab and dimple separation increases with increasing shock amplitudes.

We observed that lift-tab separation and dimple separation decrease with increasing shock pulse width.

The pulse width of shock input governs the onset time of lift-tab separation during a non-operational shock event.

Shorter pulse widths of shock excite higher frequencies and greater amplitudes. A short duration shock pulse width causes larger lift-tab separation than a longer duration pulse width for the same shock amplitude.

An increase in the thickness of suspension and gimbal spring causes a reduction in lift-tab separation as well as dimple separation.

The maximum von Mises stress in a flexure increases with increasing shock amplitudes. Plastic deformation in the flexure can occur when the amplitude of shock is extremely high.

Experimental and numerical Investigation of shock in 3.5 inch and 2.5 inch HDD's

Based on the experimental and numerical results from this study, we can draw the following conclusions:

We observed that there is no actuator arm - disk impact for the specified non-operational shock load conditions in both form factor HDD's.

Operational shock response showed that the disk contribution to out-of-plane displacements of the head suspension assembly is less than 10% for the specified shock load conditions in our experimental set up.

A Numerical finite element model of the 3.5 inch HDD was developed to simulate the shock response for the non-operational case. The results obtained in the simulation compared well with the experimental results. The bending modes of the suspension and actuator arm were also in good agreement with the experimental results.

In comparison, we observed that the vibrations modes of the suspension-arm assembly in the 2.5 inch HDD was higher than the vibration modes of the suspension-arm assembly in the 3.5 inch HDD.

Shock and vibration investigation in 1 inch HDD's

Microdrives from two different hard disk drive manufacturing vendors were subjected to shock and vibration experimentally. From this study, we can draw the follow-

ing conclusions:

The shock response of the drives varied with manufacturing vendors due to differences in the main mechanical design of the drives. In particular, an adhesive wrapping around the microdrive was found to be critical to give a more robust device and allow more structural rigidity to the top cover. The thickness of the cover plate was found to be important as far as shock absorption is concerned, i.e., the thicker the cover plate; the better is the shock response.

To increase the operational shock specification from 200 G to 300G the suspension design should be modified to prevent slap motion of the head/suspension against the disk. Increasing the gram load of the suspension could be a solution to reduce head slap due to shock.

Voice coil magnets can be a cause of shock failure due to bonding weakness of the magnets to the base plate.

The numerical shock simulation compared close to the experimental results for both non-operational and operational shock.

The dynamic response of the head disk interface was investigated numerically for two different designs of 1-inch hard disk drive enclosures, the so-called "thin" enclosure and the "thick" enclosure. First, a modal analysis for the two enclosure designs was performed numerically. Then the in-plane and out-of-plane vibration response was determined for the HDD model with the two enclosure designs. From the simulation results, we observe that the thinner enclosure has better performance with respect to

forced vibrations in terms of reduced amplitude of slider vibrations.

We conclude that the design of 1-inch form factor hard disk drive enclosures has a significant effect on the dynamics of the head disk interface.

Effect of surface texture on flying characteristics of air bearing sliders

Based on the simulations of textured slider, we draw the following conclusions:

Parallel slider bearings with surface texture generate a net load carrying capacity while the untextured parallel sliders do not generate a load carrying capacity.

Surface texture reduces the load carrying capacity of an inclined slider above a critical pitch angle (with respect to the untextured slider), but it increases the load carrying capacity below the critical pitch angle.

The dynamic flying characteristics of textured magnetic recording sliders show improved performance in terms of flying height modulation, stiffness and damping.

Texturing of air bearing sliders improves the dynamic performance of the head disk interface.

Numerical simualtion of the head disk interface for patterned media

High pressure peaks occur locally over each pattern feature. These high pressure areas are likely to cause lubricant loss over the bit areas.

From the parametric analysis of several femto slider designs, it was found that the

slider flying height decreases linearly with increasing pattern height. The flying height decreases quadratically with the ratio of d/p.

The flying height loss of a discrete bit patterned media is a linear function for small values of pattern height keeping pattern diameter and pattern pitch constant.

The slider pitch angle was found to be independent of pattern height, slider design and skew angle.

The flying height loss is larger for a bit patterned slider disk interface compared to a discrete track interface for the same recessed area of pattern.

Appendix A

Appendix for Chapter 2

A.1 Derivation of The Principle of Virtual Work in LS-Dyna Solver

In Chapter 2.4, the momentum equation was given as follows:

$$\sigma_{ij,j} + \rho f_i = \rho \ddot{x}_i \tag{A.1}$$

We seek a solution to Eq. (A.1) satisfying the traction boundary conditions on boundary ∂b_1 (Eq. (A.2)),

$$\sigma_{ij} n_j = T_i(t) \tag{A.2}$$

the displacement boundary conditions on boundary ∂b_2(Eq. (A.3)),

$$x_i\left(X_\alpha,\, t\right) = D_i\left(t\right) \tag{A.3}$$

and the contact discontinuity (Eq. (A.4)) along the interior boundary ∂b_3 when $x_i^+ = x_i^-$.

$$\left(\sigma_{ij}^+ - \sigma_{ij}^-\right) n_i = 0 \tag{A.4}$$

In the equations shown above, σ_{ij} is the Cauchy stress, ρ is the density, $f$is the body force density, $\ddot{x}$ is the acceleration, the comma in $\sigma_{ij,j}$ denotes co-variant differentiation, and n_{ij} is a unit normal to a boundary element of ∂b.

Conservation of mass is given by:

$$\rho V = \rho_0 \tag{A.5}$$

where ρ_0 is the density, and V is the relative volume. The determinant of the deformation gradient matrix, F_{ij}, is given as:

$$F_{ij} = \frac{\partial x_i}{\partial X_j} \tag{A.6}$$

The energy equation can be written as follows:

$$\dot{E} = V s_{ij} \dot{\varepsilon}_{ij} - \left(p + q\right) \dot{V} \tag{A.7}$$

Eq. (A.7) is integrated with respect to time and is used for the equation of state evaluations and a global energy balance.

In Eq. (A.7), s_{ij} represents the deviatoric stress given as

$$s_{ij} = \sigma_{ij} + (p + q)\,\delta_{ij} \tag{A.8}$$

and p represents the pressure given as follows

$$p = -\frac{1}{3}\sigma_{ij}\delta_{ij} - q = -\frac{1}{3}\sigma_{kk} - q \tag{A.9}$$

In Eq. (A.8) q is the bulk viscosity, δ_{ij} is the Kronecker delta (i.e., $\delta_{ij} = 1$ if $i = j$; else $\delta_{ij} = 0$), and $\dot{\varepsilon}_{ij}$ is the strain rate tensor.

We then write:

$$\begin{aligned}\int_v (\rho\ddot{x}_i - \sigma_{ij,j} - \rho f)\,\delta x_i dv + \int_{\partial b_1} (\sigma_{ij}n_j - t_i)\,\delta x_i ds \\ + \int_{\partial b_3} \left(\sigma_{ij}^+ - \sigma_{ij}^-\right) n_j \delta x_i ds = 0\end{aligned} \tag{A.10}$$

where δx_i satisfies all the boundary conditions on ∂b_2. Application of the divergence theorem yields

$$\int_v (\sigma_{ij}\delta x_i)_{,j}\, dv = \int_{\partial b_1} \sigma_{ij}n_j\delta x_i ds + \int_{\partial b_3} \left(\sigma_{ij}^+ - \sigma_{ij}^-\right) n_j \delta x_i ds \tag{A.11}$$

and

$$(\sigma_{ij}\delta x_i)_{,j}\,\sigma_{ij,j}\delta x_i = \sigma_{ij}\delta x_{i,j} \tag{A.12}$$

This leads to the weak form of the equilibrium equations as follows:

$$\delta\pi = \int_v \rho\ddot{x}_i\delta x_i dv + \int_v \sigma_{ij}\delta x_{i,j} dv - \int_v \rho f_i \delta x_i dv - \int_{\partial b_1} t_i \delta x_i ds \tag{A.13}$$

Bibliography

[1] Hallquist, J., “LS-Dyna Users Manual”, Livermore Software Technology Corp. 1998

[2] Hallquist, J., “LS-Dyna Theory Manual”, Livermore Software Technology Corp. 1998

Appendix B

Appendix for Chapter 6

B.1 Finite element solution for the time dependent Reynolds equation

The dimensional time-dependent Reynolds equation can be written as (Eq. (B.1), Chapter 7):

$$\frac{\partial \Theta}{\partial t} \cdot \int_{\Omega} 12\mu W N d\Omega + \int_{\Omega} \left\{ \nabla W \cdot \left[\overline{Q}\left(\Theta\right) \left(h\Theta\nabla\Theta - \Theta^2 \nabla h \right) \right] - 6\mu V \Theta W \right\} d\Omega = 0 \tag{B.1}$$

Applying the Galerkin weighted residual finite element method, we introduce the following variables:

$$[\Gamma] = \int_{\Omega} 12\mu W N d\Omega$$
$$[F] = \int_{\Omega} \left\{ \nabla W \left[\overline{Q}(\Theta) \left(h\Theta\nabla\Theta - \Theta^2 \nabla h \right) \right] - 6\mu V \Theta W \right\} d\Omega \tag{B.2}$$

Using the variables above, we can re-write Eq. (B.1) in symbolic matrix notation as:

$$[\Gamma] \frac{\partial \Theta}{\partial t} + \{F\} = 0 \tag{B.3}$$

where Γ is a constant matrix of known terms and F is a non-linear function of Θ. A number of explicit and implicit time stepping techniques are available for the solution of this type of equation. An explicit forward difference or forward Euler method for approximating the derivative is as follows:

$$\frac{\partial \Theta}{\partial t} \approx \frac{\triangle \Theta}{\triangle t} = \frac{\{\Theta\}^{n+1} - \{\Theta\}^n}{\triangle t} \tag{B.4}$$

Substituting Eq. (B.4) in Eq. (B.3), we get:

$$[\Gamma] \{\triangle \Theta\} = - \{F\}^n \triangle t \tag{B.5}$$

The forward Euler method can be easily applied to a non-linear system and is first order accurate. Hence, the error is directly proportional to the time step used in the numerical method, i.e., the time step has to be very small. To avoid very small time steps, an implicit method such as the backward Euler method can be used in combination with

the forward Euler method. In the backward Euler method, the derivative is computed at the end of the time step. Eq. (B.5) is rewritten as follows:

$$\left[\triangle t^{-1}\Gamma + K_T^n\right]\{\triangle\Theta\} = -\{F\}^n - \{\triangle F\} \tag{B.6}$$

where the tangent matrix $K_T$is the derivative of the vector F with respect to the variable Θ. Eq. (B.5) and Eq. (B.6) can be combined by introducing a parameter Υ as follows:

$$\left[\triangle t^{-1}\Gamma + \Upsilon K_T^n\right]\{\triangle\Theta\} = -\{F\}^n - \Upsilon\{\triangle F\} \tag{B.7}$$

where Υcan vary between 0 and 1. If the parameter Υ is equal to zero, then we have the explicit forward Euler method. If the parameter Υ is equal to one, then we have the implicit backward Euler method. Such a combined numerical method allows better control over the time step and stability of the solution.

The time dependent Reynolds equation is solved simultaneously with a finite element model for the suspension and gimbal. The suspension and gimbal are modeled using simple beam elements. The roll motion of the slider is added as an additional degree of freedom in the suspension and gimbal model. The equations of motion for the beam model can be written as follows:

$$[M]\left\{\ddot{d}\right\} + [\lambda]\left\{\dot{d}\right\} + [K]\{d\} = \left\{\overrightarrow{F}\right\} \tag{B.8}$$

where d is the generalized displacement vector for the z direction, the pitch direction,

and the roll direction and $\overrightarrow{F}$ is the right hand side force vector containing the air bearing forces and moments. The Newmark method, given by Eq. (B.9) is used to integrate this equation.

$$\begin{aligned} \{d\}^{n+1} &= \{d\}^n + \triangle t \left\{\dot{d}\right\}^n + \frac{\triangle t^2}{2}(1-2\beta)\left\{\ddot{d}\right\}^n + \triangle t^2 \beta \left\{\ddot{d}\right\}^{n+1} \\ \left\{\dot{d}\right\}^{n+1} &= \left\{\dot{d}\right\}^n + \triangle t\,(1-\gamma)\left\{\ddot{d}\right\}^n + \triangle t\gamma \left\{\ddot{d}\right\}^{n+1} \end{aligned} \tag{B.9}$$

where β and γ are the Newmark parameters that define the accuracy and stability of the solution. In this thesis, the values assigned for β and γ are 0.25 and 0.50 respectively. The Newmark method is used to solve the suspension and gimbal model in conjunction with the implicit backward Euler method for the solution of the air bearing forces and moments.

Bibliography

[1] Wahl, M., Lee, P., and Talke, F, "An Efficient Finite Element-Based Air Bearing Simulator for Pivoted Slider Bearings Using Bi-Conjugate Gradient Algorithms", *Tribology Transactions*, Vol.39 (no. 1): 130-138, 1996

[2] Baugh, E. Weissner, S. Talke, F.E., "Biquadratic Models for Slider Airbearing Surfaces", *IEEE Transactions on Magnetics*, Vol.34 (no. 4): 1816-1818, 1998

[3] Weissner, S., Zander, U., and Talke, F.E., "A New Finite-Element Based Suspension Model Including Displacement Limiters for Load/Unload Simulations" *Transactions of the ASME*, Vol.125 (no. 1): 162-167, 2003

[4] Jayson, E. M., Murphy, J., Smith, P. W., Talke, F.E., "Effects of Air Bearing Stiffness on a Hard Disk Drive Subject to Shock and Vibration", *Journal of Tribology*, Vol.125 (no.): 343-249, 2003

[5] Huang, W., Bogy, D., " The Effect of Accomodation Coefficient on Slider Air Bearing Simulation", *ASME Journal of Tribology*, 122: 427-435, 2000

[6] C. Pozrikidis, "Numerical Computation in Science and Engineering", *Oxford University Press*, 1998

[7] Thomas J. R. Hughes, "The Finite Element Method: Linear, Static and Dynamic Finite Element Analysis", Prentice-Hall, 1987